Technische Universität München
Fakultät für Elektrotechnik und Informationstechnik
Lehrstuhl für Kognitive Systeme

Multi-sensory tactile feedback control for robot physical interaction and biped locomotion

Julio Rogelio Guadarrama Olvera

Vollständiger Abdruck der von der Fakultät für Elektrotechnik und Informationstechnik der Technischen Universität München zur Erlangung des akademischen Grades eines

Doktor-Ingenieurs (Dr.-Ing.)

genehmigten Dissertation.

Vorsitzende:

Prof. Dr.-Ing. Sandra Hirche

Prüfer der Dissertation:

1.Prof. Gordon Cheng, Ph.D.

2.Prof. Dr.-Ing. Tamim Asfour

3.Prof. Shuuji Kajita, Ph.D.

Die Dissertation wurde am 14.06.2021 bei der Technischen Universität München eingereicht und durch die Fakultät für Elektrotechnik und Informationstechnik am 06.08.2021 angenommen.

Abstract

Physical interaction is becoming a required feature in modern robotic applications. The addition of new technologies such as robotic skins provides feedback that allows physical interaction for robots with the environment and human co-workers. However, the large amounts of information that robot skin supply come with the challenge of interpreting and extracting meaningful insights for feedback control. This thesis provides methods and algorithms to extract meaningful information from multi-modal tactile feedback to enable whole-body interaction control. This work contributes to the formulation of operational tasks from distributed force sensing for body compliance behaviors in fixed and floating base robots. The interactive tasks formulated in this thesis are compatible with task fusion methods with strict or soft prioritization for whole-body control.

With the additional geometric information provided by robot skin, this thesis developed the pressure-driven body compliance modality that amplifies the contact forces when concentrated in a small area. This work also presents formulations to use additional sensing modalities aside from contact force as feedback to produce virtual interactions with the environment. The virtual interaction tasks developed in this work generate virtual-repulsive fields from sensor measurements to impose whole-body compliant behaviors. Two examples of virtual interactions using proximity and temperature sensors are presented. The different modalities of direct and virtual interaction provide contextual information that can help to generate combined body behaviors. A modality for robot nociception using pressure-driven compliance to detect potentially harmful interactions and generate reaction reflexes is introduced. With the proximity-based collision-avoidance modality, a behavior to detect local minima that keep a robot from fulfilling an end-effector task without touching the environment is realized. The robot behavior is adapted to apply contact forces in the environment to modify it to fulfill the end effector tasks, keeping the interaction forces within a set range.

This thesis provides formulations for direct and virtual interactions using plantar skin to enhance the capabilities of biped balance and walking control. Furthermore, this work presents the formulations to compute the significant metrics for balance and walking from plantar tactile feedback and methods for closed-loop control. A method to use plantar tactile information is introduced to construct the supporting polygon and use it to define constraints for ZMP (Zero Moment Point) and DCM (Divergent Component of Motion) tracking controllers. The geometry of the supporting polygon is also used in this work to adapt the walking motions online to continuously walk over partial footholds without the need for exploratory motions. We used the proximity sensing modality to develop preemptive foot compliance control to adapt the foot orientation before foot landing in the single support phase of the walking cycle. This modality of foot compliance suppresses 80% of the impact forces when walking over flat terrain and improves walking over uneven terrain. The contributions in this thesis were extensively evaluated in three experimental platforms, including two full-size humanoid robots running two different walking controllers and software frameworks.

Preface

This work was only possible with the help of a large number of mentors, colleagues, friends, and family to whom I am deeply thankful.

I would like to thank my adviser Prof. Dr. Gordon Cheng, who gave the scientific advice and kind feedback that helped me achieve the contributions stated in this thesis. I would also like to thank my mentor Dr. Emmanuel Dean who gave me a lot of scientific and technical advice that built an important base for the contributions in this thesis. Aside from their academic guidance, I deeply appreciate their personal advice and support during all the years we have worked together. I would also like to thank my co-authors, friends, and fellow members of the H1 group: Florian Bergner, Quentin Leboutet, and Simon Armleder who were always bringing valuable feedback and interesting discussions in all kind of matters, aside from helping me with the experimental evaluations in this thesis. Thank you also for helping me revise and improve the quality of this thesis.

Special thanks to Prof. Shuuji Kajita whose famous book helped me understand the basics of humanoid robotics and who helped me develop the contributions for walking control presented in this thesis. I also would like to thank Prof. Fumio Kanehiro for his kind invitation to my two-month internship at the Intelligent Systems Research Institute in the National Institute of Advanced Industrial Science and Technology (AIST). I would like to extend my thanks to Rafael Cisneros, Mehdi Benallegue, Mitsuharu Morisawa, Iori Kumangai, Obot Nse, and all the members of the Humanoid Research Group for hosting me as a guest and sharing their ideas to develop my research. Special thanks to Arnaud Tanguy for his technical support during my internship.

Thanks to the international community of humanoid robotics. Special thanks for giving me inspiration and thoughtful discussion during my doctoral studies to Dr. Johannes Englsberger, Dr. Christian Ott, Dr. Máximo A. Roa, Prof. Alin Albu-Schäffer, Prof. Olivier Stasse, Prof. Tamim Asfour, Prof. Baek-Kyu Cho, Prof. Jun Nakanishi, and Prof. Taisuke Kobayashi.

Thanks to Ilona Nar-Witte, Wibke Borngesser, Brigitte Rosenlehner, Katharina Stadler, and Sebastian Stenner, the administrative and technical staff of the Institute For Cognitive Systems (ICS) who supported me with all the administrational and technical issues of my doctoral studies and research work. Thanks also to Constantine Uhde, Nicolas Berberich, Alireza Malekmohammadi, Natalia Paredes Acuña, Dr. Stefan Ehrlich, Dr. Erhard Wieser, Dr. Shunki Itadera, Dr. Jasmin Kajopoulos, Dr. John Nassour, Prof. Pablo Lanillos, and Prof. Karinne Ramirez-Amaro, my PostDoc colleagues and fellow PhD students at ICS for their friendship and thoughtful discussions during the seminars and events.

Thanks to Dennis Ossadnik, Chenghao Wang, Fengyi Wang, Hao Ma, Zhannan Zhang, Zhiyue Chen, Huiwen Pan, and Tony Nguemo, the students I had the honor to advise during these years who brought fresh ideas and sharp discussion to improve our research.

Thanks to my supporting and loving parents Margarita Olvera and Vicente Guadarrama and my brother Vicente for supporting me during all these years. You were always close and in contact despite being a thousand kilometers away.

Thanks to the Mexican National Council on Science and Technology and the Mexican people for giving me the opportunity and honor to receive a scholarship (No. 410699) for my doctoral studies. Thanks also to the people of Munich and Bavaria for giving me a home during these years and for sharing with me your culture and tradition.

Finally, the most special thanks and the deepest gratitude to Margarita Garduño Eligio, my loving wife who encouraged me to take this challenge. You supported me and accompanied me on this adventure around the world and for that, I will always be thankful.

List of publications

Parts of this thesis have already been published in:

Journal articles

J1 **Guadarrama Olvera, J. R.**, Dean Leon, E., Bergner, F., and Cheng, G. (2020). Plantar Tactile Feedback for Biped Balance and Locomotion on Unknown Terrain. *International Journal of Humanoid Robotics*, 17(01), 1950036.

J2 **Guadarrama Olvera, J. R.**, Dean Leon, E., Bergner, F., and Cheng, G. (2019). Pressure-driven body compliance using robot skin. *IEEE Robotics and Automation Letters*, 4(4), 4418-4423.

J3 Leboutet, Q., Roux, J., Janot, A., **Guadarrama Olvera, J. R.**, and Cheng, G. (2021). Inertial Parameter Identification in Robotics: A Survey. *Applied Sciences*, No. applsci-1199309.

J4 Kobayashi, T., Dean-Leon, E., **Guadarrama Olvera, J. R.**, Bergner, F., and Cheng, G. (2021). Whole-Body Multi-Contracts Haptic Human-Humanoid Interaction based on Leader-Follower Switching: A robot dance of the “box step”. *Advanced Intelligent Systems*, No. aisy.202100038R1.

J5 Cheng, G., Dean-Leon, E., Bergner, F., **Guadarrama Olvera, J. R.**, Leboutet, Q., and Mittendorfer, P. (2019). A comprehensive realization of robot skin: Sensors, sensing, control, and applications. *Proceedings of the IEEE*, 107(10), 2034-2051.

J6 Bergner, F., Dean-Leon, E., **Guadarrama Olvera, J. R.**, and Cheng, G. (2019). Evaluation of a large scale event driven robot skin. *IEEE Robotics and Automation Letters*, 4(4), 4247-4254.

J7 Wang, F., **Guadarrama Olvera, J. R.**, and Cheng, G. (2021). Optimal Order Pick-and-Place of Objects in Cluttered Scene by a Mobile Manipulator. *IEEE Robotics and Automation Letters*, 6(4), 6402-6409.

Peer-reviewed conference papers

C1 **Guadarrama Olvera, J. R.**, Dean, E., and Cheng, G. (2017, May). Using intentional contact to achieve tasks in tight environments. In *2017 IEEE International Conference on Robotics and Automation (ICRA)* (pp. 1000-1005). IEEE.

C2 **Guadarrama Olvera, J. R.**, Bergner, F., Dean, E., and Cheng, G. (2018, November). Enhancing biped locomotion on unknown terrain using tactile feedback. In *2018 IEEE-RAS 18th International Conference on Humanoid Robots (Humanoids)* (pp. 1-9). IEEE. **Best Conference Paper Award**.

C3 Leboutet, Q., **Guadarrama Olvera, J. R.**, Bergner, F., and Cheng, G. (2020, May). Second-order Kinematics for Floating-base Robots using the Redundant Acceleration Feedback of an Artificial Sensory Skin. In *2020 IEEE International Conference on Robotics and Automation (ICRA)* (pp. 4687-4694). IEEE.

C4 Kobayashi, T., Dean-Leon, E., **Guadarrama Olvera, J. R.**, Bergner, F., and Cheng, G. (2019, October). Multi-Contacts Force-Reactive Walking Control during Physical Human-Humanoid Interaction. In *2019 IEEE-RAS 19th International Conference on Humanoid Robots (Humanoids)* (pp. 33-39). IEEE.

C5 Kobayashi, T., Aotani, T., **Guadarrama Olvera, J. R.**, Dean-Leon, E., and Cheng, G. (2019, August). Reward-Punishment Actor-Critic Algorithm Applying to Robotic Non-grasping Manipulation. In *2019 Joint IEEE 9th International Conference on Development and Learning and Epigenetic Robotics (ICDL-EpiRob)* (pp. 37-42). IEEE.

C6 Dean-Leon, E., **Guadarrama Olvera, J. R.**, Bergner, F., and Cheng, G. (2019, May). Whole-body active compliance control for humanoid robots with robot skin. In *2019 International Conference on Robotics and Automation (ICRA)* (pp. 5404-5410). IEEE.

C7 Ossadnik, D., **Guadarrama Olvera, J. R.**, Dean-Leon, E., and Cheng, G. (2018, November). Adaptive Friction Compensation for Humanoid Robots without Joint-Torque Sensors. In *2018 IEEE-RAS 18th International Conference on Humanoid Robots (Humanoids)* (pp. 980-985). IEEE.

Contents

List of Figures

List of Tables

List of Algorithms

List of Acronyms

C

CMP - Centroidal Moment Pivot..... 1, 4, 12, 61
CoM - Center of Mass..... xii, xiii, xvii, 1, 63, 64, 67–70, 79, 80, 95, 99, 102–104, 108, 112
CoP - Center of Pressure..... xii–xiv, 1, 12, 14, 28, 66, 72–74, 78, 81
CP - Capture Point..... 1, 61

D

DCM - Divergent Component of Motion.. i, xii, xiv, xvii, 1, 4, 5, 16, 61, 67–70, 79, 81, 95, 99, 102–106, 108, 114
DoF - Degrees of Freedom..... 1, 15, 16, 18, 21, 23, 24, 33, 36, 46, 58

G

GRF - Ground Reaction Force..... xii, 1, 4, 12, 61, 63–65, 73, 74, 108
GRW - Ground Reaction Wrench..... xv, 1, 73, 76, 86, 88

L

LIP - Linear Inverted Pendulum..... xii, 1, 63, 64, 67, 94, 95, 108

P

PFC - Preemptive Foot Compliance..... xv, xvi, 1, 16, 62, 87–93, 109, 110, 113
PGRW - Preemptive Ground Reaction Wrench..... 1, 87

Q

QP - Quadratic Programming..... 1, 95, 97–99, 114

V

VGRW - Virtual Ground Reaction Wrench..... 1, 87
VRP - Virtual Repellent Point..... xii, xvii, 1, 68, 103–106, 114

Z

ZMP - Zero Moment Point..... i, vii, xii–xiv, xvi, xvii, 1, 4, 12, 14, 18, 61, 63, 65–67, 69–71, 78–80, 82, 86, 94, 95, 97, 99–109, 113, 114

1. Introduction

Humanoid robots are complex systems developed to operate in environments and conditions originally intended for human beings [9, 10, 11, 12, 13, 14]. The target of humanoid robots is to cooperate with human partners in labor and to alleviate them in tasks that are either dangerous, exhausting, or monotonous. Such a challenge demands the incorporation of different state-of-the-art technologies together into the robot's design to increase its capabilities. These contributions enhance the capabilities of all their different components. From mechanical high-powered actuation to multi-modal perception systems and real-time control, new advances emerge every decade to improve the performance and broaden the span of applications for humanoid robots. Within these new technologies, *tactile sensors* and *robot skins* have helped improve physical interaction between robots and the environment, including human beings [15, 16, 5].

This thesis presents different methods to exploit multi-modal tactile information for physical interaction and bipedal locomotion. The spatial distribution of multiple types of sensors that state-of-the-art robot skins incorporate, increases the capabilities for interaction by providing additional information that the classic force-torque sensor approaches miss. But the addition of thousands of sensors in the system comes with a series of challenges to interpret the meaningful components of large amounts of tactile information. This work will break down the formulations to exploit tactile information, which includes measurements of direct contact forces and additional modalities that do not involve physical contact but provide awareness of the conditions of the environment around the robot. Furthermore, a framework to combine different types of interactions in whole-body behaviors is presented and validated in several experimental scenarios involving both fixed base and floating base robots, including full-size humanoid robots.

The formulations to handle both types of interactions will be expanded to include plantar skin into biped balance and locomotion control. Plantar skin enhanced the capabilities of walking controllers by providing feedback for walking over uneven terrain and small footholds. Extensive experimentation was performed to assess and validate the formulations in two different robots that run two different walking controllers.

1.1. Motivations and Challenges

Robot skins are distributed sensing systems made up of a series of *tactile sensing* elements commonly known as *taxels*, and the communication and interfacing channels with a robot. These systems provide large amounts of information when stimuli are applied to a set of taxels. The larger the stimulated area, the wider the stream of tactile information generated. Within all the information generated by skin systems, there are different components with

different meanings. For example, it contains noise, geometric information, vibrations, harmful interactions, safe interactions, other sensing modalities such as proximity or temperature, etc. Although the size of the data stream can be regulated by different sensing paradigms and sensor calibration, physical interaction must be kept safe for all, the robot, the environment, and the operators/coworkers, and useful for control purposes. In this context, the usage of tactile information opens the first challenge: How to *extract meaningful information* from the torrent of data to generate feasible (computational and dynamically consistent) reaction motions from the tactile stimuli?

In large-scale systems, for example, a full-size humanoid robot with whole-body skin, traversing all the sensing modalities of all the taxels may not be feasible in every control cycle. Therefore, a strategy to identify the useful taxels for one interaction is required to *lower the computation effort*. At the same time, these useful stimuli contribute to computing the resultant forces applied to the link. This problem presents a second challenge to address when working with tactile information on: How to survey *large groups of taxels* that cover every link of a robot without exceeding the computational capacities of an embedded system?

Most skin systems provide pressure sensing which measures directly the contact force. Furthermore, multi-modal skin systems as [1] provide *additional modalities* which have no direct meaning as external forces in the dynamic model of the robot. This problem brings on another challenge: How to use additional sensing modalities to generate dynamically consistent reaction motions?

With feedback from several sensing modalities, a robot can have reactive motions with different priorities among them. How to combine interactions of different sources together into combined behaviors? brings another challenge for this thesis. Furthermore, what are the constraints required to combine these interactions in practices?

Skin provides tactile information immediately when the contract starts. Furthermore, if the skin provides proximity sensing, the geometry of the contact can be estimated before the physical interaction. This feature is particularly beneficial for balancing and walking. The available geometric information directly at the foot landing can help define the reaction movements to keep balance and adjust the walking motions to achieve stable walking. However, *extracting meaningful information for balance and walking* from all the skin information and *how to use them in the different phases of walking*? are complex challenges.

1.2. Contribution

This work contributes to providing the control algorithms needed for robots to efficiently exploit multi-modal tactile information for both whole-body physical interaction and biped locomotion. Focusing on the control problems related to the usage of such sensory information, the details about how the tactile information is generated are kept out of the scope of this work. The

formulations are intended to be used by any robot with standard sensors (e.g. IMU, force-torque, joint encoders) and any type of robot skin that provides multi-modal information and spatial calibration.

1.2.1. Contributions to whole-body physical interaction

Whole-body physical interaction
The contributions of this thesis advance the state-of-the-art on whole-body compliance providing formulations for interaction tasks based on tactile information. This extends the formulations for body compliance introduced by previous works at the Institute for Cognitive Systems to handle multiple large areas of interaction simultaneously and floating base dynamics. The execution of multiple tasks requires the implementation of a strict hierarchical whole-body controller, which was adapted using null space projectors for floating base robots in this thesis.

Multi-modal physical and virtual interaction
This thesis contributes to the formulations to generate body reactions to sensing modalities other than contact force. This covers the generation of virtual forces from other sensor signals and the task formulation for them.

The specific sensing modalities this thesis examines are:

- *Proximity to objects* sensing is used to prevent collisions with the environment by creating a repulsive field that will push away all the robot links from the environment and other links. This modality is also used to predict the geometry of the contact area before the actual contact happens. This feature turned out highly valuable for walking control.
- *Pressure distribution* sensing is used to enable a new modality of body compliance which modifies the body admittance reaction inversely proportional to the size of the contact area. It combines the contact force measurement of the taxels with the geometric information of its spacial distribution. With this modality, highly concentrated forces produce faster compliant reactions, and distributed pressure interactions produce slow reactions.
- *Temperature* sensing is used to generate repulsive forces to increase the distance to potentially harmful hot surfaces. This enables another nociceptive flexion reflex to prevent the touch of surfaces that can melt the robot covers and wiring.

Robot nociception

This thesis took inspiration from the nociceptive modalities in human skin and the reflexes it triggers to enable robot nociception from tactile information. The multi modal information is used to make changes in the priority of tasks to adapt the robot behavior according to the interactions. The robot nociception presented in this work cancels the execution of purpose tasks if they produce harmful interactions.

Intentional contact

Combined modalities of interactions are used to enable an active exploratory behavior for robots in this work. This thesis explores priority switching rules for safety tasks to increase the executability of purpose tasks by exerting intentional contacts in the environment to modify it to achieve tasks in tight environments.

1.2.2. Contributions to biped balance and locomotion

This thesis extends the formulations of the direct and virtual interactions to plantar tactile feedback for biped balance and walking control.

Balance with plantar tactile feedback

This thesis also contributes algorithms to exploit the multiple sensing modalities of robot skin for biped balance and walking. The methods to extract tactile information proposed in the first part are adapted to measure the important metrics used as feedback in balance and walking controllers for bipedal robots. These metrics include the ZMP (Zero Moment Point), CMP (Centroidal Moment Pivot), GRF (Ground Reaction Force), and DCM (Divergent Component of Motion). These metrics are commonly measured using ankle force-torque sensors. This thesis shows that skin sensors can provide an alternative solution when the ankle of a robot cannot allocate one of these sensors.

The geometric insights of the tactile information are used in this work to approximate the shape of the contact geometry. This information provides an accurate description of the supporting region immediately after foot landing at walking. This thesis developed algorithms to construct the supporting polygon and its important reference points with tactile information. For example, the contact area size, the centroid of the supporting polygon, the bounding box, and the simplified inscribed smaller order polygons.

This thesis performed an extensive experimental evaluation of the plantar tactile information in classic balance control techniques. However, these techniques make some assumptions on the contact geometry because ankle sensors cannot provide an actual measurement of the supporting polygon (e.g., full static contact of the sole with the ground). Thus, these methods were generalized to use the real contact information in the definition of the constraints for the controllers.

Walking with plantar tactile feedback

In this work, the tactile information was used to develop a method that uses contact information to define a step replanning strategy when the contact area is too small. The step replanning strategy considers the size of the obstacle to re-define the new footstep location clearing the whole area of the obstacle. This approach can identify certain conditions that ankle sensors cannot because the interaction forces are in equilibrium.

Another improvement to the walking motion generation introduced in this work is the online modification of the walking motion plans from plantar tactile information. The centroid of the supporting polygon is used to redefine the waypoints for the DCM trajectory to generate dynamically consistent trajectories to step over partial footholds, down to one-third of the sole area. As a result of this method, a waling controller designed for full sole contacts on flat ground can successfully walk continuously over partial footholds without the need for exploratory motions or fast ankle reactions.

Using plantar proximity sensing, this thesis developed a preemptive foot compliance modality to complement the classic ankle strategies for terrain adaptation. The preemptive foot compliance modifies the foot orientation during the swing trajectory to maximize the contact area and minimize the impact force at foot landing. This modality improves the performance of walking controllers even on flat ground by artificially damping the foot swing motion a few millimeters from the ground.

Tactile mountable shoes

From the experimental works of this thesis, a practical apparatus to mount plantar skin on biped robots was developed: *mountable tactile shoes*.

The plantar tactile formulations for bipedal robot balance and locomotion were extensively tested on two different robots: The HRP-2Kai humanoid robot from Kawada industries and the REEM-C humanoid robot from PAL Robotics. The plantar tactile sensors were fixed to the feet of these humanoid robots using mountable shoes. This thesis developed tactile shoes as an apparatus to easily and fast mount plantar skin on robots without modifying the foot mechanical design or affecting the robot's capabilities. With this approach, mounting and removing plantar skin on a full-size humanoid robot takes about five minutes and it requires only the foot external geometry to prepare.

1.3. Thesis Outline

This thesis will be presented as follows:

Chapter 2 will introduce the related works that help develop the contributions of the thesis. It will also present the biological inspirations for physical interaction, including plantar sensation that helped to develop the formulations written in this work. The experimental platforms used to evaluate the contributions of this thesis will be introduced in Section 2.3.

Chapter 3 will present the formulations for physical and virtual interactions that make uses of multi-modal distributed sensing. It provides the fundamentals of the operational space formulation that set the basis for the formulation of the interaction tasks. Then, it will introduce the methods for physical and virtual interaction, including experimental validations for every sensing modality and combinations of them in a number of whole-body behaviors.

Chapter 4 will extend the formulations for physical and virtual interaction for biped balance and locomotion. It will start by summarizing the fundamentals of bipedal robot walking and balance control that set the basis for the contributions of this thesis using plantar skin. Then, the methods to compute the significant metrics for balance from plantar tactile information will be presented. Furthermore, these formulations are used to provide additional feedback in balance and walking controllers that improve the performance in flat ground and enables walking over uneven terrain and partial footholds. Extensive experimental evaluation will be presented to validate the performance of the formulations in two different full-sized biped humanoid robots.

Finally, Chapter 5 will present the discussion of the results in this thesis and an outlook of the contributions to the field of robotics.

2. Related Works, Biological Inspiration and Experimental Platforms

Physical interaction is paramount in the new applications of robotics. When robots started leaving the manufacturing cells with perfectly modeled environments, the awareness of physical interaction other than at the end effectors became a necessity. This problem has been addressed by different approaches ranging from back-drivable actuator design to torque-controlled robots and complex perception systems to achieve different levels of safe interactions of robots with the environment, operators, and other robots. Within the new technologies that enable new types of interaction with robotic systems, skin systems provide a series of sensing modalities over the whole body that are highly valuable for control purposes. This chapter presents the biological inspirations for the addition of skin to robotic systems for different purposes and the related works done in robotics for safe physical interactions in manipulation and locomotion.

This chapter is divided in four sections. Section 2.1 covers related works in robot whole-body interactions including the advances in tactile based interaction methods. Section 2.2 covers the related works in interactions required for bipedal robot balance and locomotion. It will also introduce the biological inspirations for plantar tactile feedback control that will be presented in Chapter 4. Section 2.3 will give a brief introduction to the robotic experimental platforms used in this thesis. Finally, Section 2.4 will summarize the ideas presented in this chapter.

2.1. Whole-Body Physical Interactions in Robotics

2.1.1. Physical interactions between humans and robots

In recent years, many new robot applications have emerged for tasks where, until now, it was not possible to have a robot. The main reasons are safety [17], reliability [18], or simply because the available technology could not make it feasible before. Many of these new applications require tasks where a robot must physically interact with people and dynamically changing environments [19], for example, medical robotics [20, 21], nursery robots [22], robot-assisted manufacture [23], home assistance robotics [24, 9, 25] and social interaction [26, 27].

Interaction with humans in unstructured environments, require robots to have a reliable way to perceive the surrounding objects to prevent collisions. In addition, a robot must avoid collisions with its own body and most importantly, when human beings are present, it must behave compliantly to external stimuli during the process, [28, 29, 11]. As a strategy to handle these interactions, force-torque control methods have emerged to soften the rigid body structure of a robotic arm as in [30], and [31]. A remarkable example of this approach is the KUKA lightweight arm [32] which incorporates high-resolution torque sensors in every

joint of a 7 DoF arm. This design allows an accurate estimation of the robot state at the effort level which facilitates the distinction between the actuation torques and the torques produced by external interactions on the whole body. Therefore, despite requiring complex mechanical designs, the joint torque sensor approach is gaining popularity for service robots as [13]. As a result, indirect detection of the collisions with the environment is possible, and different reactions can be triggered depending on the intensity of the contact forces [33]. However, this kind of implementation requires precise modeling, complex control laws, and high-cost sensors and actuators.

Another approach to achieve safe physical interaction on robots is through hardware-compliant actuators using spring-based joints and soft materials in the design. The series elastic actuators [34] are a clear example of this approach. Adding an elastic coupling between the actuator and the interface provides the advantages of shock tolerance, lower reflected inertia, more accurate and stable force control, less inadvertent damage to the environment, and the capacity for energy storage. These designs absorb sudden contacts and impacts among the links of a robot as in [35], and [36] improving the safety of the interactions. However, the passive elements in the design make the modeling more complicated and increase the difficulty for precise control.

The concept of robot skin has also been developed to sense contact forces on the links and take actions to induce compliant behavior on stiff robot designs. Different sensing technologies have been utilized for skin purposes as in [37, 38, 39, 40]. The direct measurement of external forces provides the needed information for whole-body reactive control with stiff (position commanded) robots as described in [41, 5].

2.1.2. Physical interactions enabled by robot skin

The human body is completely covered with different types of skin which, aside from protecting us from the environment, provide meaningful information of our interactions with the environment. We use tactile information for different purposes depending on the nature of the interaction forces and the location of the stimuli over our body. For example, we use the information from the foot sole skin for walking and balance, the skin on our hands to explore the environment, and the body skin to watch our physical integrity and interact with others. Similarly, robotic systems can benefit from stimuli information if they can have access to it. This was the motivation to develop robot skin systems. Covering robots with tactile sensors brings a direct measurement of the external forces applied on any part of the robot and not only in selected frames where force-torque sensors are mounted. Nevertheless, skin systems come with a series of challenges that must be addressed to profit from tactile information.

As pointed in Section 1.1, robot skins are distributed sensing systems made up of a series of *tactile sensing* elements commonly known as *taxels*, and the communication and interfacing channels with a robot [42, 43]. A key feature of robot skins is the *spatial distribution* of the tactile sensors. While classic force-torque sensors provide a fast and accurate measurement

of the resultant wrench at the mounting coordinate frame, robot skins provide a discrete capture of the interaction forces over the surface where they are mounted.

The position of the taxels over the robot's links can be obtained utilizing different spatial calibration methods as [44], and [45]. Furthermore, these large arrays of sensors produce wide streams of data that represent another challenge for computing systems. However, neuromorphic paradigms make it feasible to acquire and handle the sensor data [46] but these techniques require the control algorithms to comply with their requirements.

Different sensing technologies have been applied to robot skins in the last decades. Primarily for sensing contact force and pressure, several transduction principles are exploited to build different types of tactile sensors (e. g. mechanical, resistive, capacitive, optical, piezoelectric, etc. [47]). Additionally, other sensing modalities have been included in tactile sensors. For example, contact temperature [48], proximity to objects [49, 50], and humidity [51].

Multi-modal tactile information helped implement behaviors in robots that were not possible with simple force-torque sensors. One clear example is the dexterous in-hand manipulation of complex shaped objects as described in [52]. Tactile feedback enabled whole body compliance without the need for joint torque sensing for fixed base and mobile base robots as in [5]. It also allowed the real-time estimation of in-hand object properties as in [53] and the robot state as in [54]. Having a direct measurement of the interaction forces and their location over the robot links gives advantages for different applications which include whole-body physical interaction with humans and complex environments [23], social interaction by meaningful contacts [55], biped balance and locomotion [56], robot nociception [57], among others.

2.1.3. Collision avoidance for safe interactions

For mechanically less complicated robot designs that cannot detect external contacts on other parts than the end-effector, the usual strategy is to avoid contacts all the time as a safety condition. The problem of avoiding self-collisions and impacts with the environment has been tackled using model-based approaches as [58, 59, 60] and [61]. These approaches require a geometric mapping of the robot and the environment to evaluate repulsive potential functions between the robot links and the surrounding objects. Simplified geometric models are often used in such methods to reduce the computational load and also to ensure a non-interaction virtual layer surrounding all the body parts of the robot and the detected objects. The success of these approaches relies on an accurate perception of the environment, then for unstructured and changing scenarios, complex perception systems are required, which often increase the computing demands.

When the environment is uncertain or constantly changing, it requires a continuous perception of its geometry to compute the repulsive forces that keep the robot's links away from them. This problem has been approached with machine vision systems as proposed in [62, 63], and [64]. This type of feedback is fast and accurate with modern vision systems but is severely

affected by occlusions in complex environments. To prevent occlusions, proximity sensing distributed over the body has been adapted, such as the successful navigation methods in mobile robots as proposed in [65]. Cheung and Lumelsky mounted opto-whisker sensors (infrared range finders) at the center of the larger links of a manipulator to keep a safe distance from the environment during reaching tasks. Further approaches use other types of proximity sensors, such as capacitive [49] or ultrasonic [66]. Latter implementations took advantage of the miniaturization of proximity sensors adding more sensing points over the robot's body, such as the 50 sensors on a robot in [50].

2.1.4. Whole-body physical interactions with the environment

Distributed contact or proximity sensing over the body allows a robot to adapt to the environment while pursuing a purposeful task with its end effector. For these cases, redundant robots can operate when the environment imposes several constraints on the task. The more degrees of freedom a robot has, the more simultaneous tasks it can perform. However, a task priority assignment is needed to define which ones can be executed and which ones cannot when the robot kinematics are overconstrained.

There are different methods to achieve the execution of a set of tasks according to the established hierarchy. For instance, null space projection methods use the remaining degrees of freedom available after fulfilling all the higher priority tasks to accomplish lower priority tasks. This can be done by defining null-space projectors between the tasks' workspaces as in [67] and [68]. Another way to implement this approach is using a chain of quadratic problems using the results of a higher priority task as restrictions for lower priority tasks [69] and [70]. These methods helped define and realize the tactile-based tasks defined in this work, as will be detailed in Chapter 3.

2.1.5. Meaning of contacts during physical interaction

With the new capabilities for physical interaction, it became feasible to have collaboration in shared space between humans and robots. However, the contacts with the environment are different from the contacts with human collaborators and these are different from self-collisions. Furthermore, contacts with the different parts of the human body are also different from one another [33]. Therefore, contacts have different meanings and purposes during physical interaction. Furthermore, with more information about them, a system can generate better reactive behaviors and make smarter decisions. For example, contacts can be produced by hard or soft collisions between the robot and the environment. In such cases, the robot must behave compliantly as in [71] to prevent damage. Moreover, when the collision occurs with a human being, a robot shall distinguish the case and show a different compliant reaction. Clear examples are the nursery robots of [22]. These robots are intended to handle human bodies which are heavy, bulky, and sensitive. In this kind of application, interaction forces are high (the weight of a human adult) but shall not be concentrated in small areas because such conditions may lead to injuries in the human body. The same condition applies for handling other kinds of heavy and bulky objects as in [72]. Therefore, the commonly used

force-sensing technologies and techniques lack sensitivity for this kind of application, and thus, new technologies must be considered for further development.

Different features help to classify contacts. For instance, the timing and frequency components of the force profile are used to identify different human-robot interaction cases in [73], the contact force magnitude is used to distinguish the interaction of the robot with mobile or fixed obstacles in [74], and the thermal pattern is used to identify contacts with persons or objects in [75]. Contacts can also be used to learn the dynamic parameters of the robot and the environment as in [76]. Visual perception can help identify humans in the environment to make a distinction between their intentional contacts with the robot and other environmental contacts as described in [77], and [78]. Tactile sensors are a good approach to acquire complementary information to identify the different meanings of contacts. State-of-the-art skin systems provide additional sensing modalities to complement contact force sensing. For example, contact temperature [48], proximity to objects [49, 50], and humidity [51].

Adding more sensing modalities to robots increase their awareness of the environment and the collaborators, either humans or other robots. But it is not all, the additional information also helps estimate the internal states of the robot. For example, acceleration information produced by robot skin was used to estimate the full second-order kinematic state of a floating base humanoid robot in [54]. Several additional sensing modalities can provide artificial nociception for robots to guarantee the operation under safe conditions to preserve the life span of a robot as described in [79], and [80]. Similar to humans and animals, robots can benefit from multiple sensing modalities distributed on the body to adapt the body behaviors for a wide span of physical interactions including those that are dangerous for the robot itself and its surrounding collaborators. In Chapter 3, we propose controllers for physical interaction that combine sensing modalities of proprioceptive and exteroceptive sensors. Section 3.4 will present two examples of whole body behaviors that combine direct and virtual interactions together.

2.2. Physical Interactions for Locomotion

2.2.1. Biped balance and locomotion

In the previous section, we described the importance of physical interactions for cooperation and safety. However, there is another set of physical interactions that are crucial for any robotic system with legs: locomotion. While manipulation interactions consist of exerting forces to inject momentum into an external body, locomotion interactions consist of exerting forces to presumably fixed surfaces to inject momentum into one's body. In reality, legged locomotion is a complex self-organizing process that requires the coordinated efforts of several elements of the body and involves strong and intermittent physical interaction between the feet and the ground [81]. Let us focus on biped balance and walking, which is the human way of locomotion and thus of humanoid robots.

Humanoid robot's biped balance and locomotion is a challenging task due to the naturally unstable dynamics of floating base systems. Its difficulty increases, even more, when the terrain is not flat and structured. In such conditions, walking controllers must be adapted to the terrain either by mapping the terrain to plan a set of footholds [82, 83, 84] or by reacting compliantly to the terrain modifying the footholds on-line [85, 86, 87, 88, 89].

Different methods have been developed for mapping the terrain looking for suitable footholds by using cameras [82], laser scanners [83] or exploratory motions [84]. With a full 3D map of the terrain, Griffin et. al. [90] achieved a footstep planned that can coup with rough terrain conditions and even narrow passages barely larger than the foot sole.

State of the art walking controllers require the measurement and control of the reaction forces exerted by the robot's feet on the terrain. The classic approach is to include ankle force-torque sensors in the leg design to have a direct measurement of the resultant wrench at the mounting point. With these sensors, a robot can estimate the significant metrics for balance and locomotion which are sufficient for walking over flat ground. These metrics include the ZMP, CMP, GRF, among others. With ankle feedback, different controllers for flat and uneven terrain have been proposed [85, 86, 87, 91, 92].

For more complicated terrain conditions, as deformable terrain or small footholds, the ankle sensors must be combined with other means to feel the terrain and adapt the footholds for walking. One example is the inclusion of contact switches at the borders of the sole as in [93] where the LOLA robot detects early contact to adapt the foot impedance and the step timing. Wiedebach et. al. [94] present a method for walking on small footholds which uses exploratory foot motions to map the geometry of the supporting surfaces and fast stepping motions to go from one to the next. Fully-torque controllable robot designs have been implemented for rough terrain conditions combining joint-torque measurements with ankle force-torque sensors as in the work done by Mesesan et. al. [95]. However, these robots neither can map the terrain geometry without exploratory motions and rely entirely on body-impedance control to keep balance. Not to mention that including torque sensors in each joint is expensive and increases the complexity of the robot's design.

In this thesis, a biologically-motivated approach for terrain sensing is presented by mounting robot skin [7, 1, 5] on the foot soles of robots without modifying the foot design. The plantar robot skin can be used to estimate all the states that are required for balance and locomotion [96, 97] (e.g. CoP (Center of Pressure), ZMP, and CMP). Besides, it provides complementary information that ankle force-torque sensors cannot by exploiting the additional sensing modalities. For example, the spatial distribution of force sensors in the robot skin enables the reconstruction of the footprint's pressure distribution and thus an accurate shape of the supporting polygon. In the following sections, the motivation and details of the plantar skin sensor are presented as well as its capabilities to improve biped balance and locomotion.

2.2.2. Biological inspiration for plantar skin

The postural equilibrium of a human being results from a complex synergy of sensation and actuation [98]. It is a dynamic phenomenon that keeps the center of gravity oscillating over the standing feet by the application of antagonistic muscular reflexes triggered by different stimuli [99]. This balance depends on a complex fusion of visual, vestibular, proprioceptive, and exteroceptive feedback. It is known that none of them is essential for balance, but the lack of each of these kinds of sensory feedback produces different changes in the posture and the movement patterns during stance balance [100]. Between the exteroceptive receptors, the cutaneous receptors of the foot sole play an important role in both balance and locomotion in humans [101].

The human foot sole is covered with an endurable layer of glabrous skin that apart from protecting the foot from rough surfaces, provides rich sensorial information about the terrain such as texture, hardness, temperature, and pressure distribution on the foothold. The role of its cutaneous receptors in the equilibrium control has been studied for more than a century [102]. Studies reveal that subjects with the soles anesthetized by hypothermia show increased posture sway while standing. For example in [103], the subjects presented larger amplitude oscillations while closing the eyes (Romberg's test [104]) than subjects with non-anesthetized soles. A similar result was generated in [105] when body sway was galvanically induced in the vestibular system of healthy subjects with anesthetized soles. Furthermore, the inhibition of the sense of touch in the soles also induces delays in the compensatory stepping reactions with different effects depending on the phase and the direction of the step [106].

The human sole shows various sensitivity to mechanical stimuli in different regions [101]. This is because its mechanoreceptive afferents are connected to distinct nerves to transport the data to the spinal cord [107] and because within the regions connected to one of these nerves the receptor density is not uniform and their pressure thresholds are mismatched [108]. Furthermore, the sensitivity and thresholds of these afferents change according to the phase of a footstep during walking. For example, sensitivity is increased during the single support phase on the swing foot and reduced considerably right after footfall [109].

The dynamic sensitivity of the human sole is used for triggering different muscular reflexes during standing and walking and even for defining the direction of a reflex depending on the walking phase [110]. During both standing and walking stages, the tactile stimuli are gattered by three main nerve branches: i) sural, ii) superficial peroneal, and iii) posterior tibial [107]. These nerves include location-specific information that triggers combined muscle reflexes and inhibitions. In [111], results from an experiment where subjects were walking on a treadmill indicate that during the late swing phase, a large increment of sensitivity generally occurred for the peroneal nerve, whereas sensitivity suppressions were observed for the tibial nerve.

In summary, 1) human equilibrium and locomotion rely significantly on the sense of touch provided by the mechanical afferents located on the feet. 2) these afferents are distributed with different sensitivities and thresholds along the sole. 3) the sensitivity and threshold of the afferents depend on the standing or walking phase with clear differences for the supporting and the swing leg. 4) the afferents are connected to three main nerve branches that coordinate different reflexes on muscular groups also depending on the walking phase.

2.2.3. Plantar robot skin for balance and walking

As described in the previous sections, robot skin can provide precise information about external contacts with the environment in other parts of the body than the end effectors. However, most tactile sensors are developed to provide high sensitivity at low and middle force ranges [42]. Nevertheless, to be used in locomotion, robot skin must be capable of holding the weight of a full-size biped or humanoid robot while resisting the impacts produced during walking on unknown terrain.

Different sensing technologies have been applied to robot soles to improve the performance and versatility of walking controllers. For example, resistive sensor arrays are mounted on the foot soles of small-size humanoid robots without ankle force-torque sensors to enable the direct measurement of the CoP [112, 113, 114, 115]. For bigger robot sizes (closer to human size and weight), resistive sensors are combined within the structural layers of the soles to increase the sensing range and endurance [116, 117]. Plantar resistive pressure sensors have been applied to the H7 robot [118], the HRP-2 robot [119], and the BHR-2 robot [120]. All of these robots have a mass larger than 50 kg and are capable of dynamically walking over flat terrain. The pressure grid sensors were proven capable of measuring the ZMP during all the phases of walking and served as feedback for balance. Likewise, other tactile sensing principles have been applied, like the optical measurement of rubber deformation [121] or the high-speed pressure sensor grid [118] which can acquire the pressure shape of the foothold at a frequency of 1kHz.

Furthermore, plantar tactile sensors can be combined with other sensing modalities to acquire more information on the terrain and the foot interactions. For example, the perceptual foot developed in [122] combines the classical ankle force-torque sensor design with a flexible resistive sensor array and an IMU sensor. With this foot design, the ZMP and the supporting polygon are acquired at a rate of 100 Hz and the foot orientation from the IMU sensor is used to estimate the dynamic posture of the robot while walking at the same rate. The custom MEMS sensors in [123] measure the grip force at the foot contacts. This information is used to estimate the friction coefficient between the feet and different terrain conditions including oiled surfaces. The IMU sensor in the foot design of [122] provides the spatial orientation of the foot during the swing and support phases.

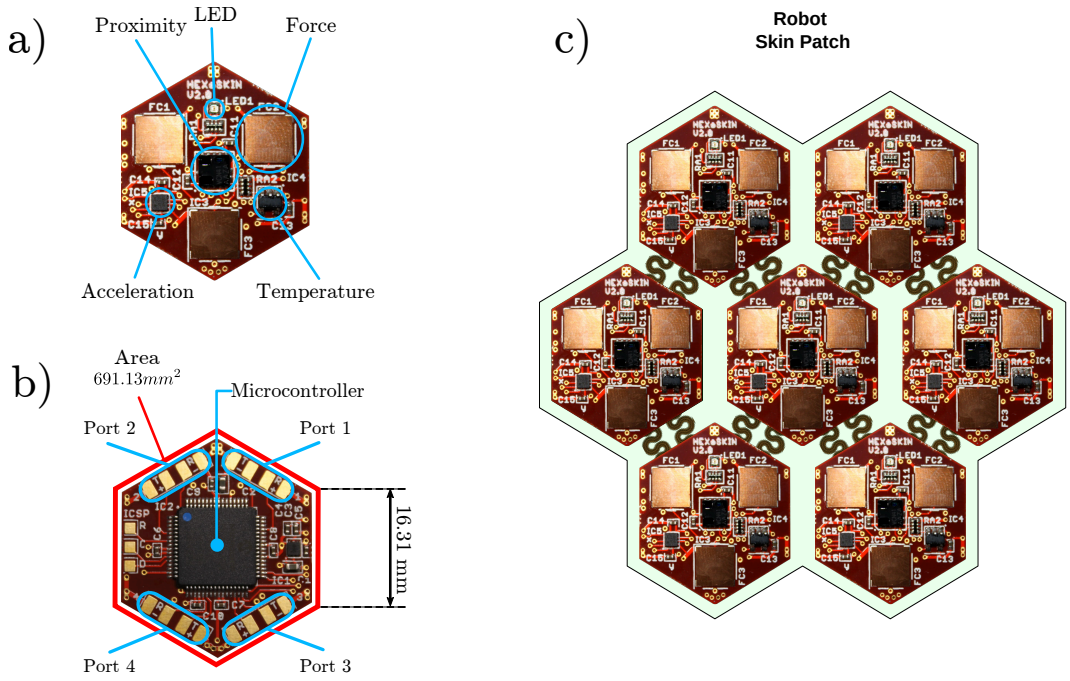

Figure 1 Robot skin developed by Mitendorfer et al. [1]. a) Each taxel has four sensing modalities: *force* $\times$ 3, 3-axis *acceleration*, *temperature* and *pre-contact* (proximity sensor). b) The data acquisition and network communication are handled by an embedded microcontroller. c) The taxels have 4 communication ports to connect with the neighboring taxels to form a dynamic communication grid in an hexagonal lattice. A group of taxels connected together form a skin patch.

2.3. Experimental Platforms Used in This Work

The formulations in this thesis were evaluated with three robotic platforms. All of them were covered with the same multimodal skin [1, 5]. As shown in Fig. 1 the hexagonal taxels provide four sensing modalities (force, proximity, temperature, and acceleration). The taxels are connected forming patches that provide uniform spatial distribution and optimal communication paths for tactile information [124]. The dimensions of the taxels and the geometry of the layout are known, acquired by a spatial calibration algorithm as shown in [45]. The tactile information is generated with an event-based neuromorphic approach [46] that sends packets of information only when significant changes in the sensor signals are detected to reduce the latency and the computational load of the host computer.

2.3.1. TOMM robot

The Tactile Omnidirectional Mobile Manipulator (TOMM) [125] is a robot designed to be an experimental platform to assess the capabilities and potential of robot skin. It is constructed with an omnidirectional mobile base with two robotic manipulators with 6 DoF (Degrees of Freedom) each as shown in Fig. 2. The arms can be controlled with position or velocity commands, but the control framework in its embedded computer is compatible with effort level control formulations. Joint torque commands are used to generate smooth joint trajectories for the hardware interface in a torque resolver module that uses the dynamic model of the whole body.

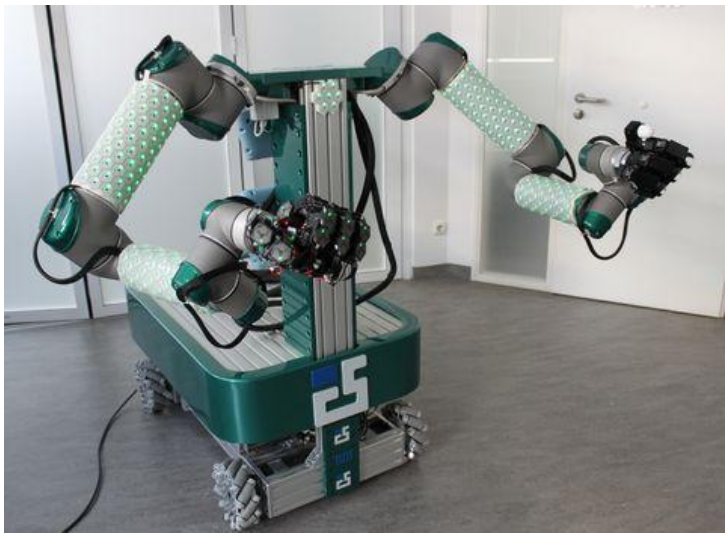

Figure 2 Experimental platform TOMM, semi-humanoid robot with two 6-DOF arms covered with artificial skin.

The arms of TOMM are fully covered with robot skin and can host different types of end effectors, including fingered hands with tactile sensors. The TOMM robot was used to test the intentional contact behavior presented in Section 3.4.2 of this thesis.

2.3.2. H1 humanoid robot

The formulations in Chapters 3 and 4 of this thesis were evaluated with a floating base biped robot fully covered with robot skin to assess their performance in large scale interactions. The robotic platform that served this purpose is the H1 robot [4, 5] as shown in Fig. 3. The H1 robot is a full-size humanoid robot fully covered with robot skin. It is a REEM-C robot from PAL Robotics, covered with 1260 taxels of the skin described in Fig. 1. Without considering the fingers, the H1 robot has 30 position controlled DoF and two embedded computers that run the $\mathrm{ros\_control}$ framework [126] with an update rate of 200 Hz. The total mass of the H1 robot with the skin system is 86 kg.

The H1 robot is controlled with the framework shown in Fig. 4. It consist of a custom walking controller based on the DCM dynamics similar to [6] as described in Section 4.1 of this thesis, and a strict hierarchical task manager built with the null-space projector method described in Section 3.1. The interconnection between these two sections is realized by a torque resolver module that computes the joint trajectory commands from the torques calculated in the task fusion module. The control framework of the H1 robot can allocate several tasks with strict priority to generate complex body behaviors that can use the interaction modalities that will be presented in Sections 3.2 and 3.3.

2.3.3. HRP-2Kai humanoid robot

The formulations for PFC (Preemptive Foot Compliance) and walking over partial footholds of this thesis were evaluated in the H1 robot. However, to assess their generality and versatility, another humanoid robot was used that runs a completely different walking controller and even

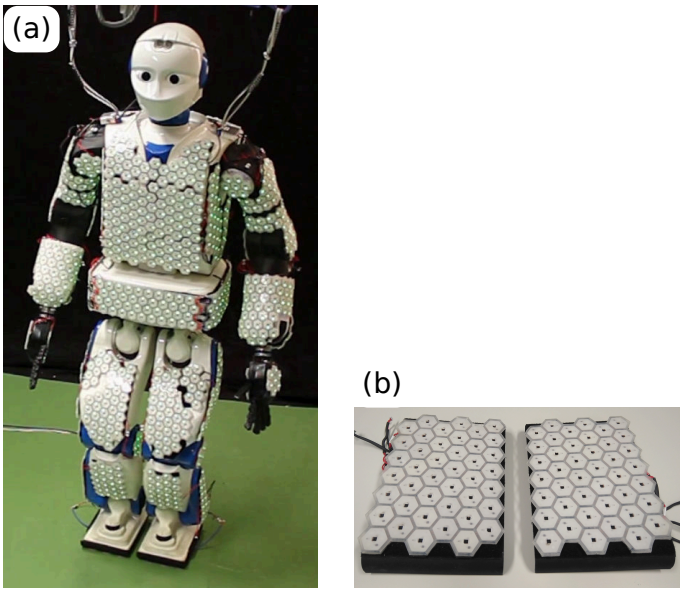

Figure 3 The H1 robot is a full-size humanoid robot fully covered with robot skin. It will be the main experimental platform for this thesis.

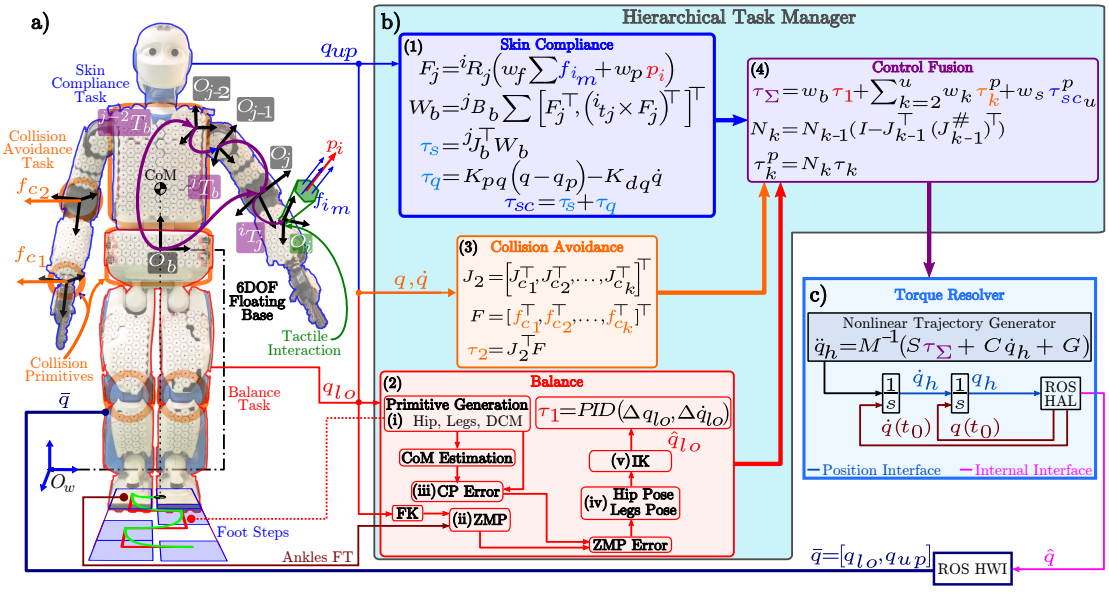

Figure 4 Controller framework in the H1 humanoid robot [2]. A prioritized task-fusion whole-body controller that combines tactile based interaction tasks, biped balance and walking control, and end-effector purpose tasks.

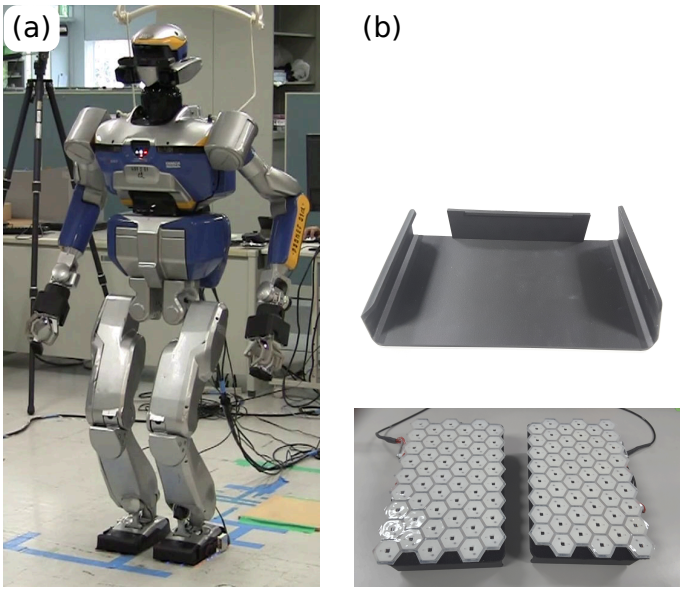

Figure 5 a)The HRP-2Kai humanoid robot [3]. b) The 3D printed tactile shoes for the HRP2-Kai robot covered with 51 taxels on each sole.

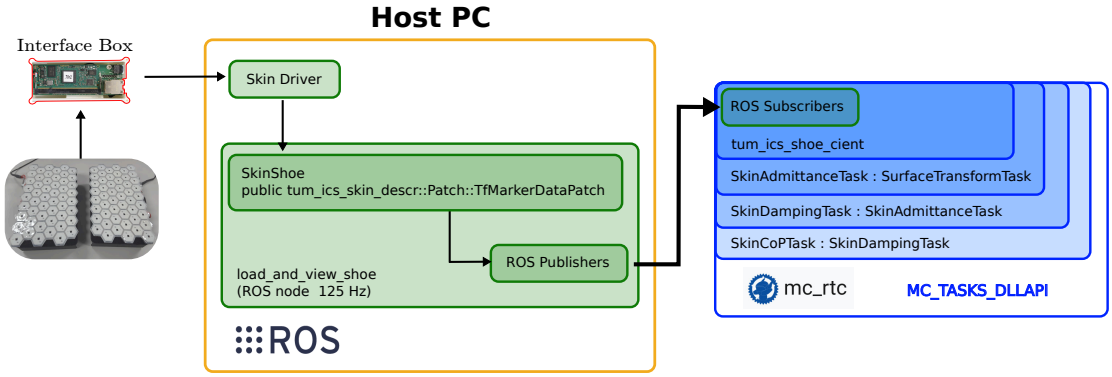

Figure 6 The plantar tactile feedback was introduced in the open source walking controller running in the HRP-2Kai robot in the mc_rtc framework by means of a bridge module using ROS publishers.

a different software framework and hardware interface. The HRP-2Kai robot [3] is the full-size humanoid robot developed by Kawada Industries, as shown in Fig. 5. Its total mass is 65 kg and also has 30 position controlled DoF.

The software running the controllers in the HRP-2Kai robot is the mc_rtc[1] framework. The formulations for plantar tactile feedback were added to the open source walking controller implemented by Caron et al. [127] [2]. The tactile information was added in the foot admittance task of the walking controller. The ZMP adjustment from the center of the supporting polygon was adapted without deep modifications to the code. As the robot skin software runs in the ROS framework, an interface module that subscribes to ROS publishers is implemented inside the mc_rtc controller, as shown in Fig. 6.

[1] https : //jrl − umi3218.github.io/mc_rtc/index.html
[2] https : //github.com/stephane − caron/lipm_walking_controller

2.4. Summary

This chapter presented the previous works and biological inspirations that helped develop the contributions of this thesis. The detailed background to construct the formulations for physical interaction will be reviewed in the first Section of Chapters 3 and 4. The classic methods for robot control focussed on interactions of the end effector with the environment. The lack of sensor information in other parts of the robot's body than the end-effector constrained the possibilities for closed-loop control. As a result, these techniques avoided contact with the environment by any chance. Nevertheless, as will be detailed in Section 3.1, the fundamentals for whole-body physical interaction come from generalizations of the methods applied for end-effector control.

Robot skins are inspired by the skin in humans and animals. Our bodies are covered with skin that, aside from protecting our internal organs, provides sensing modalities that our nerve system uses for several purposes. Skin provides feedback of mechanical pressure, temperature, and humidity. The combination of its sensing modalities can detect specific features of the environment as textures, vibrations, electric charges, and chemical reactions. In Section 3.2 and 3.3 of this work, the formulations to control interactions from multi-modal tactile feedback will be presented, including direct contact force measurement, proximity, and temperature.

When the interactions compromise the body, human skin provides means of nociception that detect these conditions and trigger muscular reflexes that prevent damage. Inspired by this behavior, Section 3.4.1 will present a control method that detects harmful stimuli and produces reaction motions to it combining interactions of different modalities. Furthermore, The idea of combining interactions of different modalities will be applied to enable an active exploration behavior for robots in Section 3.4.2.

The skin plays an important role in the process of human walking. It provides feedback on the ground reaction forces and helps synchronize the muscular reflexes that generate the walking cycle. The plantar skin gives spatial and temporal information of the foot-ground interactions that help modulate the tension in the antagonistic muscles of the ankles and the knees. These observations inspired the concept of plantar skin for robots. Chapter 4 will present the methods required include plantar tactile feedback in biped balance and walking control.

3. Tactile-Based Close Interactions

This chapter presents the formulations for whole-body physical interactions based on different sensing modalities, specifically, tactile-based close interactions. We use the operational space formulation from Khatib [128] with direct force feedback to generate whole-body compliance on stiff (position or velocity controlled) robots. For interactive tasks, the direct force feedback comes from wrist force-torque sensors or robot skins. The distributed force sensing capability of robot skins allows the formulation to be applied over all the links of a robot that have taxels mounted. During complex interactions, multiple contacts are treated as independent tasks and combined to generate whole-body reaction torques that minimize the force at each contact point.

Task fusion with strict priority is achieved by means of nested augmented null-space projectors, following the formulations proposed by Sentis et al. [129] which account for supporting contacts to define constraint tasks with the highest priority. Strict prioritization of the tasks with support constraint is paramount for floating base robots (e. g., biped humanoid robots) to guarantee postural stability and balance during physical interaction. In addition, prioritized task execution allows giving preference to the reaction motions of a limb over the others by assigning a higher priority in the stack. For skins with multiple sensing modalities, different priorities can also be imposed independently according to the needs of the applications.

For skin systems with multiple sensing modalities, this chapter will provide the formulations for virtual interactions that involve no physical contact between the robot and the environment. These types of interactions generate virtual forces proportional to sensor measurements of, for example, the temperature of the environment or the proximity of an object to the robot's body. Nevertheless, a distinction between virtual and direct physical interaction must be clear to keep the postural stability of the robot during the interaction. This distinction is crucial when controlling floating base robots where the supporting contacts provide the actuation for balance control. Therefore, direct physical interaction must be taken into account when controlling the supporting contacts. Moreover, as this chapter will propose, we can combine direct and virtual interactions to generate versatile body behaviors in both fixed and floating base robots.

Different sensing modalities working together over whole body tasks enable complex behaviors which can fit specific applications that require environmental awareness. In this chapter, we will also present rules to change the priority of the tasks from interaction conditions to cancel the execution of a task when the situation puts the robot's integrity at risk as presented in [57, 74]. The main goal of this chapter is to set the basic definitions to develop new interaction modalities from new sensing modalities that robot skins will include in the future.

This chapter is presented as follows: Section 3.1 will summarize the operational space formulation and the common methods for task fusion. Section 3.2 presents the formulation of direct interaction tasks that involve physical contact between the robot and the environment. Section 3.3 introduces the formulations to exploit sensing modalities that do not involve direct physical contact with the environment, e. g. temperature. Section 3.4 combines both modalities of interaction into composed whole-body behaviors, it presents two means to generate priority adjustment in the tasks according to interaction conditions. Two different behaviors are generated with this approach: *Robot Nociception*, and *Intentional Contact*. Finally, Section 3.5 summarizes the results and contributions of this chapter.

3.1. Background on Prioritized Whole-Body Control

The operational space formulation proposed by Khatib [128] provides a useful framework to model the dynamic interactions of the end effector of a robot in different spaces, and the mapping to transform these interactions into the generalized joint space. The core formulation that we will adapt in this work is the definition of an interaction task. Let us review the key elements of the task formulation and prioritized task fusion into whole-body control.

3.1.1. Interaction tasks in the operational space

A standard representation of a robotic system with n DoF in generalized coordinates is defined as

$$\mathbf{M}(\boldsymbol{q})\,\ddot{\boldsymbol{q}} + \mathbf{c}(\boldsymbol{q}, \dot{\boldsymbol{q}}) + \mathbf{g}(\boldsymbol{q}) = \boldsymbol{\tau} \tag{3.1}$$

being $\boldsymbol{q} \in \mathbb{R}^n$ the position of the system in generalized coordinates, $\dot{\boldsymbol{q}} \in \mathbb{R}^n$ is the velocity and $\ddot{\boldsymbol{q}} \in \mathbb{R}^n$ the acceleration also in generalized coordinates. $\mathbf{M}(\boldsymbol{q}) \in \mathbb{R}^{n\times n}$ is the symmetric and positive definite inertia matrix, $\mathbf{c}(\boldsymbol{q}, \dot{\boldsymbol{q}}) \in \mathbb{R}^n$ is a vector composed by all the centrifugal and Coriolis joint torques, $\mathbf{g}(\boldsymbol{q}) \in \mathbb{R}^n$ is the vector of joint torques produced by gravity, and $\boldsymbol{\tau} \in \mathbb{R}^n$ is a vector of input torques.

Let us define a task $\boldsymbol{x} \in \mathbb{R}^m$ as a purpose defined state in a specific space. The motion in the task space can be mapped into the generalized joint space by the Jacobian matrix $\mathbf{J}(\boldsymbol{q}) = \dfrac{\partial \boldsymbol{x}}{\partial \boldsymbol{q}} \in \mathbb{R}^{m\times n}$ as

$$\dot{\boldsymbol{x}} = \mathbf{J}(\boldsymbol{q})\dot{\boldsymbol{q}} \tag{3.2}$$

where $\dot{\boldsymbol{x}} \in \mathbb{R}^m$ is the motion in the task space. Here we must highlight that the executability of task $\boldsymbol{x}$ requires that its dimension is $m \leq n$, and the Jacobian matrix is non-singular, and thus has full row rank.

To produce variations in $\boldsymbol{x}$, and $\dot{\boldsymbol{x}}$, let us introduce an effort term $\boldsymbol{f} \in \mathbb{R}^m$ such that the dynamics of the task are described as

$$\boldsymbol{f} = \boldsymbol{\Lambda}(\boldsymbol{x})\ddot{\boldsymbol{x}} + \sigma(\boldsymbol{x}, \dot{\boldsymbol{x}}) + \varrho(\boldsymbol{x}) \tag{3.3}$$

where $\mathbf{\Lambda} \in \mathbb{R}^{m \times m}$ is an imposed positive definite task inertia matrix, $\sigma(\boldsymbol{x}, \dot{\boldsymbol{x}}) \in \mathbb{R}^m$ is the vector of centrifugal and Coriolis task forces, and $\varrho(\boldsymbol{x}) \in \mathbb{R}^m$ is the vector of task gravitational forces. At the effort level, the interconnection between Eq. (3.1) and (3.3) can be established by the relations

$$\begin{aligned} \mathbf{\Lambda}(\boldsymbol{x}) &= \left(\mathbf{J}(\boldsymbol{q})\mathbf{M}^{-1}(\boldsymbol{q})\mathbf{J}^{\top}(\boldsymbol{q})\right)^{-1} \\ \sigma(\boldsymbol{x}, \dot{\boldsymbol{x}}) &= \mathbf{J}(\boldsymbol{q})^{\dagger\top}\left(\dot{\mathbf{M}}\dot{\boldsymbol{q}} - l(\boldsymbol{q}, \dot{\boldsymbol{q}})\right) - \mathbf{\Lambda}(\boldsymbol{x})\dot{\mathbf{J}}(\mathbf{q})\dot{\boldsymbol{q}} \\ \varrho(\boldsymbol{x})(\boldsymbol{q}) &= \mathbf{J}(\boldsymbol{q})^{\dagger\top}\mathbf{g} \end{aligned}$$

as shown in [128], where $l(\boldsymbol{q}, \dot{\boldsymbol{q}})$ describes the Coriolis torques calculated row-wise as

$$l_i(\boldsymbol{q}, \dot{\boldsymbol{q}}) = \frac{1}{2}\dot{\boldsymbol{q}}^{\top}\mathbf{M}_{qi}(\boldsymbol{q})\dot{\boldsymbol{q}} \qquad i = 1, ..., n$$

The subscript $(\bullet)_{qi}$ indicates the partial derivative with respect to the i-th joint coordinate, and the operator $(\bullet)^{\dagger}$ represents the generalized inverse of $(\bullet)$. The force mapping from task space to joint space can be derived from a static instance of the model with $\dot{\boldsymbol{q}} = 0$, and $\ddot{\boldsymbol{q}} = 0$, by

$$\boldsymbol{\tau} = \mathbf{J}(\boldsymbol{q})^{\top}\boldsymbol{f} \tag{3.4}$$

which is the key formulation for the physical interaction tasks.

3.1.2. Fusion of interaction tasks

Several tasks can be defined using Eq. (3.4). The practicality of this formulation lays in the fact that the tasks can be defined in different spaces and the mapping allows us to combine them in the joint space. Therefore, we can define the i-th task in a set of k tasks as

$$\boldsymbol{\tau}_i = \mathbf{J}_i(\boldsymbol{q})^{\top}\boldsymbol{f}_i \tag{3.5}$$

This task has an associated interaction force $\boldsymbol{f}_i$, a Jacobian matrix $\mathbf{J}_i(\boldsymbol{q})$, and produces a joint torque $\boldsymbol{\tau}_i$ in the robot. A straightforward method to combine the joint torques of the k tasks is by a weighted sum

$$\boldsymbol{\tau}_{\Sigma} = \sum_{i=1}^{k} \mathbf{W}_i\boldsymbol{\tau}_i \tag{3.6}$$

$\mathbf{W}_i \in \mathbb{R}^{n \times n}$ are diagonal weight matrices that ponderate the contribution of the task into the torque of every joint. However, summing the torque contributions of all the tasks can cause execution conflicts between the tasks that produce antagonistic reaction motions. Such conditions keep these tasks from being accomplished and the robot behavior will not fulfill the expectations of the application. Tuning the weight matrices help prioritizing the execution of some tasks or a task over the others but the parasitic torques of the low weight tasks will always produce disturbances in the highly prioritized task.

When $m_i < n$, the task is executed in a subspace of the joint space of dimension n. Such a case is produced by a kinematic redundancy which means that the joint space has a residual

space of dimension $m_i - n$ while executing a m_i dimension task. These remaining DoF can be exploited to execute other tasks within the null-space of $\boldsymbol{x}_i$ in $\boldsymbol{q}$.

Let us define a priority rule for a set of tasks. Each task will have a priority $i \in \mathbb{N}$ in the set. In all the following formulations, $i_a < i_b$ implies that i_a has a higher priority than i_b and thus the highest priority is $i = 1$. In order to project the i task in the null-space of the $i-1$ task, a dynamically consistent null space projector recursion is defined as

$$\mathbf{N}_i(\boldsymbol{q}) = \mathbf{N}_{i-1}(\boldsymbol{q}) \left(\mathbf{I} - \mathbf{J}_{i-1}(\boldsymbol{q})^\top (\mathbf{J}_{i-1}(\boldsymbol{q})^\dagger)^\top \right) \tag{3.7}$$

where $\mathbf{I}$ is the $n \times n$ identity matrix. Then, the prioritized task execution is imposed as

$$\boldsymbol{\tau}_{total} = \sum_{i=1}^{k} \mathbf{N}_i \boldsymbol{\tau}_i \tag{3.8}$$

The recursive formulation of Eq. (3.7) implies that $\mathbf{N}_1 = I$ which means that the highest priority task can dispose of all the DoF it needs to be executed and thus it will be fulfilled as long as $m_1 < n$. However, the use of $\mathbf{J}_{i-1}(\boldsymbol{q})$ only guarantees orthogonality of task i with respect to task $i-1$ but not to higher priority tasks. Therefore, task i will disturb all the tasks $i-a$ for all $a > 1$. To prevent this, the calculation of the i-th null-space projector must account for all the higher priority tasks. This is achieved by using an augmented Jacobian matrix [130] instead of the task Jacobian in the calculation.

Let us define the augmented Jacobian matrix of the i-th task as

$$\hat{\mathbf{J}}_i(\boldsymbol{q}) = \begin{bmatrix} \mathbf{J}_1(\boldsymbol{q}) \\ \mathbf{J}_2(\boldsymbol{q}) \\ \vdots \\ \mathbf{J}_i(\boldsymbol{q}) \end{bmatrix} \tag{3.9}$$

With this matrix, we can compute the null-space of all the higher priority tasks simultaneously to project the next task into it. The augmented null-space projector for the i-th task is then defined as

$$\hat{\mathbf{N}}_i(\boldsymbol{q}) = \mathbf{I} - \hat{\mathbf{J}}_{i-1}(\boldsymbol{q})^\top (\hat{\mathbf{J}}_{i-1}(\boldsymbol{q})^\dagger)^\top \tag{3.10}$$

and the resultant joint torque for the task set is

$$\boldsymbol{\tau}_{total} = \sum_{i=1}^{k} \hat{\mathbf{N}}_i \boldsymbol{\tau}_i \tag{3.11}$$

With this formulation, the more tasks in the set, the larger the dimension of the augmented Jacobian of the lower priority tasks, and thus the larger the number of calculations to obtain

it. However, as proposed in [130], recursive formulation for $\hat{\mathbf{J}}_i(\boldsymbol{q})$ and $\hat{\mathbf{N}}_i(\boldsymbol{q})$ can make the process more efficient as

$$\begin{aligned} \hat{\mathbf{J}}_i(\boldsymbol{q}) &= \mathbf{J}_i \hat{\mathbf{N}}_i(\boldsymbol{q})^\top \\ \hat{\mathbf{N}}_i(\boldsymbol{q}) &= \hat{\mathbf{N}}_{i-1}(\boldsymbol{q}) \left(\mathbf{I} - \hat{\mathbf{J}}_{i-1}(\boldsymbol{q})^\top (\hat{\mathbf{J}}_{i-1}(\boldsymbol{q})^\dagger)^\top \right) \end{aligned}$$

With the null-space projector methods for task fusion, a series of tasks in different spaces can be combined with strict prioritization, with the guarantee that a lower priority task is completely orthogonal to the higher priority tasks in the joint space. This allows to define whole-body behaviors by assigning a set of tasks to fulfill the needs of an application, and when it is required, rearrange the task set according to the task states as will be proposed in Sections 3.4.1, and 3.4.2.

3.1.3. Task fusion for floating base robots

The previous formulations apply for fixed-base manipulators. However, when the base is not attached to the ground, as in the case of legged robots (e. g. a biped humanoid robot as the H1 robot described in Section 2.3.2) an additional constraint for the interactions in the legs must be considered.

Sentis and Khatib proposed a generalization for task fusion in floating base systems in [131] by defining constraint tasks in the hierarchy for the supporting contacts with the highest possible priority. In contrast to Eq. (3.1), a floating base robot representation must include the state of the floating base. Furthermore, as the DoF of the floating base is underactuated, the only means to produce variations in them is by applying external forces that produce motion to the center of mass of the robot. In legged robots, these forces come from the supporting contacts. These contacts allow producing forces in the floating base state by generating forces in the actuated joints of the legs. Let us rewrite Eq. (3.1) to include the floating base state and the supporting contacts using the task formulation in Eq. (3.4).

$$\mathbf{M}(\boldsymbol{\chi})\,\dot{\boldsymbol{\nu}} + \mathbf{c}(\boldsymbol{\chi}, \boldsymbol{\nu}) + \mathbf{g}(\boldsymbol{\chi}) = \mathbf{S}^\top \tau + \mathbf{J}_{support}^\top \boldsymbol{f}_{support} \tag{3.12}$$

where $\boldsymbol{\chi}$ is the state vector describing both the floating base position and orientation and the joint states. $\boldsymbol{\nu} \in \mathbb{R}^{n+6}$ is the complete velocity coordinates, containing the floating base's linear and rotational velocities, and joint velocities. $\dot{\boldsymbol{\nu}} \in \mathbb{R}^{n+6}$ is the time derivative of $\boldsymbol{\nu}$. $\mathbf{M}(\boldsymbol{\chi})$, $\mathbf{c}(\boldsymbol{\chi}, \boldsymbol{\nu})$ and $\mathbf{g}(\boldsymbol{\chi})$ are the inertia matrix, Coriolis and gravity effects vectors respectively. $\mathbf{J}_{support}$ and $\boldsymbol{f}_{support}$ are the Jacobian matrices and the force vector of the supporting contact points. $\mathbf{S} = [O\ I]$ is the actuated joint selection matrix. Note that $\boldsymbol{\chi}$ not necessarily has all its elements in $\mathbb{R}$ and $\dot{\boldsymbol{\chi}} \neq \boldsymbol{\nu}$.

In these systems, physical integrity depends on keeping a stable posture at all times. Therefore, the forces at the supporting contacts must be kept in controlled equilibrium. Consequently, any interaction tasks must be executed in a way that this equilibrium is not disturbed. Thus, all the interaction tasks must be executed in the null space of all the supporting contact

tasks.

$$\boldsymbol{\tau} = \boldsymbol{\tau}_{support} + \mathbf{N}_{support} \left(\tau_1 + N_2 \left(\tau_2 + ... + \mathbf{N}_m \tau_m ... \right) \right) \tag{3.13}$$

where $\boldsymbol{\tau}_{support}$ is the torque vector generated by the supporting contacts, and $\mathbf{N}_{support}$ is the dynamically consistent null-space projector to execute the lower priority tasks in the null-space of the supporting tasks. With this scheme, the interaction tasks can take any priority from 1 to m in order to keep the stability of the system.

3.2. Formulation of Direct Interaction Tasks

The operational space formulation described in the previous section provides a powerful framework to design controllers for a specific point of a manipulator. The geometric map with the Jacobian matrix allows the definition of the controlled point where the task forces are produced. In most cases, this point lays on the end effector geometry for two main reasons: 1) the end effector has the highest manipulability space of the whole robot, and 2) It is where force-torque sensors are mounted for direct feedback. However, in human-robot collaboration, interaction contacts are likely to occur in any part of the robot's body. Direct feedback of the contact forces over the whole body is possible by using tactile sensors and robot skins as in [1, 132, 44].

Dean et al. [44] proposed a controller using direct input of contact force over the whole body of a fixed base manipulator. The artificial compliant behavior achieved in that work proved the possibility of turning a stiff robot into a soft robot with direct tactile feedback. However, the implementation with that approach is computationally expensive because, for every taxel, a contact Jacobian and a whole-body torque are computed. For larger robots, that approach cannot be realized due to the number of operations required to compute the Jacobian matrices. Therefore, a different task formulation is required to cope with several hundreds of taxels mounted on large kinematic chains. One example is the method proposed by Leboutet et al. [133] where the interaction forces from several taxels are combined in a resultant force applied at the centroid of the contact geometry. Let us then define a general interaction task for robots with large-scale skin systems.

The formulations in this section will be detailed using the robot skin developed by previous works at the Institute for Cognitive Systems (ICS) [1, 5] (see Fig. 1). However, they can be applied to any skin technology that provides direct force sensing and spatial localization of the contact points [134, 135].

3.2.1. Kinematic modeling of interaction tasks

As described in Section 2.1.2, a minimum sensing element in a robot skin system, namely a tactile pixel or *taxel*, in this case, the taxel is a piece of hardware that holds a group of sensors within a pre-defined area. In every taxel, the minimal sensing modality required is force sensing. The geometric parameters of a taxel are known by the hardware design and

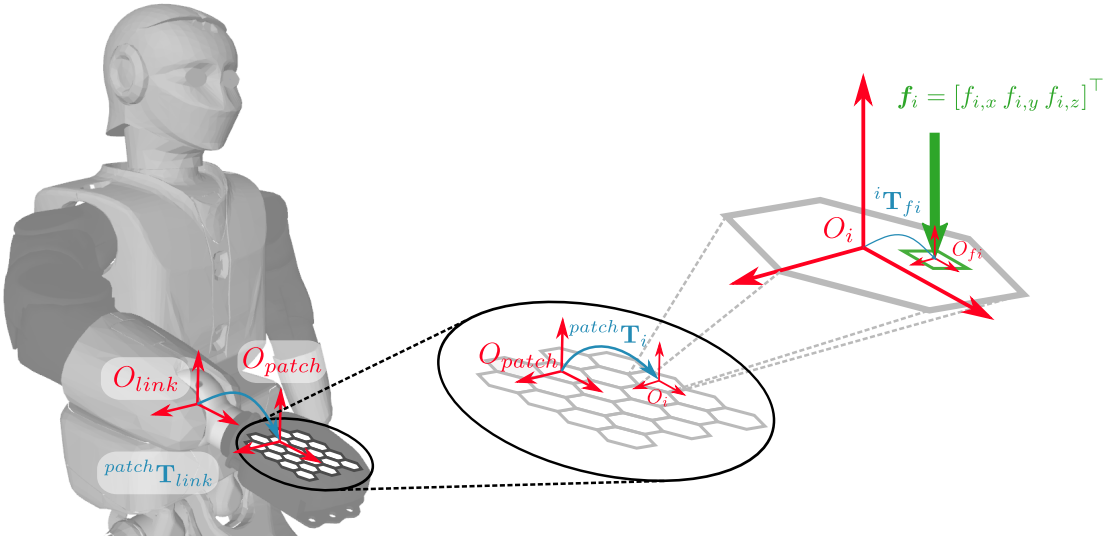

Figure 7 Kinematic description of a taxel in a pacth, mounted on a link of the robot.

the industrial processes required to manufacture it. To cover a surface on a robot, taxels are connected as shown in Fig. 1-c to form patches. A patch is a group of taxels connected, commonly in a uniform lattice shape. Therefore, we can define a coordinate frame O_i at the i-th taxel in a patch as shown in Fig. 7.

The force sensor in the i-th taxel measures the contact force $\boldsymbol{f}_i \in \mathbb{R}^3$. If the sensor only provides a measurement of the normal force, the contact force can be constructed as $\boldsymbol{f}_i = [0, 0, f_i]^\top$. In the taxel, the force sensor is mounted at the origin of the coordinate frame O_{f_i}, and the homogeneous transformation ${}^{i}\mathbf{T}_{f_i} \in SE(3)$ from O_{f_i} to O_i is known. To localize the taxel in the patch, a patch coordinate frame O_{patch} can be defined within the area covered by the patch. Then, the homogeneous transformation ${}^{patch}\mathbf{T}_i$ from O_i to O_{patch} must also be known. The location of a patch in the kinematic chain of a robot is defined by the transformation ${}^{link}\mathbf{T}_{patch}$ from O_{patch} to the coordinate frame of the link where the patch is mounted O_{link}. This information can be obtained by spatial calibration methods as in [45], and [44]. With the kinematic information of the taxels and the patches, we can find the transformation from the contact coordinate frame O_i to O_{link} as

$$ {}^{link}\mathbf{T}_{f_i} = {}^{link}\mathbf{T}_{patch}\ {}^{patch}\mathbf{T}_i\ {}^{i}\mathbf{T}_{f_i} \tag{3.14} $$

which is composed by the rotation ${}^{link}\mathbf{R}_{f_i} \in SO(3)$ and the translation ${}^{link}\mathbf{r}_{f_i} \in \mathbb{R}^3$

$$ {}^{link}\mathbf{T}_{f_i} = \begin{bmatrix} {}^{link}\mathbf{R}_{f_i} & {}^{link}\mathbf{r}_{f_i} \\ 0 \in \mathbb{R}^{1\times 3} & 1 \end{bmatrix} \in \mathbb{R}^4 \tag{3.15} $$

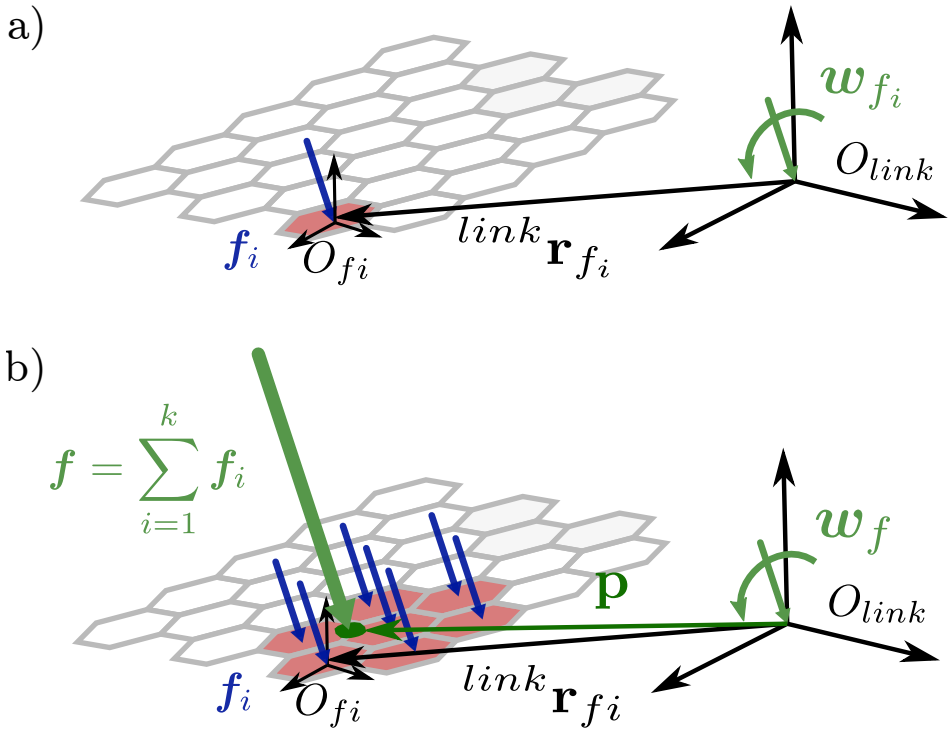

Figure 8 Computation of the interaction wrench from tactile information. a) the contact force $\boldsymbol{f}_i$ produces a wrench $\boldsymbol{w}_{f_i}$ at the link coordinate frame O_{link}. b) a group of k contact points produce a resultant wrench $\boldsymbol{w}_f$.

3.2.2. Interaction wrench from tactile information

Once the kinematic parameters of the taxels on the robot's link are defined, let us analyze how the interaction forces propagate through the kinematic chain. The contact force $\boldsymbol{f}_i$ measured by the i-th taxel is expressed at the contact reference frame O_{f_i}. However, it produces a wrench $\boldsymbol{w}_{f_i} \in \mathbb{R}^6$ at the link frame O_{link} propagated by the lever $^{link}\mathbf{r}_{f_i}$ as shown in Fig. 8-a. The interaction wrench of one taxel is then calculated as

$$\boldsymbol{w}_{f_i} = \begin{bmatrix} {}^{link}\mathbf{R}_{f_i}\boldsymbol{f}_i \\ {}^{link}\mathbf{r}_{f_i} \times {}^{link}\mathbf{R}_{f_i}\boldsymbol{f}_i \end{bmatrix} \tag{3.16}$$

For interactions over larger areas, i.e. covering more than one taxel, we can add the contributions of each taxel to compute a resultant wrench at the link frame O_{link}. Therefore, a patch of k taxels produces the resultant wrench $\boldsymbol{w}_f \in \mathbb{R}^6$ as illustrated in Fig. 8-b.

$$\boldsymbol{w}_f = \begin{bmatrix} \boldsymbol{f}_f \\ \boldsymbol{\eta}_f \end{bmatrix} = \sum_{i=1}^{k} \boldsymbol{w}_{f_i} \tag{3.17}$$

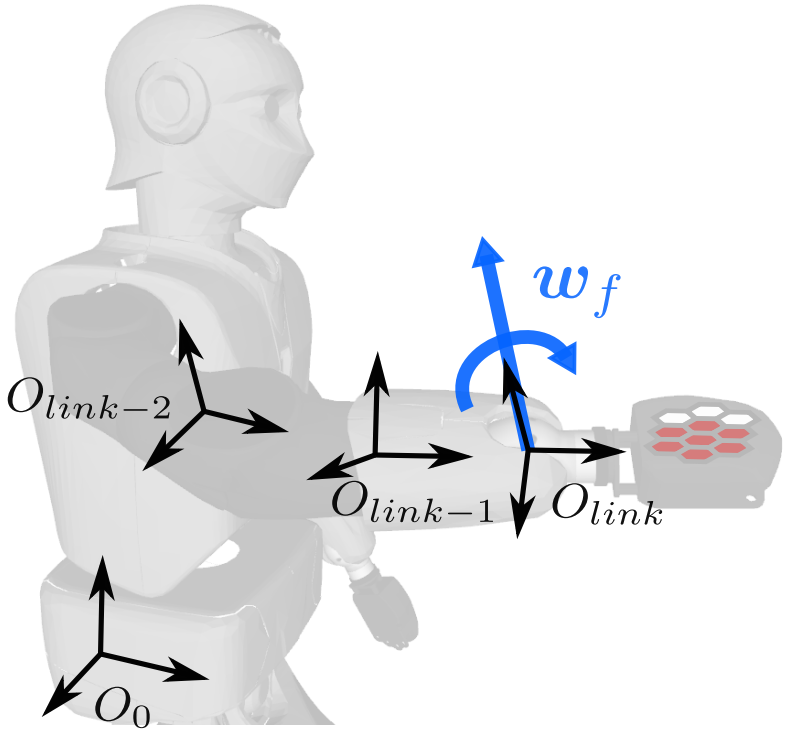

Figure 9 Kinematic chain of the robot from the base link frame O_0 to the patch mounting link frame O_{link}.

Where $\boldsymbol{w}_f$ is equal to the wrench produced by the sum of all the forces in the k taxels applied to the CoP of the contact as shown in Fig. 8, and is composed by the interaction force $\boldsymbol{f}_f \in \mathbb{R}^3$ and the twisting moment $\boldsymbol{\eta}_f \in \mathbb{R}^3$. In these three vectors, the subscript $_f$ means that its source is the direct force measurement from the taxel. This identifier will help distinguish the force measurements from other sensing modalities in the taxel, this is given in the later sections of this chapter.

In practice, a link of the robot can have more than one patch mounted simultaneously. However, the calculation of $\boldsymbol{w}_f$ is still valid because the kinematic parameters of the formulation are considered fixed and thus, the iteration over the taxels can be extended to all the k taxels of all the l patches on the same link as

$$\boldsymbol{w}_f = \sum_{j=1}^{l} \sum_{i=1}^{k} \boldsymbol{w}_{f_{j,i}} \tag{3.18}$$

where $\boldsymbol{w}_{f_{j,i}}$ is an extended representation of Eq. (3.17) with a subscript j to denote the j-th patch in the link. This formulation is equivalent as having a virtual force-torque sensor mounted at O_{link}, however we can freely chose the reference point to calculate the resultant wrench, and make distinctions from the geometric information that the robot skin provides as will be shown in Section 3.2.5.

3.2.3. Direct physical interaction task formulation

To use the resultant wrench $\boldsymbol{w}_f$ with the task formulation Eq. (3.4), we must now consider the whole kinematic chain of the robot from the base link to the patches mounting link. This requires the forward kinematics of the robot to be known. Let us define a coordinate frame for every link of a robot from the link where the skin is mounted O_{link} to the root or base link O_0 as shown in Fig. 9. From the forward kinematics of the robot, we can calculate the transformation to go from O_{link} to O_0, from the transformations between each frame in the kinematic chain as

$$ {}^{0}\mathbf{T}_{link} = {}^{0}\mathbf{T}_{1}\ {}^{1}\mathbf{T}_{2} \ldots {}^{link-2}\mathbf{T}_{link-1}\ {}^{link-1}\mathbf{T}_{link} \tag{3.19} $$

${}^{0}\mathbf{T}_{link}$ is composed by the rotation ${}^{0}\mathbf{R}_{link} \in SO(3)$ and the translation ${}^{0}\mathbf{r}_{link} \in \mathbb{R}^3$. With this information, we can finally define an operational task for direct interactions as

$$ \boldsymbol{\tau}_f = {}^{0}\mathbf{J}_{link}(q)^{\top}\ {}^{0}\mathbf{E}_{link}\boldsymbol{w}_f \tag{3.20} $$

where $\boldsymbol{\tau}_f \in \mathbb{R}^n$ is the joint torque vector, ${}^{0}\mathbf{J}_{link} \in \mathbb{R}^{6\times n}$ is the geometric Jacobian mapping joint velocities $\dot{\boldsymbol{q}}$ onto Cartesian velocities of O_{link} with respect to O_0, and ${}^{0}\mathbf{E}_{link}$ is the composite 6D rotation matrix

$$ {}^{0}\mathbf{E}_{link} = \begin{bmatrix} {}^{0}\mathbf{R}_{link} & 0 \in \mathbb{R}^{3\times 3} \\ 0 \in \mathbb{R}^{3\times 3} & {}^{0}\mathbf{R}_{link} \end{bmatrix} \tag{3.21} $$

This task formulation can be applied to any link of a robot covered with taxels to generate a compliant reaction to touch. The reaction torque is proportional to the contact forces applied to the robot's link. Therefore, it can be combined with other tasks with fusion methods as with the weighted sum Eq. (3.6) or the null-space projectors Eq. (3.10). If multiple contacts are applied to different skin patches on the robot's body, they can be accounted in the same way. Then, for a set of k contacts, the composite compliance torque is computed by

$$ \boldsymbol{\tau}_f = \begin{bmatrix} {}^{0}\mathbf{J}_1(\boldsymbol{q}) \\ {}^{0}\mathbf{J}_2(\boldsymbol{q}) \\ \vdots \\ {}^{0}\mathbf{J}_k(\boldsymbol{q}) \end{bmatrix}^{\top} \begin{bmatrix} \boldsymbol{w}_{f_1} \\ \boldsymbol{w}_{f_2} \\ \vdots \\ \boldsymbol{w}_{f_k} \end{bmatrix} \tag{3.22} $$

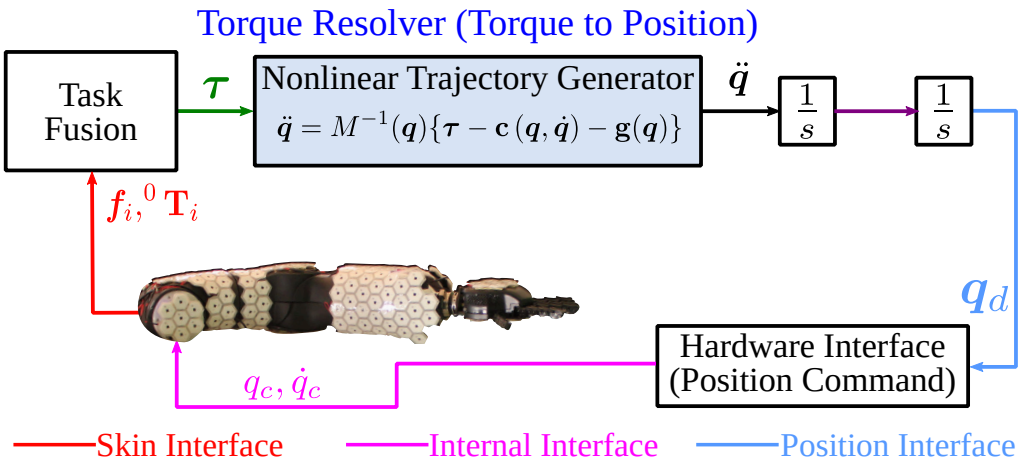

Figure 10 Although the proposed controller works at torque-effort level, it can be fed into a torque resolver to generate smooth trajectories for position or velocity commanded interfaces as shown in [4, 5].

3.2.3.1 Experiment: Direct physical interactions

The formulation for direct physical interaction was applied in the H1 robot in [4]. The interaction task was implemented to use the information provided by the large area skin system developed by [1, 5]. In [4], ten instances of the interaction task Eq. (3.20) were combined with a standing balance task to generate an active compliant behavior on the upper body.

The compliance controller outputs a joint-torque vector. However, a torque resolver as [4, 5] enables its implementation for position or velocity commanded robots (see Fig. 10). In this case, the torque resolver module computes dynamically consistent smooth trajectories for the joints, imposing desired dynamics to the robot.

The simultaneous interaction tasks were: left upper arm, left lower arm, left-hand palm, left hand back, right upper arm, right lower arm, right-hand palm, right hand back, torso, and hip. These instances were combined in a single task as Eq. (3.22) and combined with a balance task (the balance task implementation will be elaborated in Chapter 4) and a self-collision avoidance task with the following strict hierarchy.

1. Balance / supporting task.
2. Self collision avoidance task.
3. Skin interaction task + body posture task.

Fig. 11 shows two results of the implementation. Fig. 11-a shows the robot under multiple simultaneous contacts behaving compliantly to the interaction forces. Fig. 11-b shows a large area interaction on the arms and the torso in a *hug* interaction. In these experiments, the dimension of the interaction task increases with the number of instances of Eq. (3.20). If we traverse all the taxels all the time considering the task to be full rank all the time, computing the null-space projector to execute a lower priority task becomes unfeasible. This is the reason

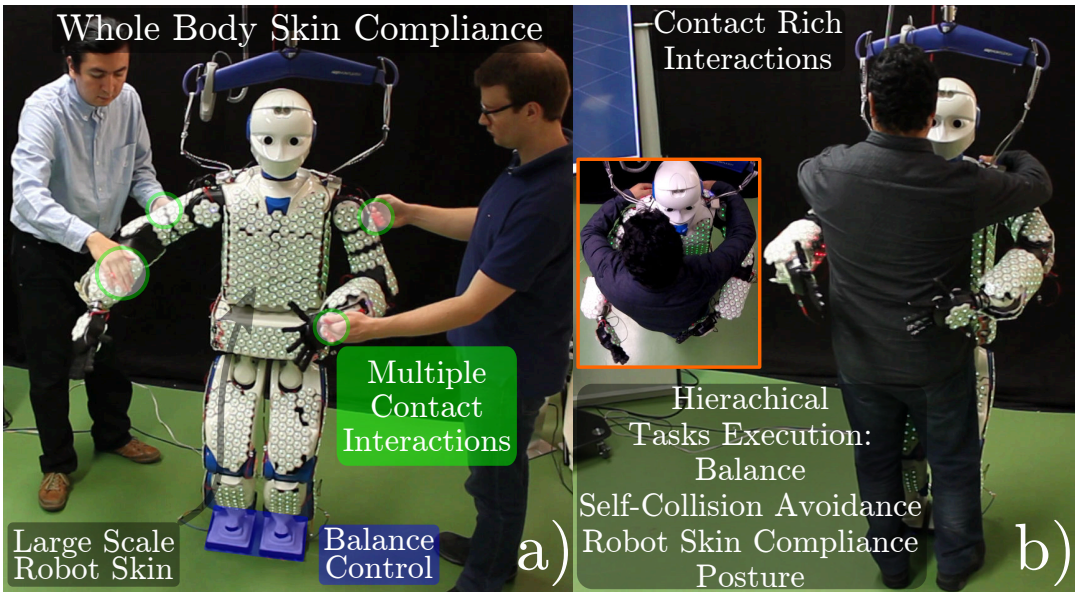

Figure 11 Direct interaction task implemented in a full-size humanoid robot in [4, 5]. a) Multiple simultaneous contacts are supported. b) Large area interactions are supported in safe human-robot physical interaction.

why the whole-body interaction task has the lowest priority as the body posture task in these experiments. To increase the versatility of this approach, we must enhance the formulations to reduce the computational load.

3.2.4. Efficient computation for multiple interaction tasks over large areas

The number of implicit calculations in Eq. (3.18) increases with the number of taxels mounted on the same link. Therefore, traversing all the taxels of a large link (e.g. the torso of a humanoid robot) can be computationally expensive and thus not real-time safe. Therefore, an active taxel calculation policy should be considered to avoid unnecessary calculations when the interaction force detected is neglectable. Let us then define an interaction threshold ϵ_f such that Eq. (3.32) is redefined as

$$\boldsymbol{w}_{f_i} = \begin{cases} 0 \in \mathbb{R}^6 & ||\boldsymbol{f}_i|| < \epsilon_f \\ \begin{bmatrix} {}^{link}\mathbf{R}_{f_i}\boldsymbol{f}_i \\ {}^{link}\mathbf{r}_{f_i} \times {}^{link}\mathbf{R}_{f_i}\boldsymbol{f}_i \end{bmatrix} & \epsilon_f \leq ||\boldsymbol{f}_i|| \end{cases} \tag{3.23}$$

Furthermore, a similar approach can help reduce the number of operation when handling several tasks over different links of the robot by avoiding computing the Jacobian matrices of the links where the interaction is neglectable. Then, we can rewrite Eq. (3.20) as

$$\boldsymbol{\tau}_f = \begin{cases} 0 \in \mathbb{R}^n & ||\boldsymbol{w}_f|| = 0 \\ {}^0\mathbf{J}_{link}(q)^\top \, {}^0\mathbf{E}_{link}\boldsymbol{w}_f & ||\boldsymbol{w}_f|| \neq 0 \end{cases} \tag{3.24}$$

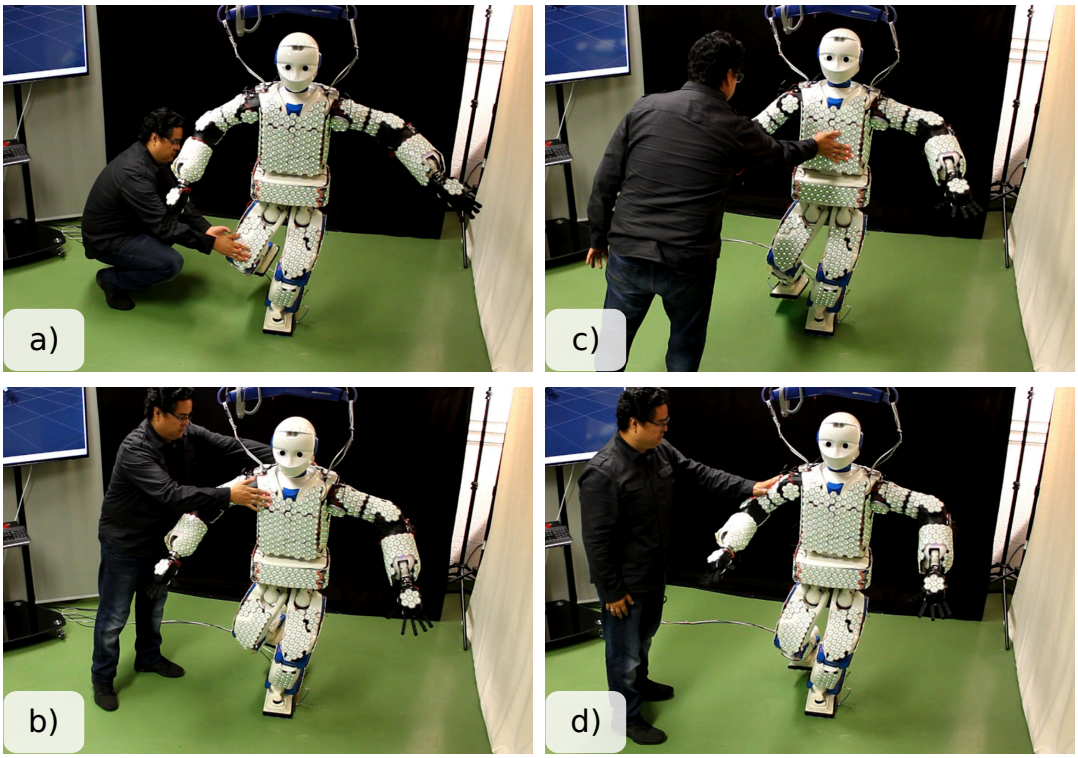

Figure 12 Implementation of whole body interaction task with efficient computation. The skin compliance is executed with a higher priority than a whole body Center of Mass position task. The CoM position task is executed in the null-space of the active instances of the tactile interaction task. And these two are executed in the null-space of a self collision avoidance task and a supporting/balance constraint task.

If the interaction task is applied in a strict hierarchical fusion as Eq. (3.10), the null space projector of the instances with no force detected can be directly assigned as the identity matrix $\mathbf{I} \in \mathbb{R}^{n \times n}$ which will avoid computing the generalized inverse of an $m \times n$ matrix and three large size matrix multiplications.

3.2.4.1 Experiment: Efficient computation of multiple interaction tasks

We tested this formulation in a similar experiment to the one in Section 3.2.3.1 but applying the methods of Section 3.2.4 to reduce the computations. With these efficient computation methods, we can increase the priority of the tactile interaction task in the hierarchy. Therefore, we moved the posture task one level down and replaced it with a full-rank Center of Mass position control task formulated as

$$\boldsymbol{\tau}_{com} =^{0} \mathbf{J}_{com}(q)^{\top} \mathbf{K}_{com} \boldsymbol{e}_{com} \tag{3.25}$$

where ${}^{0}\mathbf{J}_{com}(q) \in \mathbb{R}^{3 \times n}$ is the Center of Mass Jacobian matrix as proposed by Sugihara and Nakamura in [136], $\mathbf{K}_{com} \in \mathbb{R}^{3 \times 3}$ is a proportional gain, and $\boldsymbol{e}_{com}$ is the CoM position error defined as $\boldsymbol{e}_{com} = \boldsymbol{x}_{com}\,[0, 0, 0.8]^{\top}$ (a constant height over the supporting foot).

Additionally, we increase the number of instances of the interaction task to one of the legs. Therefore, the interaction task instances were 13: left upper arm, left lower arm, left-hand palm, left hand back, right upper arm, right lower arm, right-hand palm, right hand back, torso, hip, right upper leg, right lower leg, and right foot sole. The strict task hierarchy in this experiment is:

1. Balance / supporting task.
2. Self collision avoidance task.
3. Skin interaction task.
4. Center of mass position task

Fig. 12 shows different interactions with the robot. The CoM position task compensates with the free limbs the deviations that the interactions produce in the regulation of the CoM position. The support balancing task (dimension 6) with the highest priority, in this case, uses only the left leg. In the null-space of the support task, a self-collision avoidance task similar to [137] is keeping the hands, elbows, foot, and knee away from each other and the torso and supporting leg by generating repulsive fields. This task is also active only when the monitored distances are critically small and bypassed when there is no risk of collision. In the null-space of this task, the 13 instances of the tactile interaction task are executed also with a dynamically changing dimension. Finally, in the null-space of all these tasks, the CoM position task is continuously acting on all the remaining DoF of the robot. The behavior imposed in the robot by these tasks shows a robust balance on the support foot while the body posture can be modeled by multiple simultaneous contacts.

3.2.5. Physical interactions using additional information / Pressure driven body compliance

The interaction task in Eq. (3.16) - (3.20) is formulated using link-wise resultant wrenches to generate the joint reaction torques. It is equivalent to having force-torque sensors mounted in the reference frames of the robot links (similar to the KUKA LWR [32]). However, tactile sensors provide additional information from two main factors: 1) the spatial distribution of the sensors over the body of the robot, and 2) additional sensing modalities as will be extended in Section 3.3. Let us develop one clear example of a modality for body compliance that exploits the spatial distribution of tactile sensors and cannot be reproduced using only joint torque sensors.

The resultant link wrench in Eq. (3.17) is produced from direct force measurements in the contact points as shown in Fig. 8. However, the area and geometry of the taxels are known as drawn in Fig. 1. Therefore if we collect these details while building the interaction wrench, we can approximate the geometry of the contact area as drawn in Fig. 13.

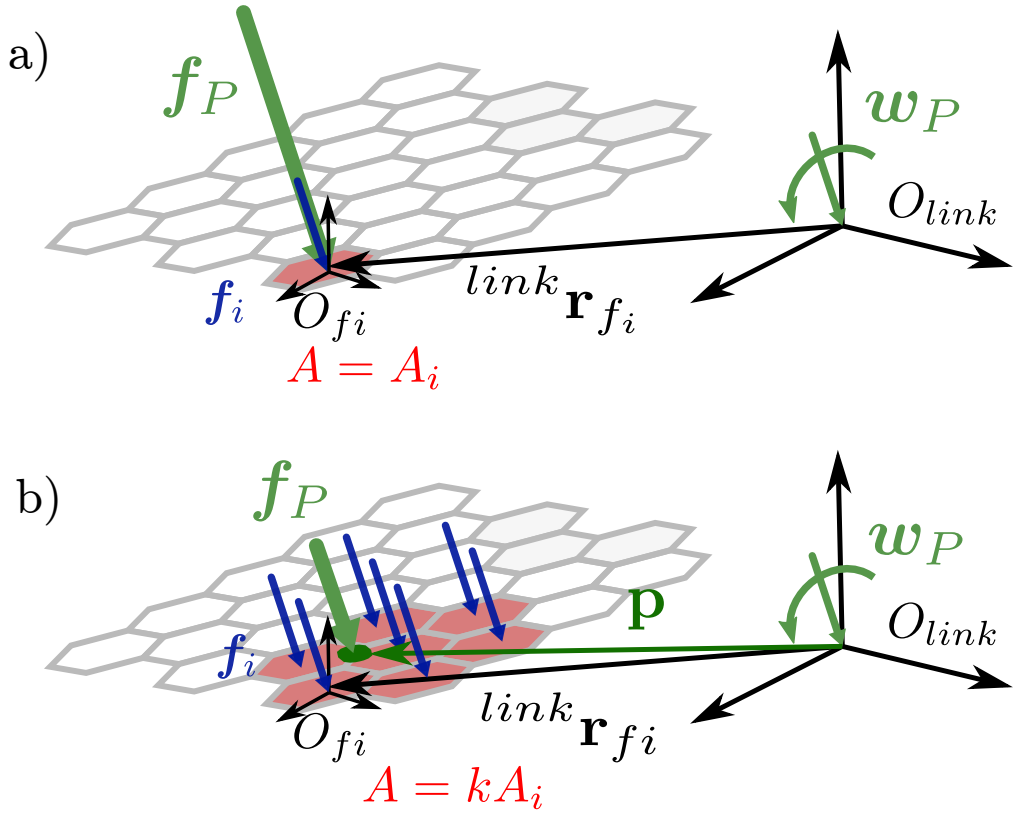

Figure 13 Pressure driven interaction task. a) interaction force is amplified when the contact area is small. b) interaction force is damped when the contact area is larger.

Let us now formulate an interaction wrench that uses the area to amplify or damp the interaction force. In a group of k taxels, the taxel coordinate frame of the i-th taxel is defined as O_i. In O_i, the force measured by the i-th taxel of area A_i is defined as $\boldsymbol{f}_i \in \mathbb{R}^3$. If the taxel only provide the magnitude of the normal force $f_n \in \mathbb{R}$, the contact force can be constructed as $\boldsymbol{f}_i = [0, 0, f_i]^\top$. Using a minimum contact force threshold ϵ_a while iterating over the taxels as in Eq. (3.23), the area $\alpha_i \in \mathbb{R}$ of every contact point is

$$\alpha_i = \begin{cases} A_i & ||\boldsymbol{f}_i|| \geq \epsilon_a \\ 0 & ||\boldsymbol{f}_i|| < \epsilon_a \end{cases} \tag{3.26}$$

Then, with this information, we can define a pressure driven interaction wrench $\boldsymbol{w}_P \in \mathbb{R}^6$ by scaling the interaction wrench $\boldsymbol{w}_f$ with a gain ξ with units of area, e.g. $[m^2]$, to adjust the sensitivity of the compliant controller, and to match the units for the subsequent computations as

$$\boldsymbol{w}_P = \begin{bmatrix} \boldsymbol{f}_P \\ \boldsymbol{\eta}_P \end{bmatrix} = \frac{\xi}{\sum \alpha_i} \boldsymbol{w}_f \tag{3.27}$$

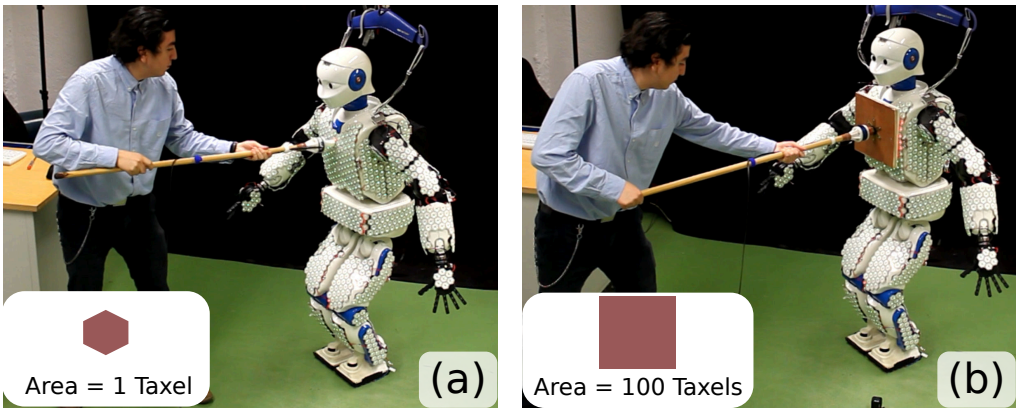

Figure 14 Whole-body pressure-driven compliance controller. External forces were applied on the robot using probes mounted on an force-torque sensor. a) The first probe concentrates all the applied force in a single taxel area. b)The second probe distributes the force on a large area.

where $\boldsymbol{w}_P$ is an amplified wrench depending on both the contact force and area, which will be used to implement the pressure-driven body compliance modality. $\boldsymbol{f}_P$ and $\boldsymbol{\eta}_P$ are the amplified force and torque, respectively.

After computing the virtual wrench Eq. (3.27), we can propagate it through the kinematic chain with the transposed Jacobian matrix using the task formulation. Therefore, knowing the kinematic parameters of the robot and the transformations from the contact point to the base link O_0, the torques for the joints of the kinematic chain can be computed as

$$\boldsymbol{\tau}_P = {}^0\,\mathbf{J}_{link}(q)^\top\, {}^0\mathbf{E}_{link}\boldsymbol{w}_P \tag{3.28}$$

where $\boldsymbol{\tau}_P \in \mathbb{R}^n$ is the joint torque vector, and ${}^0\mathbf{J}_{link} \in \mathbb{R}^{6\times n}$ is the geometric Jacobian mapping joint velocities $\dot{\boldsymbol{q}}$ onto Cartesian velocities of O_{link} with respect to O_0. $\boldsymbol{\tau}_P$ represents the joint-torques generated by the amplified force to produce a pressure-based compliant reactive behavior in the robot.

3.2.5.1 Experiment: Pressure-driven body compliance

We evaluated the performance of the pressure-driven compliance controller in the H1 robot as in the experiments[1] in Sections 3.2.3.1, and 3.2.4.1.

To highlight the difference between the reaction in a distributed contact force and a concentrated force, two scenarios were prepared. The task priority arrangement is as follows:

[1] This result and the formulation of the pressure-driven body compliance was published in the peer reviewed journal article [57] and presented in the 2019 IEEE/RSJ International Conference on Intelligent Robots and Systems (IROS 2019).

1. Balance / supporting task.

2. Pressure-driven compliance task.

3. Posture task.

The robot must keep the balance all the time while reacting to the contact pressure with the whole upper-body. The posture task holds the lowest priority to provide postural stability to the remaining DoF after the execution of the first two tasks. Two probes were used to apply force on different parts of the upper body (see Fig. 14).

The probes were mounted on a force-torque sensor to measure the applied external force. The robot reacts considerably faster when the force is concentrated in a small area. Therefore, small forces can move large body parts like the torso when applied on a single taxel (see Fig. 14-a). The behavior is kept also with multiple simultaneous contacts (see Fig. 14-b). Conversely, the robot can hold large forces when they are distributed in a wide area (see Fig. 14-b). Under low contact pressure, the robot holds the body posture strongly and the pushing force is transferred to the floating base and thus handled by the balance controller.

The interaction forces, torques and joint velocities are plotted in Fig. 15. During the first 50 seconds of the experiment, the probe with a single taxel area Fig. 14-a was used. Then, during the following time the probe with a large area Fig. 14-b was used. The plots show that with the single-taxel probe, the external force $||\boldsymbol{f}_{ext}||$ is small but the virtual force $||\boldsymbol{f}_P||$ is large (see plot *a* in Fig. 15), producing highly reactive motions (see plots *b* and *c* in Fig. 15). And with the wide area probe, the external force reaches high levels but causes almost no motion on the robot.

3.3. Formulation of Virtual Interaction Tasks

The interaction task formulation of the previous section is a straightforward method to close the loop in controlled physical interactions of a robot with the environment. It uses direct force measurements at the contact points to produce reaction joint torques that minimize the contact force. However, spatially distributed additional modalities can be exploited to produce a similar compliant behavior by using the artificial potential field approach [138].

In [58], Khatib proposes a method for obstacle avoidance by monitoring the distance between significant points located in the kinematic chain of a robot and known geometry obstacles in the environment. The potential field approach proposes then a virtual repellent force inversely proportional to the distance between the robot geometry and the environment. However, this approach required complete knowledge of the environment geometry, and complicated potential field formulations. Later, direct distance measurement was available due to new sensing technologies that allowed mounting several range finder sensors on a robot for collision avoidance as in [49], and [50]. Range finder sensors can also be included in taxel hardware

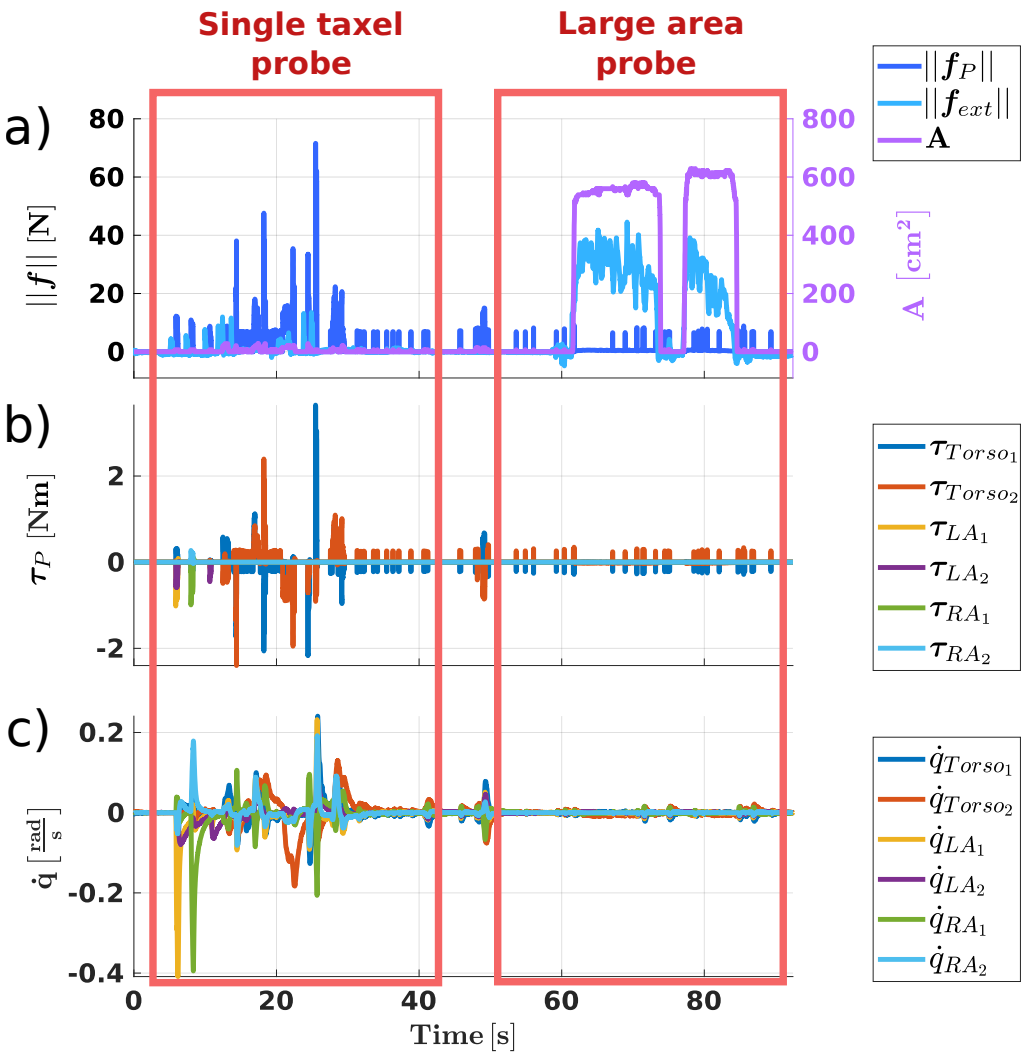

Figure 15 Reaction forces, torques and velocities during the experiment. During the first 50 seconds of the experiment, the single taxel area probe was used. After that, the large area probe was mounted on the sensor. a) shows the interaction forces, $||\boldsymbol{f}_P||$ is the norm of the virtual force, $||\boldsymbol{f}_{ext}||$ is the applied force measured by the force-torque sensor in the probe, and A is the contact area. b) shows some representative joint-torques generated by the pressure-driven compliance controller, $\boldsymbol{\tau}_{Torso_1}$, $\boldsymbol{\tau}_{LA_1}$ and $\boldsymbol{\tau}_{RA_1}$ are the torque of the first joint of the torso, the left arm and the right arm respectively. c) shows the joint velocities generated by the reaction motions.

which can help implement the potential field approach from direct distance measurements. However, the formulation can be easily adapted to other sensing modalities that do not imply physical force interactions.

Let us explore the potential of the potential fields approach by formulating virtual interaction tasks that produce body reaction motions to different sensing modalities on robots with large numbers of sensing points distributed over the robot's body.

3.3.1. Virtual interactions from distributed proximity sensors

Following a standard potential field obstacle avoidance scheme [58]. Every object in the environment, including all the robot's links, is considered to have a repulsive field normal to the object's surface. Such field used to be described by a vector field defined by the geometry of the object. In this form, when an object approaches a robot's link, a reactive force inversely

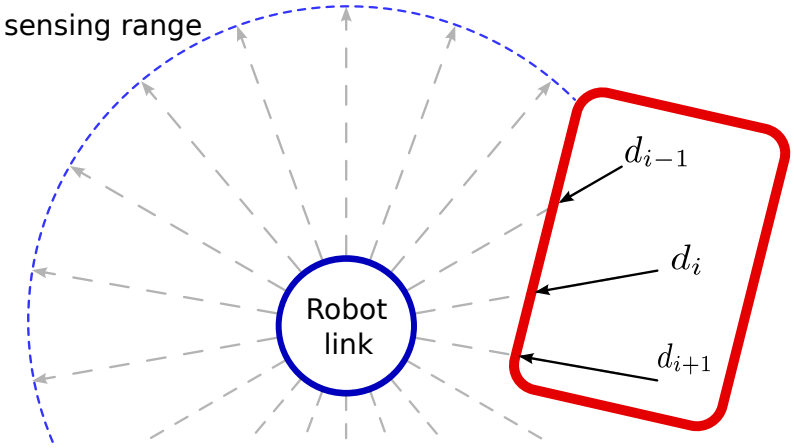

Figure 16 Direct measurement of repulsive field from distribute proximity sensors.

proportional to the distance between the bodies is applied to keep the robot's body away from it. The reactive force can be transformed into a joint torque vector as

$$\boldsymbol{\tau}_p = {}^0\,\mathbf{J}_p\left(\boldsymbol{q}\right)^\top \boldsymbol{f}_p\left(d\right) \tag{3.29}$$

where $\boldsymbol{\tau}_p \in \mathbb{R}^n$ is the induced joint torque, $\boldsymbol{f}_p \in \mathbb{R}^m$ is the virtually induced force in task coordinates being m the dimension of the task space, $d \in \mathbb{R}$ is the distance between the surfaces of the link and the object, and $\mathbf{J}_p\left(\boldsymbol{q}\right) \in \mathbb{R}^{m\times n}$ is the Jacobian matrix which defines the differential kinematic mapping between the task space and the joint space for the surface point where the distance is measured on the robot.

All the geometrical calculations regarding the potential fields around the objects can be avoided by directly measuring the distance from a link's surface to any surrounding object as shown in Fig. 16. This measurement is possible thanks to the inclusion of a range finder array as in [139]. In addition, because of nowadays electronics are smaller, advanced skin implementations have higher spatial resolution and thus, the distances between the taxels are shorter.

Most small size range finder sensors in the market deliver an inverse measurement that saturates with the closest detectable distance and returns 0 when the target is outside the sensing range. With this behavior, a repulsive force can be calculated defining a sensing range as shown in Fig. 16.

$$\boldsymbol{f}_{p_i} = k_{prox}\left(d_{range} - d_i\right)\boldsymbol{u}_{p_i} \tag{3.30}$$

where d_i is the measured distance by the i-th taxel of the array, and $k_{prox} \in \mathbb{R}$ is a defined repulsion gain. The subscript p now denotes the origin of the feedback from *proximity* to the environment. $\boldsymbol{u}_{p_i} \in \mathbb{R}^3$ is a unit vector that describes the sensing direction of the proximity sensor. If the proximity sensor is oriented ortogonal to the taxel geometry, it is defined as $\boldsymbol{u}_{p_i} = [0\ 0\ 1]^\top$ which is the best configuration for collision avoidance because it produces the

strongest repulsive filed from the environment.

The similarity to the interaction force $\boldsymbol{f}_f$ is obvious and thus, the formulation of the operational task from the proximity sensing is straightforward. Therefore, for a set of k taxels mounted on a link, the contributions of the repulsive forces produce a resultant wrench at the link frame O_{link}

$$\boldsymbol{w}_p = \sum_{i=1}^{k} \boldsymbol{w}_{p_i} \tag{3.31}$$

where

$$\boldsymbol{w}_{p_i} = \begin{bmatrix} {}^{link}\mathbf{R}_{p_i} \boldsymbol{f}_{p_i} \\ {}^{link}\mathbf{r}_{p_i} \times {}^{link}\mathbf{R}_{p_i} \boldsymbol{f}_{p_i} \end{bmatrix} \tag{3.32}$$

Despite its similarity to Eq. (3.18), $\boldsymbol{w}_p$ represents a virtual wrench that does not imply physical contact with the environment. This is important when designing controllers for floating base systems, where physical contacts with the environment modify the momentum of the system, increase the supporting constraints, and produce variations in the floating base state. On the other hand, virtual interactions only modify the momentum of the system but do not impose hard constraints on the system. For fixed-base robots, both types of interactions (virtual and direct) can be treated identically. Once the difference is highlighted, we can define the virtual interaction task generated from proximity sensing as

$$\boldsymbol{\tau}_p = {}^0\mathbf{J}_{link}(\boldsymbol{q})^\top \, {}^0\mathbf{E}_{link} \boldsymbol{w}_p \tag{3.33}$$

Additionally, the methods to reduce the number of operations applied in the previous section can also be applied for virtual interactions. For the case of proximity sensors, the threshold is automatically defined by the range of the sensors. Then, when an obstacle is far from the sensing point, the sensor will return $d_i = d_{range}$, and the virtual interaction wrench $\boldsymbol{w}_p = 0 \in \mathbb{R}^6$.

3.3.1.1 Experiment: Virtual interaction with proximity sensors

We evaluated the performance of the proximity-driven compliance task in the H1 robot as in the experiments in Sections 3.2.3.1, and 3.2.4.1. The proximity-based virtual interaction task was combined with the direct physical interaction task described in Section 3.2.3. The task priority layout is:

1. Balance / supporting task.
2. Self collision avoidance task.
3. Skin interaction task + proximity task.

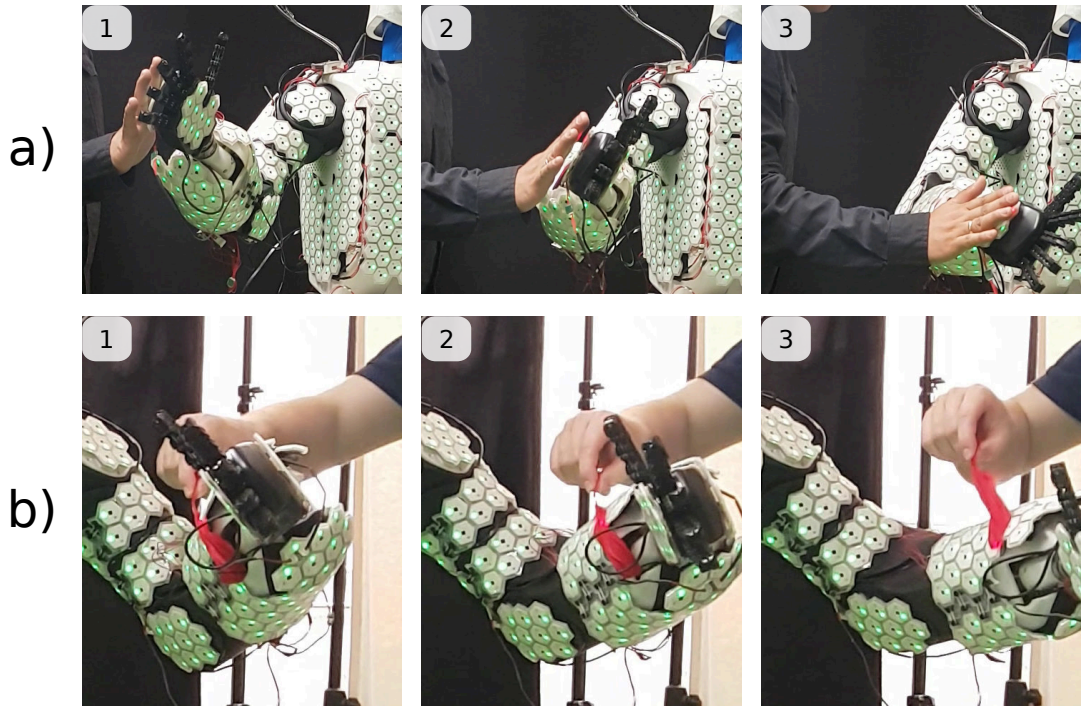

Figure 17 Experimental evaluation of the proximity virtual interaction task. a) The hand of the robot is repelled by the hand without touching it. b) This modality of body compliance enables the compliant behavior with a relatively mass-less object such as a feather.

Fig. 17 shows two sequences from the virtual interaction. In Fig. 17-a the robot's right hand is repelled by a human hand without physical contact involved. The proximity sensors detect the human hand and the task produces the reactive repelling force in the surface of the robot hand. The sensing range of the sensors was adjusted to 2 cm. The sequence in Fig. 17-b shows a feather manipulating the robot hand with virtual contact. The proximity interaction task enables this kind of virtual interaction with weightless objects.

3.3.2. Virtual interactions from distributed temperature sensors

The potential field approach for collision avoidance described before maximizes the distances between the robot and the environment to prevent collisions and unexpected contacts while performing other operational tasks. The proximity task Eq. (3.33) implements it with direct sensor feedback thanks to complementary sensing modalities included in the taxels of a robot skin. However, the direct sensor input can come from other sensing modalities than proximity, for example, temperature.

Human skin also senses temperature and our reactive motions when we detect a drastic increment in the temperature of our hand in the vicinity of a hot object is to automatically increase the distance (i.e. retraction reflex of the arm). This natural reflex helps preserve the integrity of our body and is feasible thanks to the temperature sensing modality of our skin. Similarly, for robot skin systems with temperature sensing, we can define a repulsive field and thus a virtual interaction task proportional to the measured temperature.

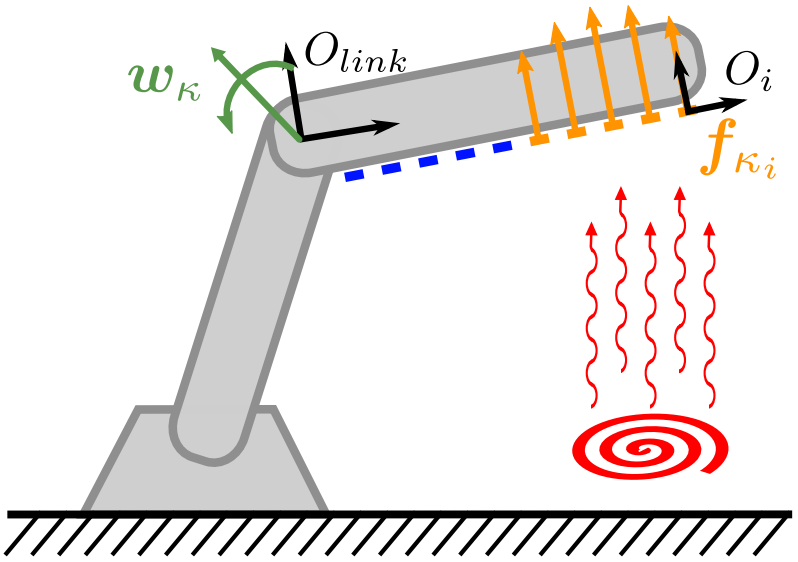

Figure 18 Temperature driven repulsive field. When the temperature detected at the i-th taxel is higher than κ_0, a repulsive potential $\boldsymbol{\kappa}_i \in \mathbb{R}^3$ is generated to push the robot away from the source of temperature.

Most commercial temperature sensors return a value from 0 to saturation within a specific temperature range. Within this range, we can define a threshold $\kappa_0 \in \mathbb{R}$ to generate a virtual repulsive force κ_i for the i-th taxel as

$$\kappa_i = \begin{cases} 0 \in \mathbb{R}^n & T_{measured} < \kappa_0 \\ T_{measured} - \kappa_0 & T_{measured} \geq \kappa_0 \end{cases} \tag{3.34}$$

where $T_{measured}$ is temperature measured by the sensor and $\kappa_i \in \mathbb{R}$ the magnitude of the repulsive force at the sensing point. We can then define a repulsive force vector at the taxel frame O_i as can be seen in Fig. 18

$$\boldsymbol{f}_{\kappa_i} = \begin{bmatrix} 0 \\ 0 \\ \kappa_i \end{bmatrix} \tag{3.35}$$

Similarly to the other sensing modalities, the virtual force produces a virtual interaction wrench at the link coordinate frame O_{link}.

$$\boldsymbol{w}_{\kappa_i} = \begin{bmatrix} {}^{link}\mathbf{R}_i \boldsymbol{f}_{\kappa_i} \\ {}^{link}\mathbf{r}_i \times {}^{link}\mathbf{R}_i \boldsymbol{f}_{\kappa_i} \end{bmatrix} \tag{3.36}$$

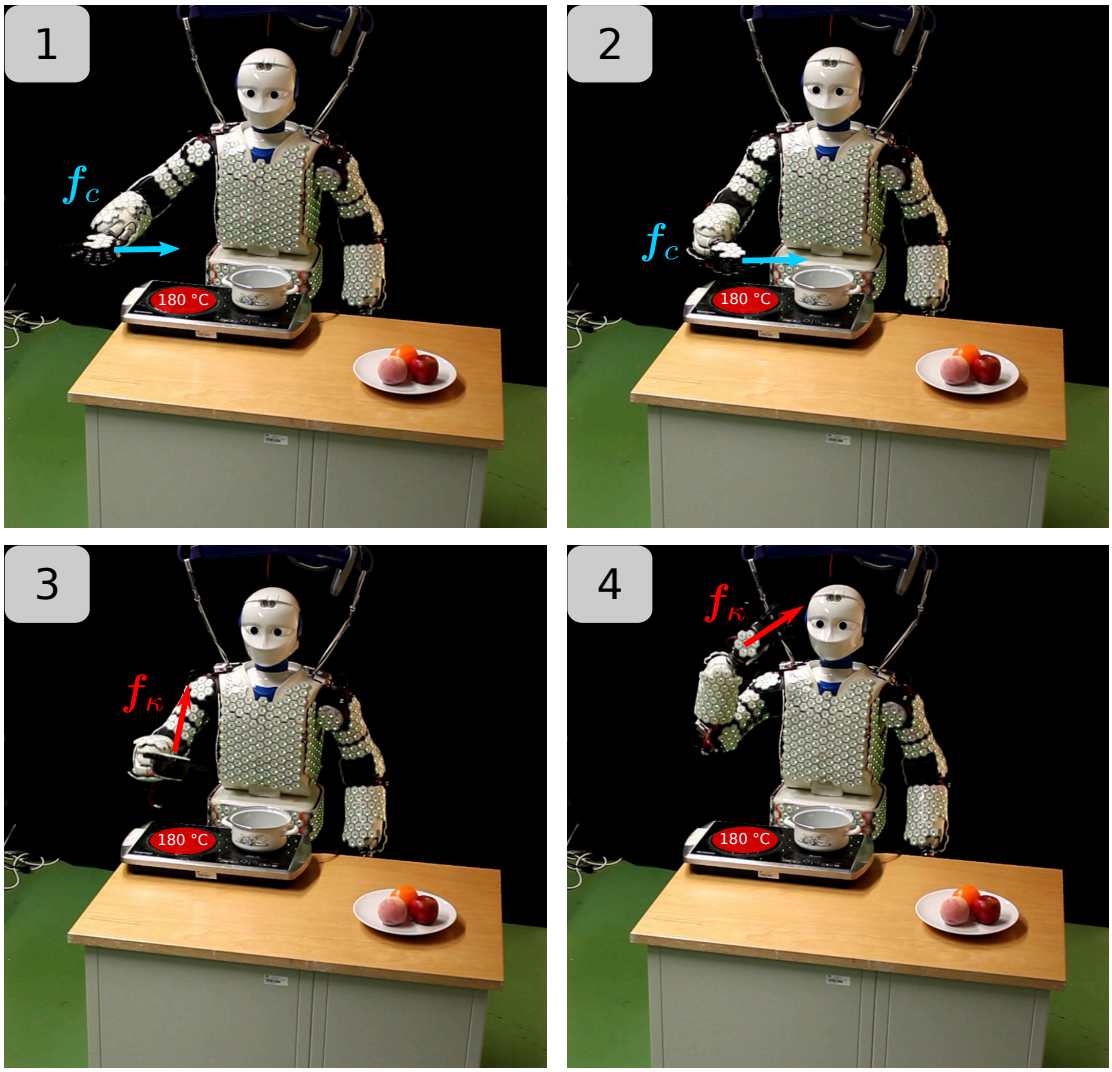

Figure 19 Cooking simulation experiment. The robot operates an electric stove with a burner on at ≈ 180 °C. When the hand of the robot passes by the burner, the taxels on the hand back detect the increment in the temperature and activate the temperature compliant task which has higher priority than the hand Cartesian control task. As a result, the hand Cartesian task is blocked by the retraction motion of the temperature compliance task.

Then, for a set of k taxels, the resultant interaction wrench is

$$\boldsymbol{w}_\kappa = \sum_{i=1}^{k} \boldsymbol{w}_{\kappa_i} \tag{3.37}$$

and the interaction task from temperature sensing is defined as

$$\boldsymbol{\tau}_\kappa = {}^0\,\mathbf{J}_{link}(\boldsymbol{q})^\top\, {}^0\mathbf{E}_{link}\boldsymbol{w}_\kappa \tag{3.38}$$

Once again, the formulations for efficient computation are valid to reduce the computational load of this virtual interaction task.

3.3.2.1 Experiment: Virtual interaction with temperature sensors

We evaluated the performance of the temperature-driven interaction task in the H1 robot introduced in Section 2.3.2. The experiment emulates a cooking scenario where the robot operates in front of an electric stove with a burner *on*, as shown in Fig. 19. The temperature at the burner plate is $\approx$ 180 °C. For this experiment, a Cartesian Position and Orientation task is included in the Hierarchy below the temperature compliance task. This decision is motivated by the priority of human reactions to burning temperature contacts as several studies have shown in the past century [140]. Our nerve system prioritizes the reaction to a harmful stimulus over a purpose task to prevent damage [141]. As a result, pain reflexes always preempt manipulation tasks [142]. Thus, the task layout in this experiment is:

1. Balance / supporting task.
2. Temperature-driven compliance task.
3. Right hand Cartesian position and orientation task.
4. Posture task.

The Cartesian position and orientation task is defined using the operational space formulation using Quaternion representation proposed by Yuan in [143]. The task is formulated with a damped attractor field as

$$\boldsymbol{\tau}_h = {}^0\,\mathbf{J}_{link}\left(\boldsymbol{q}\right)^T \begin{bmatrix} -\dot{\boldsymbol{x}}_h + \mathbf{K}_{h_p}\boldsymbol{e}_{h_p} \\ \\ -\boldsymbol{\omega}_h + \mathbf{K}_{h_o}\boldsymbol{e}_{h_o} \end{bmatrix} \tag{3.39}$$

where $\dot{\boldsymbol{x}}_h \in \mathbb{R}^3$ us the Cartesian velocity of the hand, $\boldsymbol{\omega}_h \in \mathbb{R}^3$ is the angular velocity of the hand, both with respect to O_0. $\mathbf{K}_{h_p} \in \mathbb{R}^{3\times3}$ and $\mathbf{K}_{h_o} \in \mathbb{R}^{3\times3}$ are diagonal proportional gain matrices for the position and orientation. e_{h_p} and $\boldsymbol{e}_{h_o}$ are the Cartesian position and orientation errors as defined in [143].

Fig. 20 shows the virtual interaction forces and the temperature of the hand. Fig. 20-a shows the temperature measured by the taxels of the hand the threshold κ_0 that activates the task. When one single taxel crosses the temperature threshold of 31 °C threshold, the virtual interaction wrench $\boldsymbol{w}_\kappa$ is generated. The norm of components of this wrench is plotted in Fig. 20-b. $\boldsymbol{f}_\kappa$ is the virtual interaction force and $\boldsymbol{\eta}_\kappa$ the virtual interaction torque, both in O_{hand} coordinate frame. The joint torques of the right arm are plotted in 20-c. There, we can see the torques generated by the Cartesian Position and Orientation hand before the temperature increases in the hand. 20-d shows the joint velocities of the right arm generated during the experiment.

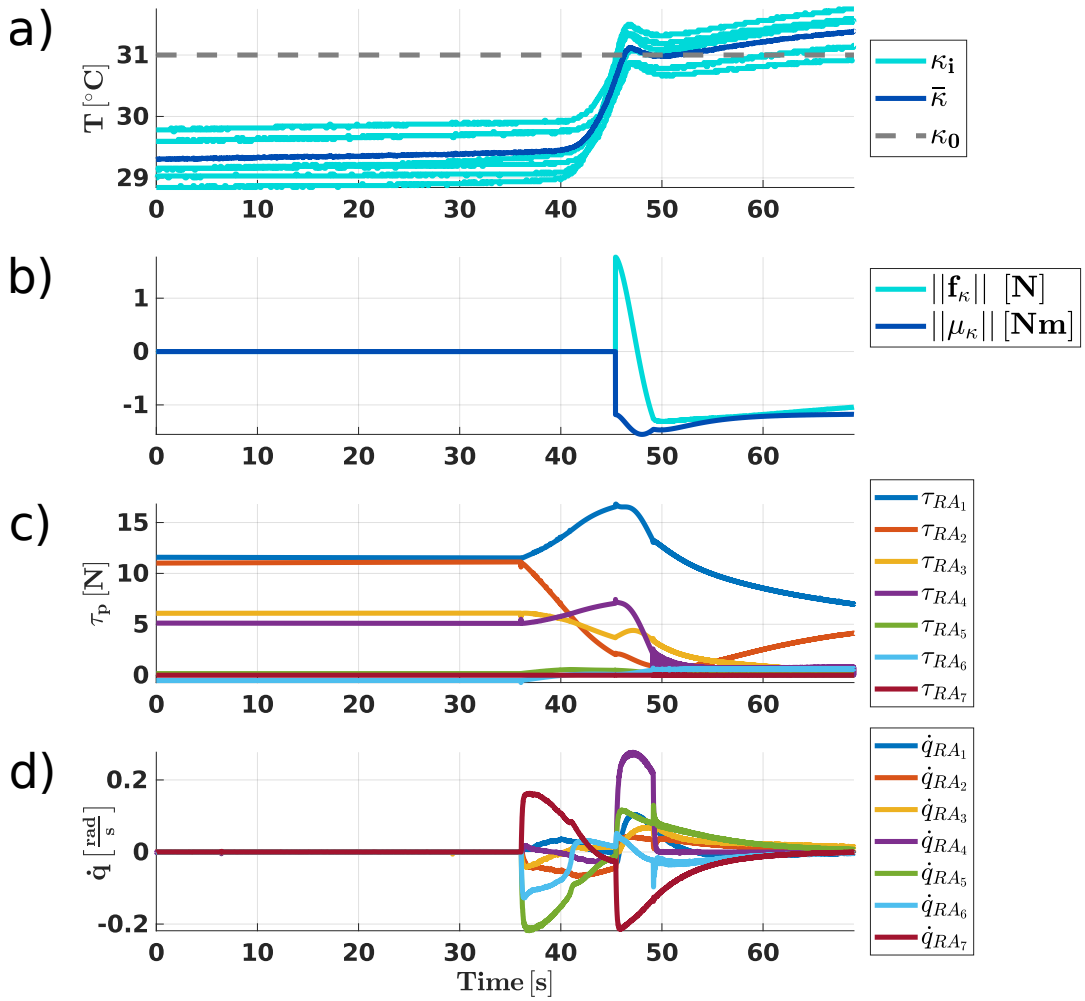

Figure 20 Virtual interaction forces, torques and velocities during the experiment. a) The temperatures measured by the 7 taxels in the hand back κ_i, the average temperature $\bar{\kappa}$, and the thershold κ_0. b) virtual interaction wrench $\boldsymbol{w}_\kappa$ composed by the force $\boldsymbol{f}_\kappa$, and the torque $\boldsymbol{\eta}_\kappa$. b) shows the joint-torques of the right arm. c) shows the joint velocities generated by the reaction motions.

3.4. Combination of Direct and Virtual Interaction Tasks in Whole-Body Behaviors

This chapter introduced the formulations of direct and virtual interaction tasks that exploit the different sensing modalities available in robot skins. The experiments in Sections 3.2.3.1, 3.2.4.1, 3.3.1.1, and 3.2.5.1 showed the performance of the tasks on whole-body interactions in a full-size humanoid robot. These experiments imply also the fusion of the interaction tasks with constraint tasks (the balance/support task) and full-rank tasks at the bottom of the hierarchy. We can combine different modalities of interaction tasks to fulfill the requirements of applications that require manipulation with awareness of the environment.

The cooking simulation experiment in Section 3.3.2.1 brings the multi-modal interactions into a meaningful purpose which uses the task hierarchy to cancel (or block) a task when the robot's integrity is compromised. Additional sensory information can also be used to manage the priorities of the tasks when the interaction (direct and virtual) show a certain pattern. Let us analyze two cases where multi-modal tactile information serves a higher level of purpose than the feedback for the interaction alone.

3.4.1. Task priority adjustment for nociceptive reflex in robots

Humans and animals have several modalities of nociception distributed along the body [141]. In [79], Bagnato et al. highlight the advantages of self-diagnosis and nociception in biological systems and the approaches take in robotics to emulate these features. Nociception in robots can help prevent overloads of the actuators, and detect unusual operating conditions as, for example, a worn bearing that can break soon and cause damage to the system. Let us explore how tactile information can be used for a basic modality of nociception and its implications in the hierarchical task execution developed in the previous sections.

The cooking simulation experiment in Section 3.3.2.1 showed a first insight on robot nociception where the robot senses a potentially harmful interaction and triggers a reactive motion to it. The pressure-driven interaction wrench in the experiment of Section 3.2.5.1 distinguishes between interaction forces highly concentrated in a small area and distributed interaction over a larger area. This behavior can serve to implement a direct force interaction task in the hand while keeping the contact pressure under a safety boundary. When the pressure is high, the interaction task amplifies the force and the reaction motion is, in a sense, similar to the arm retraction in the cooking experiment. If a similar interaction is applied over human skin, there is one threshold in the pressure that will stimulate the mechanical nociceptors in the skin and activate a retraction reflex similar to the one that a burning contact produces. Let us elaborate on this idea in a case study experiment with the H1 robot.

3.4.1.1 Experiment: nociceptive reflex for robots

In this experiment, the default task priorities are as follows:

1. Balance / supporting task.
2. Right hand Cartesian position task.
3. Right hand Cartesian orientation task.
4. Pressure-driven compliance task.
5. Posture task.

The robot must keep balance and react to the contact pressure as in the previous experiment. However, with a higher priority, the Cartesian tasks are keeping the position and orientation

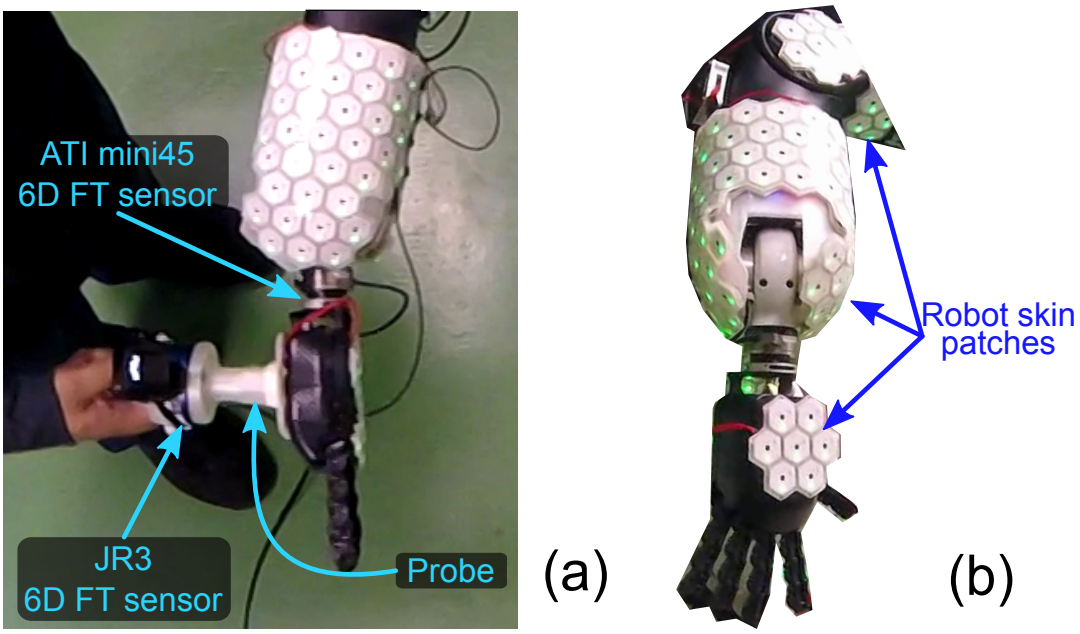

Figure 21 (a) Force sensors used in the experiment. A JR3 force-torque sensor was mounted on the probe and an ATI mini45 force-torque sensor in the wrist of the robot. (b) The arm is covered with robot skin which provides contact force information (pose, magnitude and area).

of the right hand. Then, when a highly concentrated force $||\boldsymbol{f}_P|| > \epsilon$ is detected and keeping the Cartesian tasks from being accomplished, they will be deactivated, releasing all the DoF for the pressure-driven compliance task. The idea is to verify the feasibility of the higher priority tasks in the robot behavior and cancel them if a highly concentrated force (potentially harmful) is sensed by the robot. Therefore, when a high-pressure interaction is detected, the task priorities are rearranged as:

1. Balance / supporting task.
2. Pressure-driven compliance task.
3. Posture task.

Two probes were used to distribute the contact force in different areas. The first probe is designed to concentrate the contact force into a single taxel area (see Fig. 22-a). The second probe covers a seven-taxel area and thus generates lower contact pressure than the first probe when applying the same external force (see Fig. 22-b). The interaction forces were monitored with an force-torque sensor mounted at the wrist of the robot in a classical configuration of an end-effector (see Fig. 21-a). The interaction forces using the single-taxel probe are plotted in Fig. 23-a. The threshold for the virtual force to deactivate the Cartesian controllers was set to 10N. The threshold was exceeded when applying a small force with the single-taxel probe. Conversely, with the seven taxel probe (see Fig. 23-b), the force to cancel the Cartesian tasks was considerably larger than in the previous case.

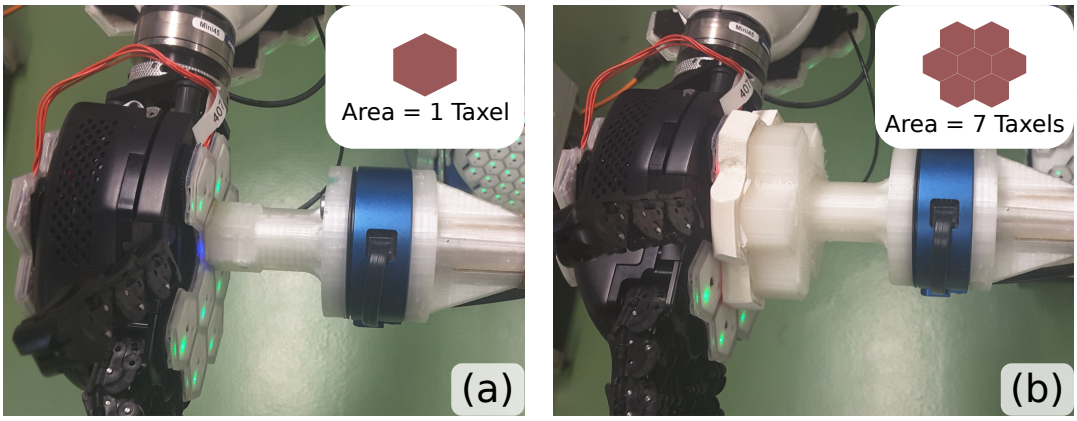

Figure 22 Probes mounted on a force-torque sensor to generate different pressure distributions with the same force. (a) Area of one skin taxel. (b) Area of seven taxels.

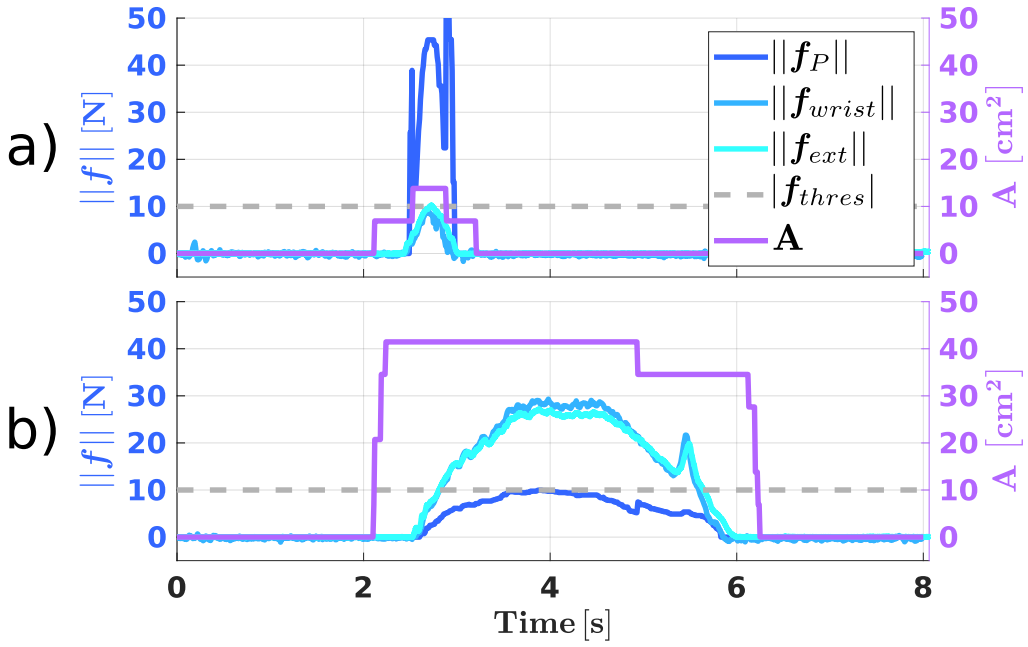

Figure 23 Interaction forces measured in the experiment. The upper plot shows the data of the experiment using the 1-taxel area probe. The lower plot shows the data when the 7-taxel area probe was used. $||f_{ext}||$ is the norm of the external contact force applied by the probe. $||f_{wrist}||$ is the norm of the force measured by the force-torque sensor mounted at the wrist of the robot arm, $||f_P||$ is the norm of the virtual force (first three elements of w_P), A is the contact area measured by the robot skin. The higher-priority Cartesian tasks are disabled when $||f_P|| > f_{thres}$.

3.4.2. Task priority adjustment for intentional contact

Potential fields are widely used in robotics to prevent collisions [59, 144]. However, choosing a proper function to define the vector fields may become difficult. Local minima can get the trajectory stuck into undesired equilibrium points trying to avoid contacts as shown by [145]. Such a scenario may keep the robot from accomplishing other tasks, for instance, tracking a certain position or orientation on the end effector.

Some strategies to escape from local minima have been proposed as the virtual obstacle approach in [146] or the hierarchical execution of tasks in [137]. Within this hierarchical approach, collision avoidance can be defined as a task between other goals and safety tasks.

Let us define a task hierarchy policy to manage task priorities according to tactile data provided by multi-modal robot skin. Such policy allows reducing the safety tasks like collision avoidance and physical interference compliance to simple potential field rules. It is well known that potential fields are prone to undesired behaviors such as oscillations and stagnations due to local minima [145]. However, with this scheme, smooth task priority changes are triggered when local minima are detected in presence of obstacles allowing the robot to touch objects in the environment under a defined tolerable force.

The concept of "*Intentional Contact*" is introduced in this work as a tool to explore and clear mobile obstacles from the environment in order to enable the execution of the goal tasks. Skin force feedback during the Intentional Contact phases lets the policy trigger an emergency rearrangement if the contact force exceeds a permitted rank. In that scenario, reducing the contact force takes the highest priority. The proposed policy can be applied to any hierarchical task manager on position, velocity, or force-controlled robots.

Let an end effector position task be defined as

$$\boldsymbol{\tau}_g =^0 \mathbf{J}_{ef}\left(\boldsymbol{q}\right)^\top \boldsymbol{f}_g\left(\boldsymbol{x}, \dot{\boldsymbol{x}}\right) \tag{3.40}$$

where $\boldsymbol{\tau}_g \in \mathbb{R}^n$ is the torque vector needed to achieve the task, ${}^0\mathbf{J}_{ef} \in \mathbb{R}^{m\times n}$ is the Jacobian matrix for the end effector and $\boldsymbol{f}_g \in \mathbb{R}^m$ is the desired wrench or force in task space produced by a control law to track the desired trajectory of the end effector whose position and velocity are described in task coordinates by $\boldsymbol{x} \in \mathbb{R}^m$ and $\dot{\boldsymbol{x}} \in \mathbb{R}^m$, respectively. The sub-index g was chosen to denote a goal task.

On a common implementation, it is expected that the goal task is executed avoiding any collision. This can be done by adding the proximity task Eq. (3.33) and Eq. (3.40). However, the usage of added potential fields may lead to local minima producing undesired equilibrium points on the robot trajectory [145]. If the robot's path falls in one of those regions, it would be detected if the norm of the velocity vector $\dot{\boldsymbol{x}}$ decreases to a value lower than a desired transitory threshold ϵ_v. In such a case, switching of the control law must be considered, for instance, a reduction in the sensing range allowing the robot to approach objects in order to

carry out the goal task.

If the sensing range is decreased to zero and the goal task is still not fulfilled, then the robot can exert forces on the environment to modify its configuration in order to clear the path for the goal task. Following this idea and taking advantage of the capabilities of the artificial skin, a robot can exert *Intentional Contacts* on surrounding objects and reallocate them to make the goal task feasible. Tactile feedback during the contact makes it possible to keep all the contact forces below a defined margin ϵ_c and step back if it is exceeded.

The force limit may be defined by the resilience of the skin layer and also the surrounding objects. Therefore, the system should be able to push and move light objects while fulfilling all the other tasks and reactively respect all the hard physical constraints of the environment. To ensure this, the skin should be able to measure the contact force knowing exactly the point where it is being applied on the robot's body in order to compute a response torque similar to Eq. (3.33) as

$$\boldsymbol{\tau}_c = \sum_{i=1}^{k} \mathbf{J}_{c_i}^T (\boldsymbol{q})\, \boldsymbol{f}_{c_i} \tag{3.41}$$

where $\boldsymbol{\tau}_c \in \mathbb{R}^n$ is the needed torque vector to relax the contact force, $\boldsymbol{f}_c \in \mathbb{R}^m$ is the contact force measured in task space and $\mathbf{J}_{c_i} \in \mathbb{R}^{m \times n}$ is the Jacobian matrix which defines the differential kinematic mapping between the task space of dimension m and the joint space of dimension m for the surface point where the force is located at the i-th sensed contact point in a set of k measuring points.

According to the proposed behavior, three priority arrangements shall be considered as shown in Table 1.

The conditions in Table 1 are used for triggering transitions between the three cases. Here, smooth transition methods can help to keep joint torques under feasible values and to avoid overshoot behaviors and chattering on the robot performance which could lead to damage of the mechanical components.

3.4.2.1 Experiment: Intentional contact in simulation

In order to corroborate that the proposed policy matches the desired behavior, a simulated environment was set with a planar 7-DOF robot. The robot was provided with skin-like sensing capabilities to measure contact forces and proximity on every link, emulating the functionality of artificial skin. Two goal-tasks are defined. The higher priority task is to reach and keep a desired position with the end effector, keeping the velocity bounded during long displacements. This control law is described in [58], where the desired speed $\dot{x}_d$ is defined with

(a) Transitory phases with collision avoidance

Priority	Task id	Task name	Conditions
1	$\boldsymbol{\tau}_p$	Obstacle avoidance	$0 \leq \|\|\boldsymbol{f}_p\|\|$
2	$\boldsymbol{\tau}_g$	Goal task set	$\epsilon_v < \|\|\dot{\boldsymbol{x}}\|\|$
3	$\boldsymbol{\tau}_c$	Contact reaction	$\|\|\boldsymbol{f}_c\|\| = 0$

(b) Intentional approach and contact

Priority	Task id	Task name	Conditions
1	$\boldsymbol{\tau}_g$	Goal task set	$0 < \|\|\boldsymbol{f}_p\|\|$
2	$\boldsymbol{\tau}_c$	Contact reaction	$\|\|\dot{\boldsymbol{x}}\|\| \leq \epsilon_v$
3	$\boldsymbol{\tau}_p$	Obstacle avoidance	$0 \leq \|\|\boldsymbol{f}_c\|\| < \epsilon_c$

(c) Hard contact reaction

Priority	Task id	Task name	Conditions
1	$\boldsymbol{\tau}_c$	Contact reaction	$0 \leq \|\|\boldsymbol{f}_p\|\|$
2	$\boldsymbol{\tau}_g$	Goal task set	$0 \leq \|\|\dot{\boldsymbol{x}}\|\|$
3	$\boldsymbol{\tau}_p$	Obstacle avoidance	$\|\|\boldsymbol{f}_c\|\| \geq \epsilon_c$

Table 1 Priority arrangements for obstacle avoidance and *Intentional Contact*

respect to the distance to an attraction point in Cartesian space

$$\dot{\boldsymbol{x}}_d = \frac{k_p}{k_v}\left(\boldsymbol{x}_d - \boldsymbol{x}\right) \tag{3.42}$$

where the k_p and k_v are proportional and derivative scalar gains respectively. With this desired end effector speed, a force vector is defined

$$\boldsymbol{f}_g = -k_v\left(\dot{\boldsymbol{x}} - \nu\dot{\boldsymbol{x}}_d\right) \tag{3.43}$$

where the speed saturation function is defined as

$$\nu = \min\left(1, \frac{V_{max}}{\sqrt{\dot{\boldsymbol{x}}_d^T\dot{\boldsymbol{x}}_d}}\right) \tag{3.44}$$

being V_{max} a maximum speed value allowed for the system.

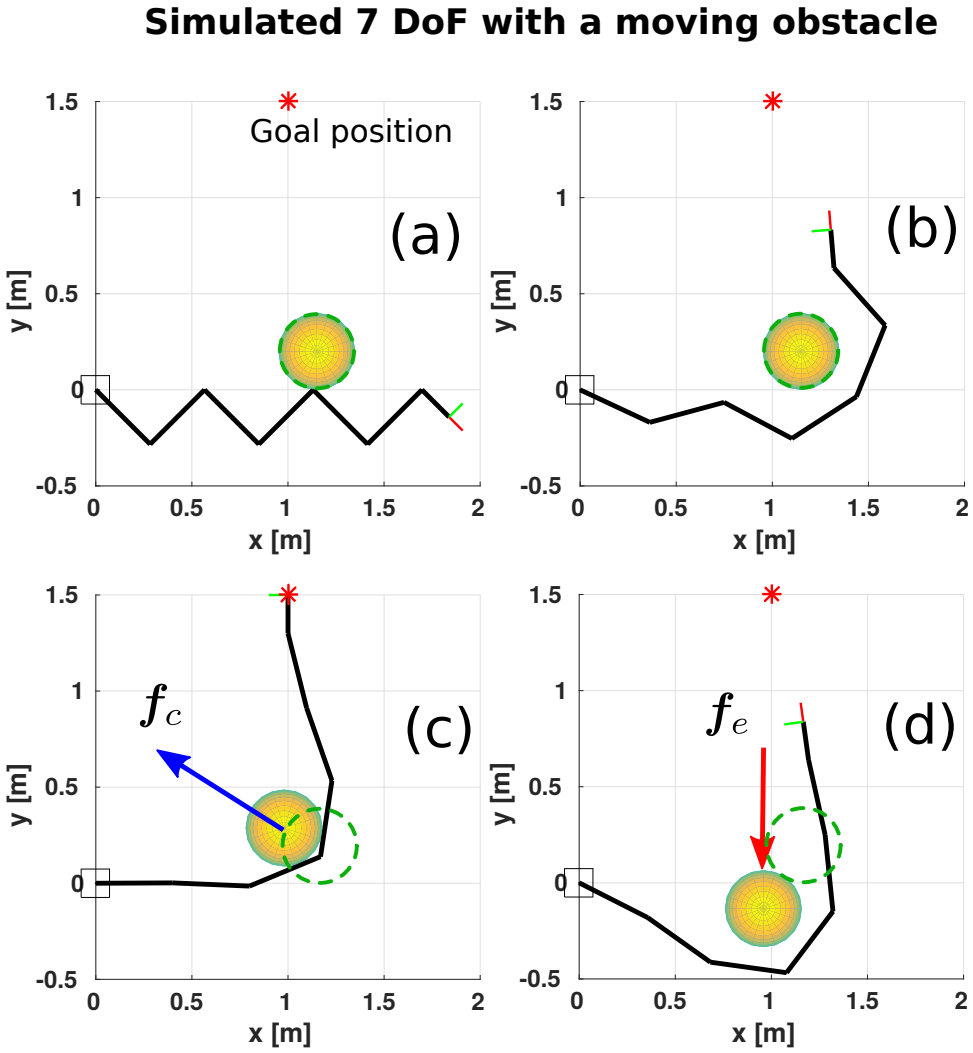

Figure 24 Stages of the proposed skin reactive policy. (a) Initial condition, the robot's first reaction is to avoid the obstacle. (b) The robot tries to reach its end effector goal position but falls into a local minimum due to the potential fields nature. (c) *Intentional contact*, the robot approaches and pushes the obstacle with a contact force $\boldsymbol{f}_c$ lower than the permissible threshold ϵ_c in order to fulfill the goal-task, the original pose of the obstacle is marked by the dashed circle. (d) Hard contact reaction, an external force $\boldsymbol{f}_e > \epsilon_c$ is applied to the obstacle so it moves and transfers the force to the robot which moves to reduce the contact force.

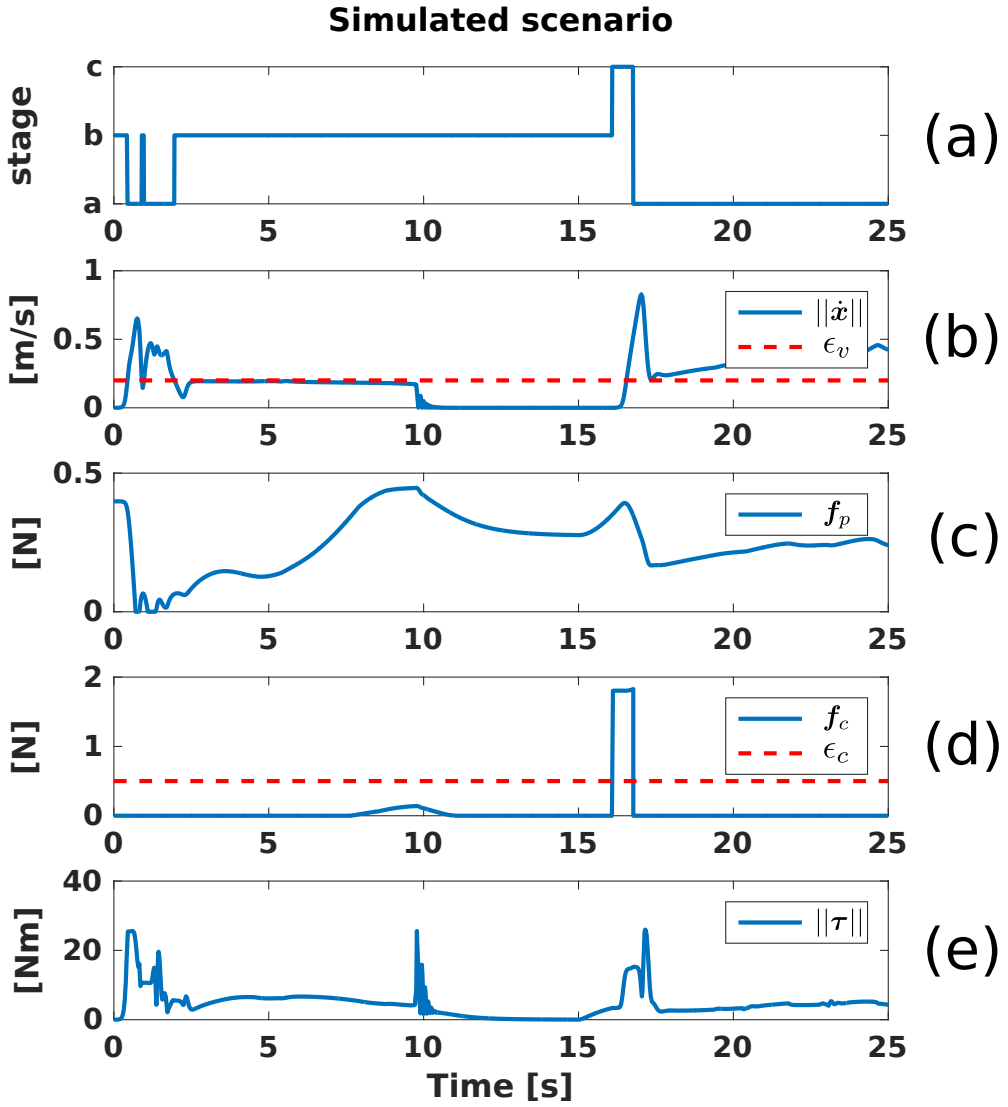

Figure 25 (a) Priority arrangement according to Table 1. (b) End effector speed and minimal value to consider a local minimum in $\left[\frac{m}{s}\right]$. (c) Force produced by proximity sensors at the closest point to an obstacle in $[N]$. (d) Highest contact force detected by the skin and maximum permitted contact force in $[N]$. (e) Norm of the torque vector $\boldsymbol{\tau}$ in $[Nm]$.

The second task is to keep the end effector oriented vertically, pointing in the positive direction of $y - axis$. For this task, the control law is the same but considering the end effector's orientation. A movable obstacle is placed between the initial position of the robot and the desired end-effector position to induce a local minimum on the execution of the tasks.

The proposed task-priority policy was implemented using the augmented Jacobian null-space projection described in [68] with soft transitions defined as

$$\tau = \chi\tau_{k-1} + (1 - \chi)\tau_k \tag{3.45}$$

where

$$\chi = \frac{(1 - \tanh(\delta_t (t - t_t)))}{2} \tag{3.46}$$

with τ_{k-1} being the output torque at the moment when the transition was triggered, τ_k the output torque with the new priority arrangement, t the time, t_t the specific instant the transition was triggered, and δ_t a smoothing gain.

Fig. 24 plotted the interaction between the robot and the obstacle while the tasks are executed. The forces acting on the robot and the transitions between the task arrangements during the process are shown in Fig. 25.

3.4.2.2 Experiment: intentional contact using tactile feedback

In order to evaluate the proposed concept on a physical platform, a robot manipulator covered with skin is needed. The skin must be able to measure both contact force and proximity in a reasonable range. Our robot TOMM [125] covers those requirements as shown in Section 2.3.1.

In this experiment, the mobile base was fixed to the ground and a position control task was implemented for the end effector. The position control task will track the desired position with the end effector of TOMM's right arm over a table. Under these conditions, two scenarios were tested. In the first one (Fig. 26), non-fixed obstacles were be placed in the path to the goal position and the robot had to move them in order to fulfill the goal-task as long as the contact force remains under the tolerated value. One of the obstacles was placed exactly in the desired position. In the second scenario (Fig. 27), a non-fixed obstacle and a fixed obstacle was be placed on the robot's path specially configured to induce the classic local minimum problem using the potential fields. The robot tries to reach the desired position and faces the local minima produced by the obstacles. When the *Intentional Contact* occurs, the robot makes its path to the desired position by pushing and moving the non-fixed obstacle around the fixed one. The only information provided to the robot in this experiment is the desired position and orientation for the end effector to set the goal task. No information about the obstacles is needed.

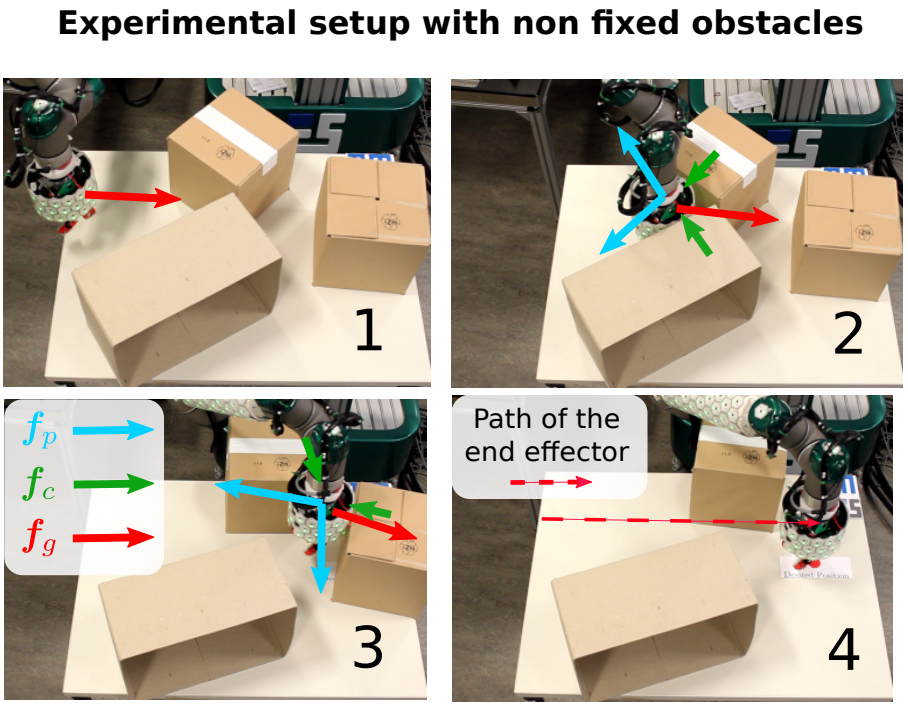

Figure 26 (1) Initial position. (2) Local minimum reached. (3) *Intentional Contact* to move the obstacles. (4) Goal position reached. Red arrows describe the Cartesian velocity of the end effector. Blue arrows describe repulsive force generated by the movable objects when they are close to the robot. Green arrows describe de contact forces between the robot and the obstacles. Red arrows describe the attractive force induced by the desired position.

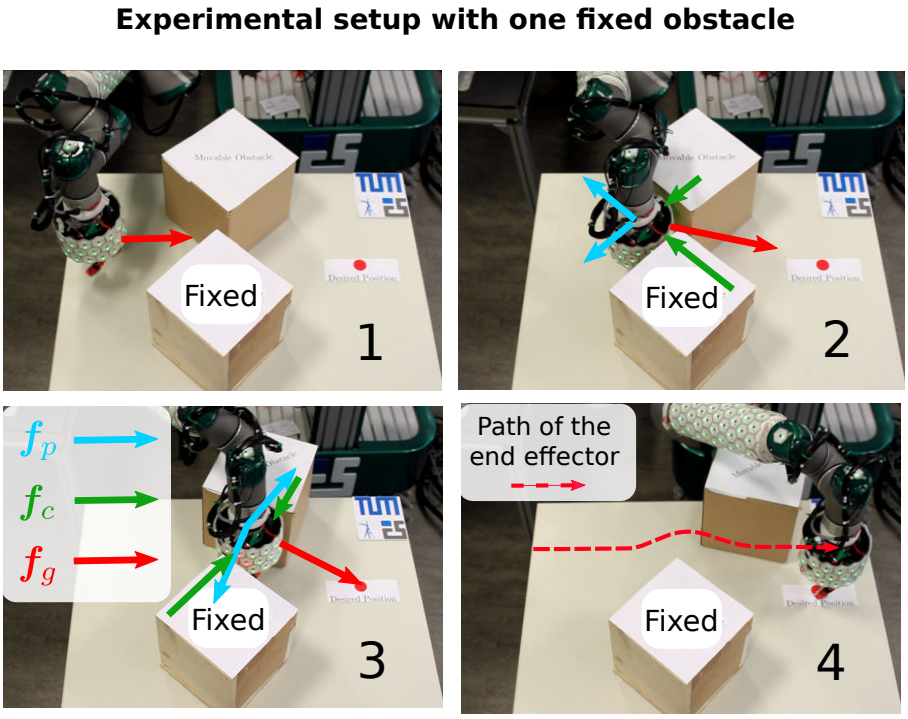

Figure 27 (1) Initial position. (2) Local minimum reached. (3) *Intentional Contact* to move the non fixed obstacle. (4) Goal position reached. Red arrows describe the Cartesian velocity of the end effector. Blue arrows describe repulsive force generated by the movable objects when they are close to the robot. Green arrows describe de contact forces between the robot and the obstacles. Red arrows describe the attractive force induced by the desired position.

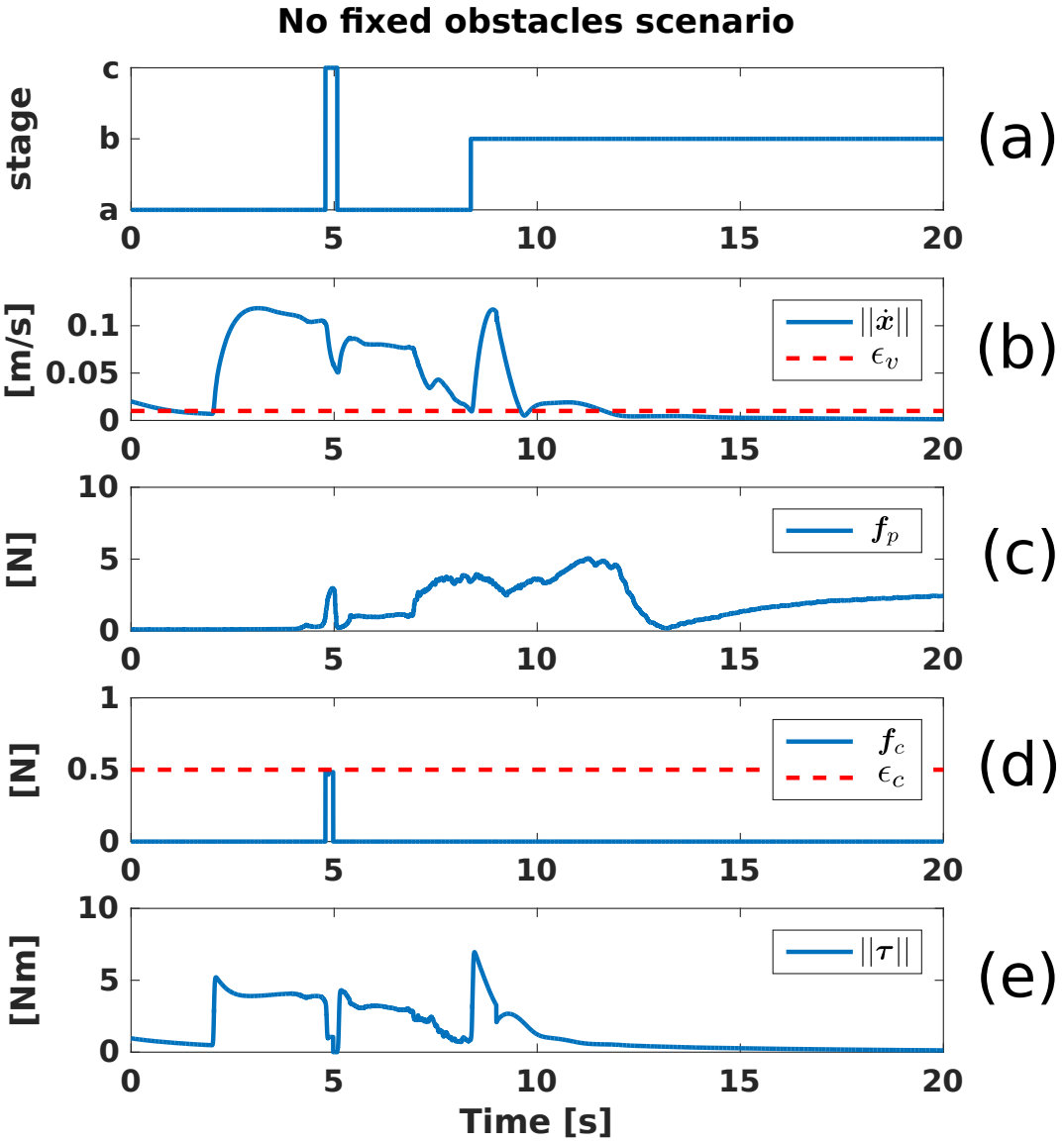

Figure 28 Movable obstacles scenario. (a) Priority arrangement according to Table 1. (b) End effector speed and minimal value to consider a local minimum in $\left[\frac{m}{s}\right]$. (c) Force produced by proximity sensors at the closest point to an obstacle in $[N]$. (d) Highest contact force detected by the skin and maximum permitted contact force in $[N]$. (e) Norm of the torque vector τ in $[Nm]$.

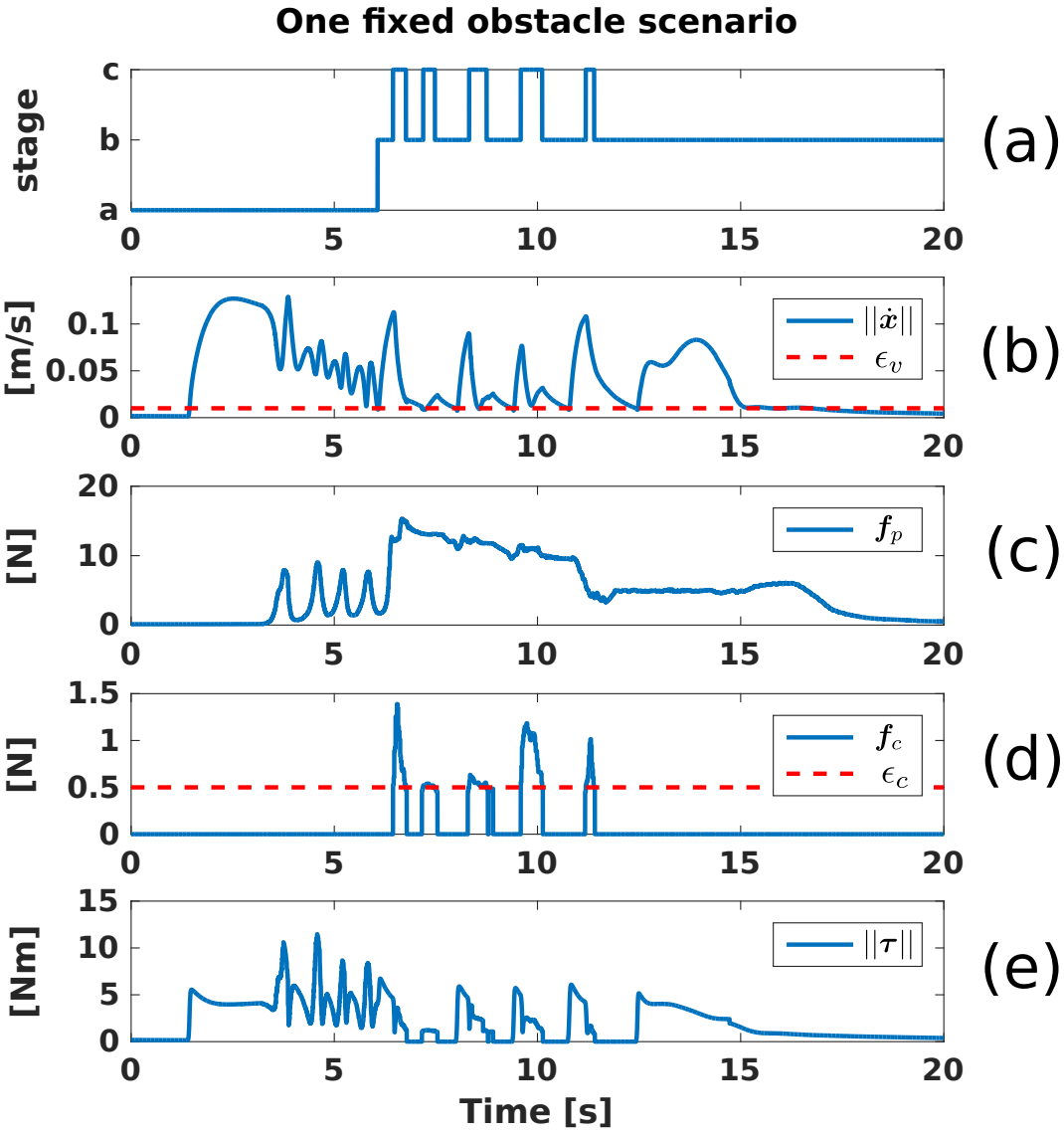

Figure 29 Non movable obstacle scenario. (a) Priority arrangement according to Table 1. (b) End effector speed and minimal value to consider a local minimum in $[\frac{m}{s}]$. (c) Force produced by proximity sensors at the closest point to an obstacle in $[N]$. (d) Highest contact force detected by the skin and maximum permitted contact force in $[N]$. (e) Norm of the torque vector τ in $[Nm]$.

In Figures 28 and 29 the interacting forces during the experiment, as well as the priority arrangement configuration according to Table 1 are displayed. In the contact force graph from Fig. 29, a number of *Intentional Contact* attempts are shown, along the path around the fixed obstacle.

The presented hierarchical policy for interaction provides a reactive way to explore and modify the environment keeping safety as the main concern. It can be implemented under different conditions according to the needs of the applications. Other control laws and hierarchy management methods are supported for the proposed set of conditions. The use of potential fields prevents collisions and enables soft interaction contact events to prevent damage to the mechanical parts and the skin itself.

Intentional Contact allows a robot to interact with its environment in order to fulfill the goal tasks[2]. The concept can be applied to other perception technologies but artificial skin expands the idea to the whole body. Tactile feedback plays an important role during the *Intentional Contact* phases because the contact force must be constantly monitored as it is responsible for triggering the hard-contact task priority arrangement. Enabling Intentional Contact in a robot makes it possible to clear the path along with unknown scenarios without considering the dynamical properties of the obstacles. The major advantage of this approach is that no previous knowledge about the environment is required. The behavior of the robot is completely reactive to the environment, task priority rearrangements are triggered by interaction events that can be also used to modify controller gains and adjust thresholds and tolerances for different operational conditions.

3.5. Summary

This chapter transformed the operational space formulation from Khatib to physical direct and virtual interactions using robot skin. We use the spatial distribution of multiple sensors provided by robot skin to directly measure interaction forces and environmental conditions to generate reactive motions in the whole body of stiff (position-controlled) robots.

Distributed force-sensing was used to formulate interaction tasks in Section 3.2 which enabled a compliant behavior to external forces, similar to the body compliance achieved with joint torque sensors, such as with the KUKA LWR. The formulations were tested in a highly redundant system, a 30 DoF floating base humanoid robot fully covered with skin (Fig. 3). To cope with the redundancy of the robot, we used strict hierarchical task execution to fuse several instances of physical interaction tasks with posture and purpose tasks with different priorities. The prioritized combination of tasks helps generate whole-body behaviors that guarantee that the primary tasks, such as balance and supporting contacts, are executed on top of the purpose tasks that do not compromise the integrity of the robot or the operators.

[2] This work on *Intentional Contact* was presented at a peer-reviewed international conference in [74].

Distributed sensing requires the generation and processing of large amounts of information that, in practice, increases the computational load of the system. However, different methods and technologies can be applied to improve the performance of handling large amounts of tactile information. Skin systems improve the generation and communication of tactile information with neuromorphic approaches as the event-based protocol in [46]. On the application side, which is the concern of this thesis, traversing the taxels to generate the interaction tasks is time-consuming and can break the real-time loop of a controller if the amount of taxels is too large. In this thesis, we proposed a method to discard the information that is not relevant for the interactions, for example skipping the computations related to the taxels that measure forces smaller than a set range. We showed the potential of this approach by enabling several simultaneous interactions over the whole body of a robot in the experiment in Section 3.2.4.1.

The advantage of distributed force sensing over joint-torque sensors lies in the additional geometric information it provides about the contact interactions. While joint torque sensors measure the resultant body torques caused by the external forces, distributed force sensing can detect when multiple contacts are applied over the same link and the areas where the contact forces are applied. This additional information allows the generation of alternative body compliance modalities as in the case of the pressure-driven body compliance presented in Section 3.2.5.1.

Pressure-driven body compliance amplifies the forces that are concentrated in small areas producing fast reactions and dampens the forces distributed over large surfaces providing the capability of handling high payloads as long as they are distributed. This modality of compliance was inspired by the way we handle heavy loads in everyday life. We distribute the contact of heavy objects in larger areas to prevent damaging our bodies. We can measure the contact pressure with our skin, and when it presents a threat, it activates the nociceptor of our skin that triggers nociceptive reflections to protect ourselves. We followed this behavior in Section 3.4.1.1 to design a way of mechanical nociception for robots that cancel the execution of an interaction task when the interaction forces are highly concentrated.

Distributed sensing of other modalities provides information on the environment that helps to generate other types of body behaviors. However, sensing modalities different from contact force shall not be treated as direct physical interactions because they do not involve direct contact between the robot and the environment. We can use these measurements to generate virtual repulsive or attracting forces that produce body reactions but do not introduce external forces in the model. This difference is most important for floating base robots because virtual interactions must not be considered in the supporting contacts for balance controllers. Therefore, all the virtual interactions must be handled with lower priority than the direct physical interactions to keep the equilibrium in the supporting contacts. This distinction will be highlighted in Chapter 4 where the modalities of contact force and proximity sensing will be used as feedback for biped locomotion.

This chapter presented two modalities of virtual interactions using distributed sensors. In Section 3.3.1, distributed proximity sensors were used to generate repellent potential fields from the environment geometry. These repulsive fields push the robot body away from any object in the environment. This modality of virtual interaction enables a collision avoidance behavior over the whole body that requires no other perception system than the skin and the robot kinematic chain. Similarly, distributed temperature sensors were used to produce a temperature-driven modality of body compliance. We used the formulation for virtual interactions to generate repulsive forces triggered from temperature measurements. The experiment in Section 3.3.2.1, shows a robot in a cooking scenario that detects the temperature of the hand is rising fast, and it generates a pushing force that retracts the hand to put distance between the hand and the source of heat.

Finally, in Section 3.4.2 direct and virtual interactions were combined to achieve an end effector task activating intentional contacts of the robot with the environment. Proximity-based collision avoidance was combined with a Cartesian control of the end effector. When the repulsive fields of the collision avoidance task fall into local minima, a priority rearranges of the tasks enable the robot to come closer to the environment and exert contact forces to modify it in the pursuit of fulfilling the end effector task. Distributed force sensors allow the robot to measure the contact forces and distinguish whether a part of the environment can be pushed away or if it is fixed. With this behavior, the robot pushes away movable obstacles avoiding fixed obstacles, clearing the path to fulfill the end effector task. The intentional contact behavior is only possible by combining direct and virtual interactions with distributed sensing points. The framework for handling direct and virtual interactions presented in this thesis allows the generation of this kind of body behavior that expands the capabilities of robots in complex environments.

Overall, this Chapter presented the formulations to combine different modalities of sensor feedback into whole body behaviors. The interaction tasks can be applied in fixed based and floating base robots as the TOMM robot (Fig. 2) and the H1 robot (Fig. 3). The whole body behaviors combining interaction modalities allow a robot to interact with the environment and even to modify it if an application requires it.

4. Tactile Based Bipedal Robot Balance and Locomotion

This chapter presents the formulations to exploit multi-modal tactile feedback for bipedal robot balance and locomotion. The sensing modalities introduced in Chapter 3 are now applied for plantar sensing to measure the interaction forces between the foot and the terrain. The distributed direct force measurements provide the information to estimate the significant metrics for bipedal robot balance control [147] that are commonly measured using ankle force-torque sensors. These metrics include the ZMP, CMP, GRF, and the DCM, also called CP (Capture Point). Additionally, the geometric information on the contacts helps approximate the supporting polygon which provides the boundaries for guaranteeing stable footholds during standing and walking.

The plantar tactile information provides complementary information that is highly valuable for bipedal robot walking controllers. Knowing the geometry of the supporting polygon allows assessing a foothold immediately after foot landing without the need for exploratory motions or complex visual systems. With the instant information on the foothold, a robot can decide whether it is safe to step on it or a step retargeting is required to find a better suitable foothold. Furthermore, the proximity sensing modality provides preemptive geometric information of the terrain during the foot landing motion while walking. This modality allows the formulation of the preemptive foot compliance that increases the robustness of a walking controller to unknown terrain conditions.

This chapter also provides the formulations to use the supporting polygon geometry to define constraints for the robot balance controllers. Two examples will be presented that incorporates the plantar tactile feedback into two different walking controllers in two different full-size humanoid robots. The bounding box of the supporting polygon will be used to redefine the friction cone constraints introduced by Caron et al. in [8]. The tactile information lets us remove the full-sole contact assumption required in several walking controllers as [127, 148, 6]. The supporting polygon can also be used to constraint the adjustments to the reference ZMP in the DCM feedback-based balance controller proposed by Englsberger et al. in [6].

Walking over partial footholds requires the knowledge of the contact geometry to define the constraints of the motions. But to keep the dynamic stability, the walking motions must be adjusted to respect these constraints. Nevertheless, the tactile information provides the insights needed to adapt the walking reference trajectories online right after foot landing. We provide the formulations to apply these changes from tactile information that achieve continuous dynamic walking over partial footholds.

The formulations for balance and control with plantar tactile feedback presented in this chapter are generalized to be applied with any skin system that provides distributed force sensing. We will present the advantages of having additional sensing modalities (e. g. proximity sensing) for enhancing walking motions online using the formulations of virtual interactions introduced in Chapter 3.

Aside from the proximity sensing modality, different robot skins can be applied for tactile sensing. However, most of the available solutions require deep modifications in the foot design to incorporate the tactile sensors. In this thesis, we propose a simple but practical solution to mount tactile sensors on the feet of humanoid robots that require no permanent changes in the robot's legs: mountable shoes.

Mountable shoes can provide plantar tactile sensation to a robot in less than five minutes of setup time. They also facilitate unmounting for maintenance and repairments of the tactile sensors and the versatility to modify the skins for different applications. To test the formulations in this chapter, tactile shoes were built for the HRP-2Kai robot [3] and the H1 robot [149] as shown in Figures 3 and 5.

This chapter is presented with the following layout: Section 4.1 will review the fundamentals of biped balance and walking control required to elaborate the contributions of this thesis. Section 4.2 will introduce the modalities for plantar tactile sensation and the metrics calculated from it. Section 4.3 introduces the application of plantar tactile feedback into balance and walking controllers for full-sole flat footholds. Two experiments are presented to compare the performance of a robot with plantar tactile feedback with a robot using the classic ankle force-torque sensors. Section 4.4 applies the plantar sensation for walking on uneven terrain and partial footholds. We expand the formulations of balance and walking control to use the supporting polygon, and introduce the PFC modality using plantar proximity sensing. Several validate these formulations running in both the HRP-2kai and the H1 robots. Finally, Section 4.5 summarizes the results and contributions of the Chapter.

Along this chapter, the subscript $(\bullet)_f$ denotes that the vector $(\bullet)$ was generated from the force sensing modality of the skin. Likewise, $(\bullet)_p$ denotes the proximity sensing modality.

4.1. Background on Balance and Walking Control

Biped walking is a complex process composed of a succession of antagonistic interactions that must be controlled within strict boundaries to keep a harmonic pace from one step to another [150, 151, 152]. At a glance, the dynamics of walking split into two phases: single and double support [153].

During the double support phases, the body swings from above one foot to the other, transferring the weight from one foot to the other in a smooth transition that eventually releases all the load of the rear foot. Then, the single support phase starts pushing forward the body over the supporting leg and swinging the free leg to the next foothold and the cycle starts over again.

A biped robot is modeled as a floating base system (Eq. (3.12)) where the supporting contacts are external forces applied on the feet. The phases of walking are produced by the control of these interactions between the feet and the ground. However, to reduce the complexity of the problem, a common strategy is to simplify the dynamics using a low-dimensional model to approximate the interactions required for walking [154].

4.1.1. Linear inverted pendulum model (LIP)

The most common simplified model for bipedal walking is the LIP. As illustrated in Fig. 30, the body is seen as a point mass located on a stretchable inverted pendulum so that the height of the CoM z_x is kept constant. In this representation, the CoM position in the world coordinate frame $O_{\mathbf{w}}$ is given by $\boldsymbol{x} \in \mathbb{R}^3$, and its velocity and acceleration are $\dot{\boldsymbol{x}} \in \mathbb{R}^3$, and $\ddot{\boldsymbol{x}} \in \mathbb{R}^3$ respectively. The pendulum's fulcrum is located on the ground on a point $\mathbf{p} \in \mathbb{R}^3$ such that the GRF $\boldsymbol{f}_{GR} \in \mathbb{R}^3$ concentrates all the dynamic forces produced by the motion of the CoM and the gravity. Therefore, we can describe the motion of the CoM using the LIP model as

$$\ddot{\boldsymbol{x}} = \omega^2(\boldsymbol{x} - \mathbf{p}) \tag{4.1}$$

where $\omega = \sqrt{\dfrac{g}{z_x}}$ is the radian frequency of the pendulum defined by the gravity acceleration g and the height of the pendulum z_x.

4.1.2. Zero moment point (ZMP) and supporting polygon

While the LIP model provides a simple way to represent the reaction forces involved in walking, the realization of these motions requires the control of the legs to reproduce the desired resultant forces with the foot's sole over the ground. However, as a floating base system, a biped robot is prone to tilting over if the interactions are not kept in equilibrium. Furthermore, to realize the GRF required by the LIP model, the contact between the supporting foot and the ground must be keep static. Therefore, the primary concern to realize walking motions is to guarantee the stable contact of a foot sole with the ground.

The formulation of the ZMP as a metric for contact stability was introduced by Vukobratović in [155]. Let us analyze the 2D case for a flat foot in contact with the ground. Define a coordinate $\boldsymbol{\rho}$ to describe a position in the $sole$ of the foot. The ground reaction force at a given $\boldsymbol{\rho}$ is given by the force function $\boldsymbol{\rho}$ as drawn in Fig. 31-a. At the point $\varrho \in \boldsymbol{\rho}$, the reaction force field (or pressure distribution) along the whole $sole$, produces a resultant force

$$\boldsymbol{f}_{\varrho} = \int_{sole} \boldsymbol{f}(\rho)\mathrm{d}\rho \tag{4.2}$$

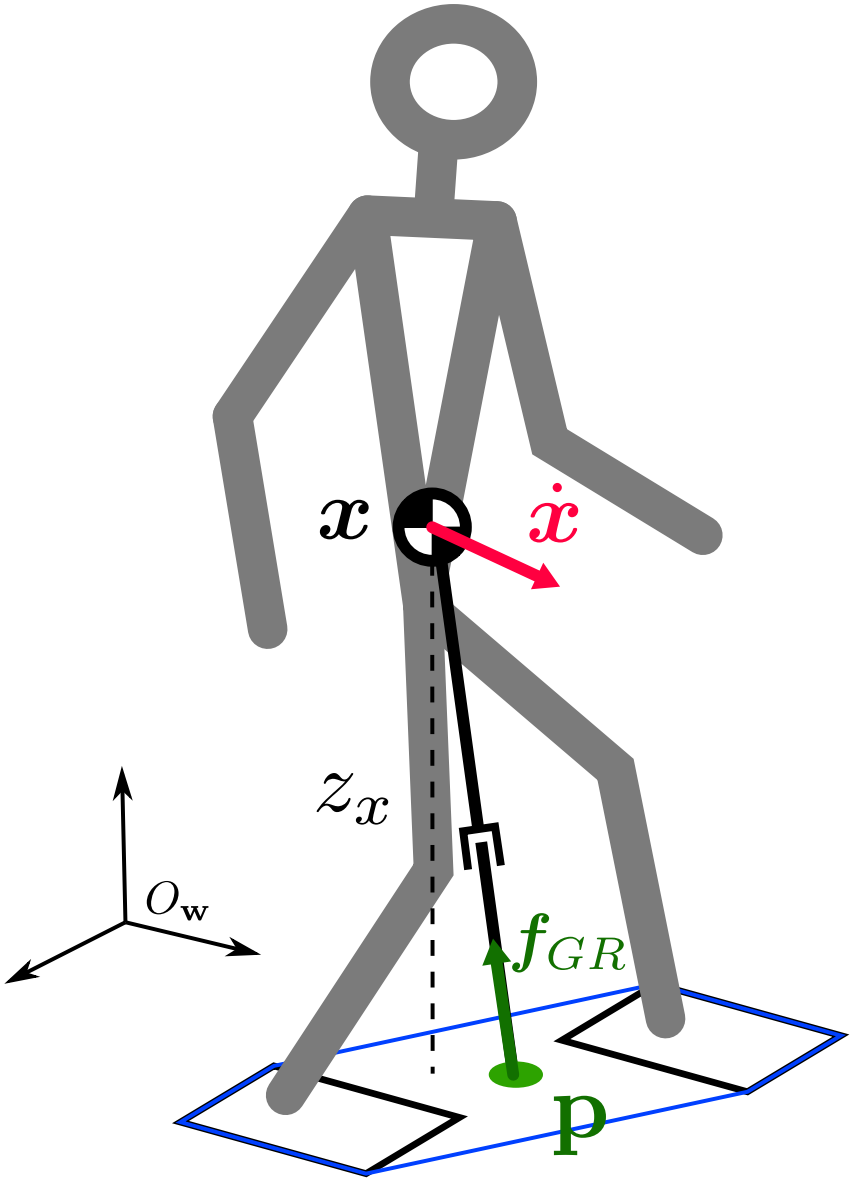

Figure 30 LIP (Linear Inverted Pendulum) representation of the walking dynamics. The CoM (Center of Mass) position in the world coordinate frame $O_{\mathbf{w}}$ is given by $\boldsymbol{x} \in \mathbb{R}^3$, and its velocity and acceleration are $\dot{\boldsymbol{x}} \in \mathbb{R}^3$, and $\ddot{\boldsymbol{x}} \in \mathbb{R}^3$ respectively. The pendulum's fulcrum is located on the ground on a point $\mathbf{p} \in \mathbb{R}^3$ such that the GRF $\boldsymbol{f}_{GR} \in \mathbb{R}^3$. The height of the CoM is kept constant at z_x.

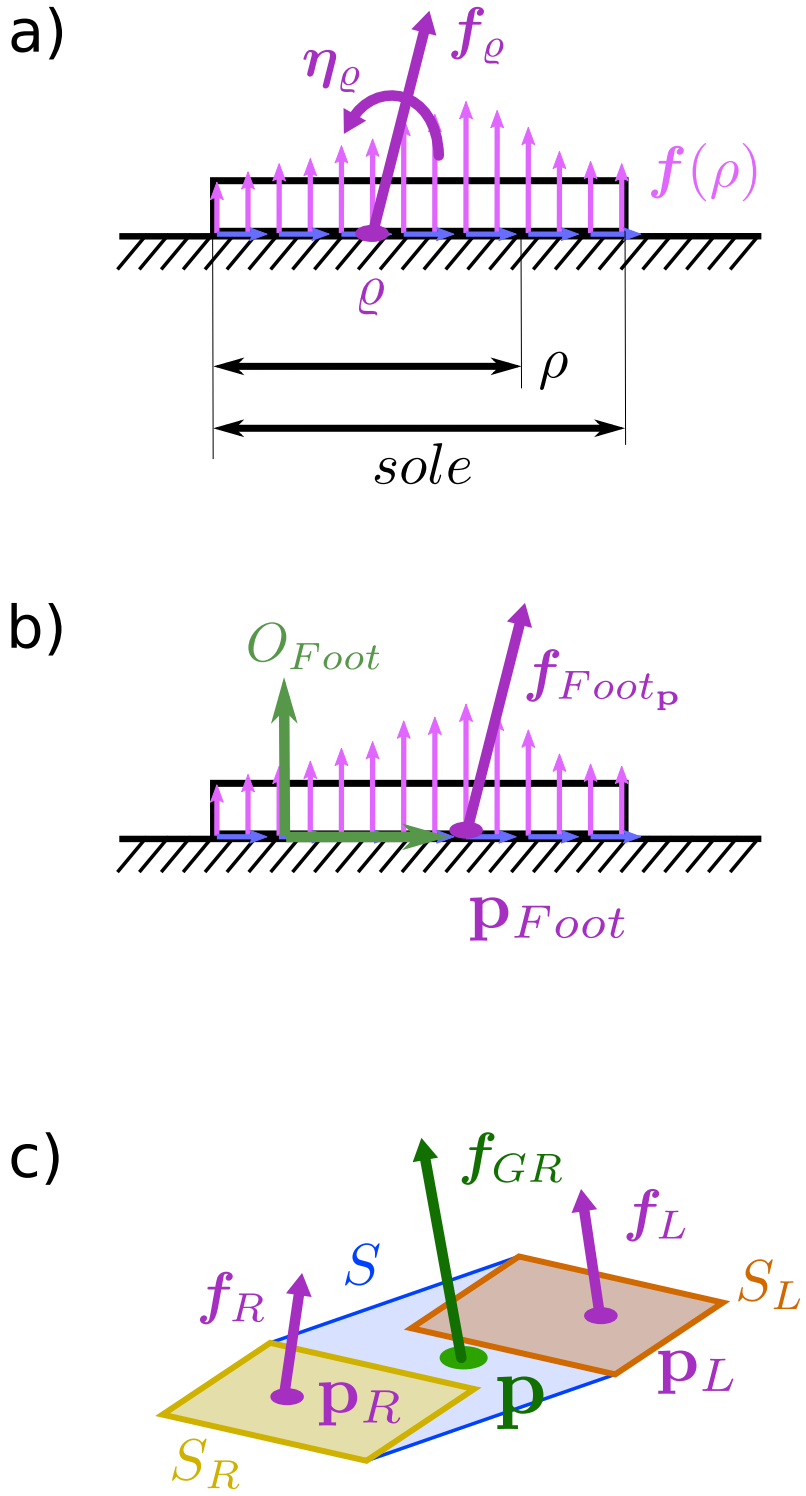

Figure 31 Definition of the ZMP. a) the pressure distribution of a foot in full contact with the ground. b) the GRF located at the point where the reaction torque is zero. c) the supporting polygon S is the convex hull enclosing the sets of contact points of the feet S_R and S_L.

and a resultant torque

$$\boldsymbol{\eta}_{\varrho} = \int_{sole} (\rho - \varrho)\boldsymbol{f}(\rho)\mathrm{d}\rho \tag{4.3}$$

From these expressions, it is clear that for an arbitrary pressure distribution of $\boldsymbol{f}(\boldsymbol{\rho})$, $\boldsymbol{f}_{\varrho}$ is kept constant at any point. Nevertheless, $\boldsymbol{\eta}_{\varrho}$ depends on ϱ and thus is different for every ϱ. The ZMP of the foot $\mathbf{p}_{Foot}$ is then defined as the point in the sole where $\boldsymbol{\eta}_{\varrho} = 0$ as shown in Fig. 31-b, and can be calculated as

$$\mathrm{p}_{Foot} = \frac{\int_{sole} \rho \boldsymbol{f}(\rho)\mathrm{d}\rho}{\int_{sole} \boldsymbol{f}(\rho)\mathrm{d}\rho} \tag{4.4}$$

The ZMP formulation can be extended to the 3D space by adding a second coordinate in the function of the pressure distribution as described in [12]. If we define a set of x-y coordinates to define a point in the sole, the reaction force is then given by $\boldsymbol{f}(x, y)$. Therefore, the ZMP is then extended to

$$\mathbf{p}_{Foot_x} = \frac{\int_{sole} x\boldsymbol{f}(x, y)\boldsymbol{d}sole}{\int_{sole} \boldsymbol{f}(x, y)\boldsymbol{d}sole} \tag{4.5}$$

$$\mathbf{p}_{Foot_y} = \frac{\int_{sole} y\boldsymbol{f}(x, y)\boldsymbol{d}sole}{\int_{sole} \boldsymbol{f}(x, y)\boldsymbol{d}sole} \tag{4.6}$$

Equations (4.5) and (4.6) describe the ZMP in a sole of a foot. The usual method to estimate this point is using the measurements of a force-torque sensor mounted in the ankle of the foot. However, for the case of the double support phases in the walking cycle, the ZMP must consider the interactions of both feet with the ground. Let us define the ZMP for the left and right foot as $\mathbf{p}_L = [\mathrm{p}_{L_x}, \mathrm{p}_{L_y}, 0]^\top$ and $\mathbf{p}_R = [\mathrm{p}_{R_x}, \mathrm{p}_{R_y}, 0]^\top$ respectively as drawn in Fig. 31-c. In the same way, $\boldsymbol{f}_L = [f_{L_x}, f_{L_y}, f_{L_z}]^\top$ and $\boldsymbol{f}_R = [f_{R_x}, f_{R_y}, f_{R_z}]^\top$ are the ground reaction forces of the left and right foot respectively. With this information, the ZMP of the whole system can be computed as

$$\mathrm{p}_x = \frac{\mathrm{p}_{R_x} f_{R_z} + \mathrm{p}_{L_x} f_{L_z}}{f_{R_z} + f_{L_z}} \tag{4.7}$$

$$\mathrm{p}_y = \frac{\mathrm{p}_{R_y} f_{R_z} + \mathrm{p}_{L_y} f_{L_z}}{f_{R_z} + f_{L_z}} \tag{4.8}$$

When the whole foot sole is in contact with the ground, the CoP is equivalent to the ZMP and can be located at any point of the sole. When the foot tilts over one of the borders of the sole, the CoP no longer has zero moment around the CoP and thus, ZMP does not exist. The set of points S_{sole} where the ZMP can exist is called support polygon and encloses all the contact points between one foot and the ground for the single support phases. On the other hand, for double support phases, the support polygon comprises all the points where the composed ZMP (Eq. (4.7) and (4.8)) can exist. In such a case, the support polygon is formed by the convex hull S that encloses S_L and S_R. Where S_L and S_R, are the supporting polygons of the left foot and the right foot respectively as drawn in Fig. 31-c.

The ZMP has served as a primary metric of postural stability for decades [97]. We can say that a foothold is stable as long as the ZMP exists in the supporting polygon and therefore, it serves as feedback for balance and walking control.

4.1.3. Divergent component of motion (DCM) and walking control

The LIP model describes the motion of the CoM of the robot. The ZMP and the support polygon provide metrics to assess the stability and the constraints to keep the model stable. Let us now review the formulation of the DCM and how it provides a framework to generate stable walking motions.

The DCM, originally named Capture Point, was introduced independently in [156] and [157] as a complementary metric to assess the stability of walking motion. Briefly, the DCM is the point on the ground where the fulcrum of the LIP model must be placed so that the CoM comes to a complete rest given a defined CoM velocity. For practicality in the formulation, the DCM is considered co-planar to the CoM. Therefore, for the LIP model in Eq. (4.1) the DCM $\boldsymbol{\xi} \in \mathbb{R}^3$ is defined as

$$\boldsymbol{\xi} = \boldsymbol{x} + \frac{\dot{\boldsymbol{x}}}{\omega} \tag{4.9}$$

Equation (4.9) describes the CoM's first order dynamics as

$$\dot{\boldsymbol{x}} = -\omega(\boldsymbol{x} - \boldsymbol{\xi}) \tag{4.10}$$

which is stable when $\omega > 0$. In other words, the DCM is a natural attractor point for the CoM. The first order dynamics of the DCM are

$$\dot{\boldsymbol{\xi}} = \dot{\boldsymbol{x}} + \frac{\ddot{\boldsymbol{x}}}{\omega} \tag{4.11}$$

which we can combine with Eq. (4.1) as

$$\dot{\boldsymbol{\xi}} = \omega(\boldsymbol{\xi} - \mathbf{p}) \tag{4.12}$$

which is unstable. However, we can use $\mathbf{p}$ as a control input to stabilize it. This structure is the core of the algorithm to generate walking motions proposed by [6]. Englsberger et al. develop a practical method to define walking primitives that exploit the stable dynamics of the CoM following a reference DCM. The method consist of 4 steps:

1. **Footstep plan:** The process starts with the definition of the footstep locations over the terrain. They can be defined by simple geometric rules or considering the geometry of the environment as in [158] and [159]. Regardless of the method used, the footsteps are a list of poses over the terrain used as reference positions and orientations for the feet. Let us define the footsteps as a set of transformations ${}^{\mathbf{w}}\mathbf{T}_i \in SO(3)$ composed by the rotation ${}^{\mathbf{w}}\mathbf{R}_i \in SE(3)$ and the translation ${}^{\mathbf{w}}\mathbf{r}_i$.

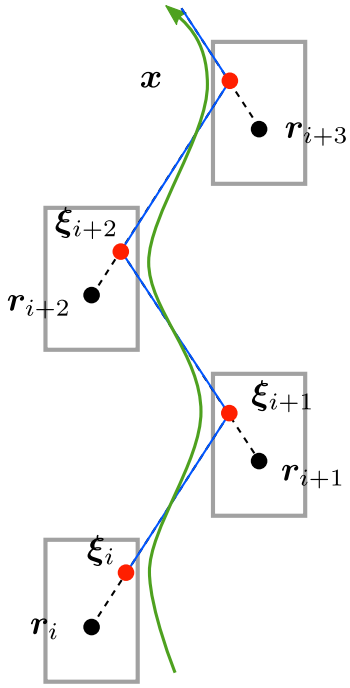

Figure 32 Walking motion generation from Englsberger et al. in [6]: 1) Define footstep positions. 2) Define VRP (Virtual Repellent Point) over the footsteps. 3) Compute the DCM waypoints between the VRPs. 4) Execute the plan evaluating the DCM and CoM dynamics.

2. **Virtual Repellent Point (VRP) plan:** Once defined the footstep locations, we can set virtual repellent points than will push away the DCM from where they are located. Therefore, by defining VRPs over the target foot locations as drawn in Fig 32, we can produce the reference trajectories for the DCM. Therefore, the i-th VRP is defined by

$$\boldsymbol{r}_i = {}^{\mathbf{w}}\mathbf{r}_i + \begin{bmatrix} 0 \\ 0 \\ z_x \end{bmatrix} \tag{4.13}$$

3. **DCM way point plan:** With the VRPs, we proceed to define waypoints evaluating the solution of Eq. (4.12) for a constant $\mathbf{p}$, and constant step time t_{step}. The i-th DCM waypoint is given by

$$\boldsymbol{\xi}_i = \boldsymbol{r}_{i+1} + e^{\omega t_{step}} \left(\boldsymbol{\xi}_{i+1} + \boldsymbol{r}_{i+1}\right) \tag{4.14}$$

4. **Generate CoM trajectory:** Once generated all the waypoints for the DCM, the reference trajectory for the DCM $\boldsymbol{\xi}_r$ is given by the solutions of Eq. (4.12) as

$$\boldsymbol{\xi}_r = \boldsymbol{r}_i + e^{\omega(t - t_{step})} \left(\boldsymbol{\xi}_i + \boldsymbol{r}_i\right) \tag{4.15}$$

where $t \in \mathbb{R}$ is the time. Then, the trajectory of the CoM is given by Eq. (4.10) which is smoothly following $\boldsymbol{\xi}_r$.

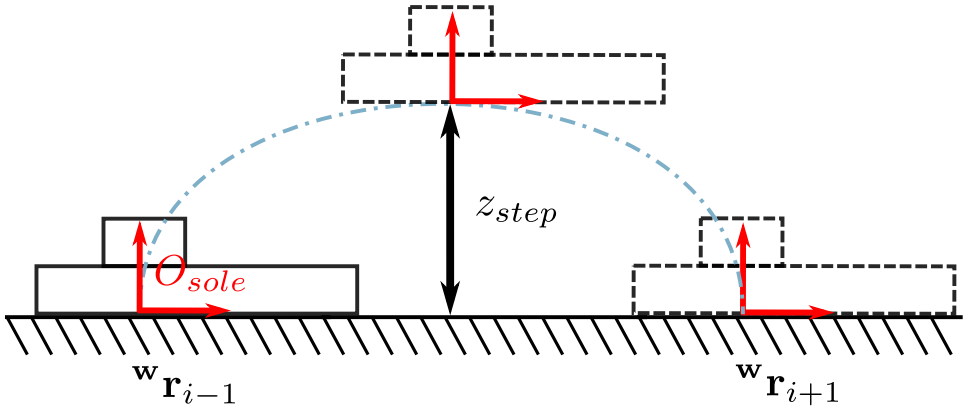

Figure 33 Kinematics of the foot swing motion during the single support phase. At the i-th step, the non supporting foot moves from ${}^{w}\mathbf{r}_{i-1}$ to ${}^{w}\mathbf{r}_{i+1}$ in a smooth spline that reaches z_{step} height.

These steps generate a smooth stable trajectory for the CoM over the footsteps. The only missing part of the walking reference motions is the swing motions of the legs during the single support phases. The step motions are coordinated within a step period t_{step}. This period is divided into the periods of the two phases t_{ss} for the single support, and t_{ds} for the double support, such that

$$t_{step} = t_{ss} + t_{ds} \tag{4.16}$$

Then, the foot motion must be generated within t_{ss} as drawn in Fig. 33. The most usual way to generate these motions is with constrained splines of third or higher-order, or with a series of interpolations as proposed in [160]. However, the start time of the splines must be precisely triggered by a walking state machine that coordinates the walking motions as in [161].

4.1.4. Balance control for bipedal walking

A robot can stably walk over perfectly flat terrain if it tracks the walking motions with perfect accuracy in an open loop. However, they are sensitive to external perturbations, motion tracking deviations, modeling inaccuracies, and irregularities in the terrain. Therefore, open-loop walking with the generated pattern is not feasible if any of these conditions appear. In reality, all of these issues are present and disturb the walking motions, thus we must somehow close the loop. To do so, we can make use of the structure of the DCM-CoM dynamics again. We can define stable closed loop dynamics for the DCM as

$$\dot{\boldsymbol{\xi}} - \dot{\boldsymbol{\xi}}_r = -k_\xi \left(\boldsymbol{\xi} - \boldsymbol{\xi}_r\right) \tag{4.17}$$

where $\boldsymbol{\xi}_r \in \mathbb{R}^3$ is the reference DCM trajectory defined by the algorithm in Section 4.1.3, $\dot{\boldsymbol{\xi}}_r \in \mathbb{R}^3$ its derivative, $\boldsymbol{\xi} \in \mathbb{R}^3$ is the actual DCM of the robot, $\dot{\boldsymbol{\xi}} \in \mathbb{R}^3$ its derivative, and $k_\xi > 0 \in \mathbb{R}$ is a proportional gain. Evaluating the left side with Eq. (4.12) for both the reference DCM $\dot{\boldsymbol{\xi}}_r = \omega(\boldsymbol{\xi}_r - \mathbf{p}_r)$ and actual DCM $\dot{\boldsymbol{\xi}} = \omega(\boldsymbol{\xi} - \mathbf{p}_d)$, we can define a control input from the ZMP position as

$$\mathbf{p}_d = \mathbf{p}_r - \left(1 + \frac{k_\xi}{\omega}\right)\left(\boldsymbol{\xi}_r - \boldsymbol{\xi}\right) \tag{4.18}$$

where $\mathbf{p}_d \in \mathbb{R}^3$ is an adjusted ZMP reference position, namely desired ZMP, that closes the loop for tracking the reference DCM. Nevertheless, we must close the loop on the CoM level to track $\mathbf{p}_d$ with the real ZMP. There are different methods for ZMP tracking as described in [12]. One simple example is by defining a stable closed loop dynamics, similar to Eq. (4.17) as

$$\dot{\mathbf{p}} - \dot{\mathbf{p}}_d = -k_p \left(\mathbf{p} - \mathbf{p}_d\right) \tag{4.19}$$

which we can derive and expand to an adjusted reference for the CoM as considering $\dot{\mathbf{p}}_d = \boldsymbol{x}_r - \frac{1}{\omega^2}\dddot{\boldsymbol{x}}_r$ with $\dddot{\boldsymbol{x}}_r = 0 \in \mathbb{R}^3$ a zero jerk reference trajectory for the CoM as

$$\dot{\boldsymbol{x}}_r = \dot{\mathbf{p}} + k_p(\mathbf{p} - \mathbf{p}_d) \tag{4.20}$$

which closes the loop commanding the velocity of the CoM using ZMP feedback.

4.2. Plantar Tactile Sensing for Biped Robots

As summarized in the previous section, walking controllers require the measurement and control of the reaction forces exerted by the robot's feet on the terrain. The classic approach is to include ankle force-torque sensors to have a direct measurement of the resultant wrench at the mounting point. With these sensors, a robot can estimate the significant metrics for balance and locomotion which are sufficient for walking over flat and uneven ground. However, in [162] and [56], we proposed plantar multi-modal robot skin to enhance the capabilities of biped robots to acquire more information on the foot-ground interactions which complement the ankle sensors to improve balance and locomotion control. In this section, the requirements and capabilities of plantar skin for biped robots will be revised, and the formulations to estimate the significant metrics needed for balance and locomotion.

4.2.1. Hardware for plantar sensing

Full-size humanoid robots are designed to work in human environments and to perform tasks with humans. Their mass can be larger than 100 kg and consequently, the weight of these robots can vary around 980 N without considering payloads. Also, biped walking consists of a succession of single and double support phases. Therefore, the skin sensor required for this application must be capable of holding around 980 N in the area of a foot and still sense variations in the contact pressure.

Due to the heavy load requirement, the suitable robot skins for full-size humanoid robot soles are the resistive matrix arrays [116, 117, 122] and the capacitive force cell [163]. Some of the skin technologies that have proved capable of resisting high pressure and still sense variations are the Tekscan pressure sensors [164] with pressures larger than 1 MPa, the flexible ROBOSKIN sensors [163] under pressures larger than 150 kPa, and the stretchable PsSi tactile sheet [165] under pressures larger than 150 kPa. Nevertheless, these tactile sensors only provide the pressure shape, and the geometrical mapping over the robot sole must be ob-

tained manually. Even more, they would require protective layers to prevent damage caused by harsh terrain textures.

The robot skin developed at our lab fulfills the load requirement [1]. Each skin taxel with a surface area of 6.9 cm^2 (Fig. 1) can hold more than 80 kg and still sense variations in the applied force (operating pressure $\approx$ 80 MPa). As described in Chapter 3, it provides four sensing modalities (force, proximity, acceleration, and temperature) over a uniform spatial distribution that can cover complex curved surfaces [166]. The complete tactile information can be delivered at a rate up to 250 Hz in large scale areas (covering not only the soles) due to new neuromorphic paradigms, such as the even-driven communication approach by Bergner et al. [167]. The robot skin also provides the position of every taxel on the sole [168] which can be used to reconstruct the pressure shape when the foot is on the ground in real-time.

The skin taxels are connected with the neighboring taxels conforming a dynamic network where the data packets are sent following optimal communication paths to reduce the latency [124]. This dynamic network configuration is valuable for the foot-sole application because the skin must reconfigure its communication channels in case of hardware damage. Therefore, if a heavy impact is produced between the terrain and the sole, and a taxel in the sole is damaged, the network reconfigures itself and continues transporting the data generated by the other taxels. Nevertheless, the construction of the taxels is resilient and can hold hard impacts without receiving damage. Additionally, following the biological principle of the sole skin in human feet, the external silicon layer was thickened for this special application to extend its lifespan. This silicon material shows a high friction coefficient over different surfaces which improves the stability of the steps, reducing the likelihood of slipping.

4.2.2. Mountable tactile shoes

New advances in skin technologies allow covering complex surfaces with tactile sensors without major modifications to the body parts. For example, the rubber-dome optical-based tactile sensors in [121] allowed covering the feet of a biped robot with an active toe joint. However, this mounting mechanism still requires a modification of the robot's feet, and the rubber domes' add a spring-damper layer between the foot and the ground. Another practical mounting mechanism for plantar sensors is the wireless sensitive shoes in [169]. These shoes encapsulate all the electronics and enable the measurement of the ZMP from force sensors. Mountable shoes can serve other purposes in addition to incorporating sensors. For example, the shoes in [170] provide energy storing elements for lateral motions that help reduce the energy consumption in the actuators.

Modularity in hardware and software increases the versatility of robotic platforms. By replacing simple elements, a robot can adapt to different applications, analogously to how we change clothes and shoes for different activities. For this thesis, two 42 taxel patches were created to cover the soles of the H1 robot as shown in 3. These patches are mounted on a

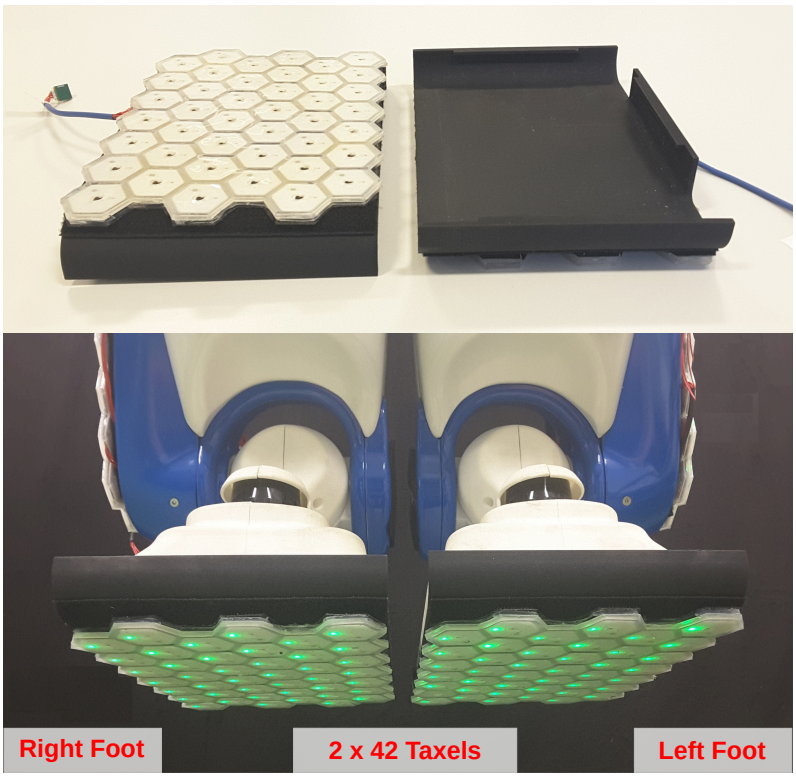

Figure 34 Skin patches mounted on the soles of the REEM-C robot. 42 taxels in each sole, mounted on 3D printed removable sole covers.

set of 3D printed removable sole covers which make it easy to mount and dismount without making permanent changes on the robot. This mounting mechanism can be easily adapted to different foot sizes and geometries by creating the mountable covers for the robot foot and the skin patches to cover the sole area. Furthermore, the same process was applied to mount 51 taxels on each sole of the HRP-2Kai robot. Plantar robot skin is mounted on both robots with the same apparatus as shown in Figures 3 and 5. The robot skin mounted on the shoes is the latest version of the tactile sensors developed at the Institute for Cognitive Systems [5].

4.2.3. Center of Pressure Estimation (CoP) from plantar information

There are different methods to locate the center of pressure of a robot's foothold with different foot and sensor designs [12]. For example, using an array of single-axis force sensors distributed on the sole. The normal force sensors in our robot skin fulfill that requirement. It covers the whole area of the sole with a uniform distribution of normal force sensors as shown in Fig. 34. Then, for a single sole, the position of the center of pressure is defined as

$$\mathbf{p}_x = \frac{\sum_{i=1}^{k} \mathbf{p}_{i_x} f i_z}{\sum_{i=1}^{k} f i_z}, \qquad \mathbf{p}_y = \frac{\sum_{i=1}^{k} \mathbf{p}_{i_y} f i_z}{\sum_{i=1}^{k} f i_z}, \tag{4.21}$$

where, for a group of k taxels mounted on a robot's sole, $\boldsymbol{f} j_z$ is the vertical ground reaction force measured by a taxel located at $\boldsymbol{r}_i$ with respect to the sole coordinate frame O_{sole} as shown in Fig. 35. We denote $\mathbf{p}$ as the computed CoP of the foot sole. Furthermore, the

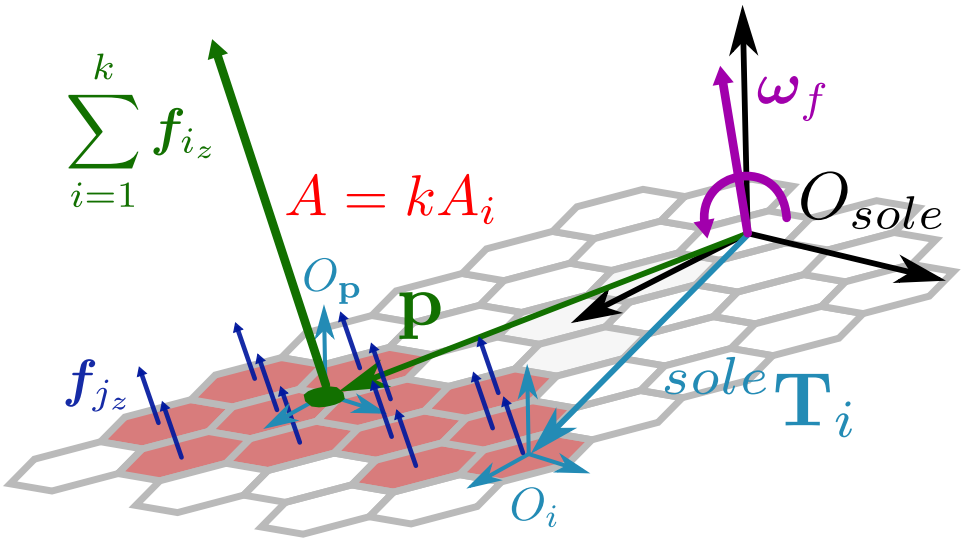

Figure 35 Computation of the CoP on the sole using the normal force sensors in the robot skin. $\boldsymbol{f}_i$ is the normal force measured by the $i-th$ taxel, $\mathbf{p}$ is the computed CoP position, and $^{sole}\mathbf{T}_i$ the homogeneous transformation from O_i to O_{sole}. As an example of additional information that can be generated with the robot skin, the contact area A is easily computed.

uniform spatial distribution and size of the taxels enables a fast computation of the contact area by counting the taxels that detect contact force over an activation threshold $||\boldsymbol{f}_{i_z}|| > \epsilon_f$. All the taxels that satisfy this condition are called *Active-Taxels*. Then, the contact area is

$$A = kA_{taxel}, \tag{4.22}$$

with $A_i \approx 691$ mm^2.

4.2.4. Ground reaction force (GRF) from plantar information

In a set of k taxels mounted on a sole with a coordinate frame $\boldsymbol{O}_{sole}$ located at the sole surface, the i-th taxel measures the contact force $\boldsymbol{f}_{f,i} = [f_{f,i,x}\ f_{f,i,y}\ f_{f,i,z}]^\top \in \mathbb{R}^3$ at its mounting coordinate frame $\boldsymbol{O}_i$. Assuming a spatially calibrated robot skin, the transformation $^{sole}\mathbf{T}_i$ from $\boldsymbol{O}_i$ to the sole coordinate frame $\boldsymbol{O}_{sole}$ is known and composed by the rotation $^{sole}\mathbf{R}_i \in SO(3)$ and the translation $^{sole}\boldsymbol{r}_i \in \mathbb{R}^3$. A graphic description of these parameters is drawn in Fig. 35.

Considering the contribution of all the taxels on the sole, the resultant GRW (Ground Reaction Wrench) at $\boldsymbol{O}_{sole}$ frame is calculated as

$$\boldsymbol{\omega}_f = \begin{bmatrix} \boldsymbol{f}_f \\ \\ \boldsymbol{\eta}_f \end{bmatrix} = \sum_{i=1}^{k} \begin{bmatrix} ^{sole}\mathbf{R}_i\, \boldsymbol{f}_{f,i} \\ \\ ^{sole}\mathbf{r}_i \times ^{sole}\mathbf{R}_i\, \boldsymbol{f}_{f,i} \end{bmatrix} \in \mathbb{R}^6, \tag{4.23}$$

where $\boldsymbol{f}_f = [f_{f,x}\ f_{f,y}\ f_{f,z}]^\top$ is the GRF, and $\boldsymbol{\eta}_f = [\eta_{f,x}\ \eta_{f,y}\ \eta_{f,z}]^\top$ the sole reaction torque, both in $\boldsymbol{O}_{sole}$ coordinate frame. This is equivalent as the measurement of a 6D force-torque

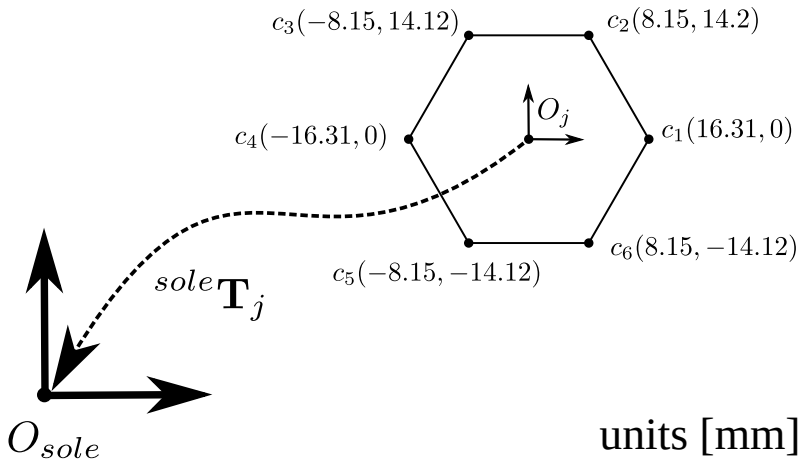

Figure 36 The Corner points of the taxel are used to populate a cluster which later is used to find the smallest convex hull as supporting polygon. This example is using the geometry of the hexagonal taxels in the robot skin designed at ICS [7].

sensor mounted at $\boldsymbol{O}_{sole}$. Let us define a coordinate frame parallel to O_{sole} but located at the CoP $O_{\mathbf{p}}$ as drawn in Fig. 35. Transforming $\boldsymbol{\eta}_f$ from O_{sole} to $O_{\mathbf{p}}$ yields to $\boldsymbol{f}_{\mathbf{p}} = \boldsymbol{f}_f$, and $\boldsymbol{\eta}_{\mathbf{p},x} = \boldsymbol{\eta}_{\mathbf{p},y} = 0 \in \mathbb{R}$ which is the GRF with zero moment according to Vukobratović [155].

4.2.5. Supporting Polygon Acquisition from plantar information

The extra information the robot skin provides enables the direct acquisition of important balance-stability metrics such as the supporting polygon. As depicted in Fig. 37 the construction of the supporting polygon from skin information starts by finding the active taxel (Fig. 37-b). Then, for every active taxel in the sole, the set of corner points $S_c = [c_1\, c_2\, ...\, c_6]$ of the hexagonal taxel are transformed to the sole frame O_{sole} as shown in Fig. 36 and added to a cluster set (Fig. 37-c)

$$S_{sole} = \Big|\Big|_{j=1}^{k} {}^{sole}\mathbf{T}_j S_c, \tag{4.24}$$

where ${}^{sole}\mathbf{T}_j$ is the homogeneous transformation from taxel frame O_j to the sole frame O_{sole}. Finally, the cluster of contact points on the sole S_{sole} can be used to find the smallest convex hull wrapping S_{sole} using algorithms such as [171] (Fig. 37-d). It is also possible to find concave hulls describing the shape of the ground contact areas with algorithms such as [172].

For double support, the point clusters of each sole S_L and S_R can be transformed to world coordinates and concatenated (Fig. 37-f)

$$S_{feet} =^{\mathbf{w}} \mathbf{T}_L S_L \,\|^{\mathbf{w}}\, \mathbf{T}_R S_R \tag{4.25}$$

with ${}^{\mathbf{w}}\mathbf{T}_L$ and ${}^{\mathbf{w}}\mathbf{T}_R$ being the transformation from the left sole frame O_L and right sole frame O_R to world frame $O_{\mathbf{w}}$ respectively. And then, find the convex hull wrapping S_{feet} which generate the double support supporting polygon (Fig. 37-g).

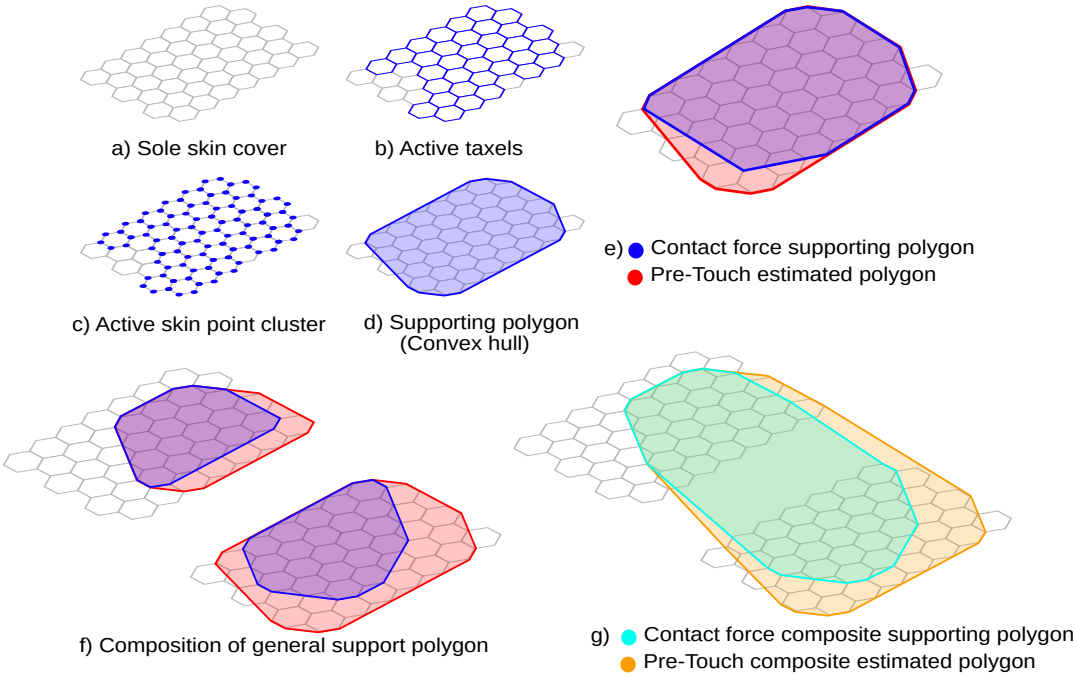

Figure 37 Supporting polygon acquisition. a) The spatial distribution of the robot skin over the sole. b) Detection of active taxels where $f_{jz} > \epsilon_f$. c) Active taxels point cluster. d) Convex hull obtained from the point cluster. e) Two polygons obtained from different sensing modalities: contact force and pre-touch. f) Polygons of both feet. g) Composite supporting polygon and pretouch polygon (convex hull from feet polygons).

The accuracy of S_{feet} is inversely proportional to the size of the taxels. However, for control purposes, a simplified convex polygon can be constructed from the initial approximation using iterative algorithms. For example, [173] finds the maximum area triangle inscribed in a convex polygon, [174] finds the maximum area parallelogram in a convex polygon, and [175] finds the minimal area enclosing parallelogram containing a convex polygon.

This procedure can be applied to other sensing modalities to obtain the temperature footprint of a sole or the pre-touch modality to find a preemptive shape of the supporting polygon from a few centimeters before the foot landing (Fig. 37-e). This information is useful to create preemptive controllers for robust walking over unknown terrain.

4.2.6. Preemptive ground reaction wrench (PGRW) from plantar proximity sensors

Human feet are flexible structures of bones, joints, muscles, and soft tissues that let us stand upright and perform activities like walking, running, and jumping. Its complex anatomy allows the feet to find the best suitable foothold while walking by relaxing the ankle muscles and letting them adapt to the terrain. This mechanism also bears the high loads and impacts of biped walking while providing tactile and proprioceptive feedback on the interactions.

New actuator technologies are being developed to mimic the flexibility of human muscles showing promising results as summarized in [176]. However, these complex mechanical designs increase the cost of the construction and the difficulty of servo control. To simplify

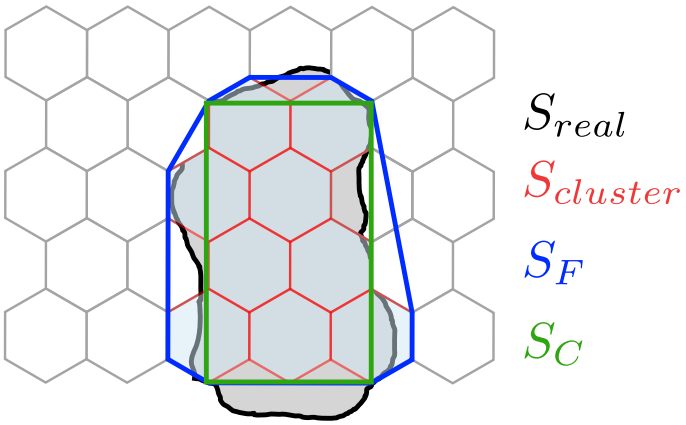

Figure 38 Supporting polygon constructed from tactile information. The real contact geometry S_{real} can be approximated from the known taxel geometry and measured forces $\boldsymbol{f}_i$. First, a cluster $S_{cluster}$ with the points of the contour of the contact area is created. Then, the convex hull of $S_{cluster}$ approximates the physical supporting polygon S_F. This information can be used to define contact constraints as the quadrilateral S_C which can be used on force distribution optimization methods.

the design and lower the costs, the legs and feet of several biped robots are built with stiff actuated joints that are not back-drivable nor soft as summarized in [177].

To alleviate this problem, plantar proximity sensing has been proposed in [178] for a small size robot. Plantar proximity sensing enabled preemptive ankle motion planing for walking on uneven terrain even with a coarse sensor distribution. Furthermore, if every taxel on the foot sole provides proximity-to-ground sensing within a suitable range, a virtual preemptive GRW can be computed using the virtual interaction formulation from proximity sensing in Section 3.3.1. This scenario is depicted in Fig. 39-a, where every taxel on the sole measures the distance to the ground. Most of low-cost commercial sensors deliver a numeric value inversely proportional to the detected distance $\rho_i = d_{range} - d_i$, where d_{range} is the maximum range of the sensor and d_i the actual distance.

Let us define a virtual ground repellent force inversely proportional to the distance between the taxel and the ground within its sensing range $\boldsymbol{f}_{p,i} = [0\ 0\ k_p\rho_i]^\top \in \mathbb{R}^3$ (see Fig. 39-a). The magnitude of the repulsive field can be adjusted with $k_p \in \mathbb{R}$ according to the needs of the walking motion. Analogously to the case of force sensing skin, for k taxels on the sole, the *Virtual Ground Reaction Wrench* (VGRG) is calculated as

$$\boldsymbol{w}_p = \begin{bmatrix} \boldsymbol{f}_p \\ \boldsymbol{\eta}_p \end{bmatrix} = \sum_{i=1}^{k} \begin{bmatrix} {}^{sole}\mathbf{R}_{p_i}\boldsymbol{f}_{p_i} \\ {}^{sole}\mathbf{r}_{p_i} \times {}^{sole}\mathbf{R}_{p_i}\boldsymbol{f}_{p_i} \end{bmatrix} \tag{4.26}$$

The components of $\boldsymbol{w}_p$ serve two purposes that will be expanded in the following sections: $\boldsymbol{f}_p$ helps detect premature contacts and damp the foot motion to reduce the landing impact. $\boldsymbol{\eta}_p$ helps adapt the foot orientation to the terrain geometry to find a larger contact area at foot landing.

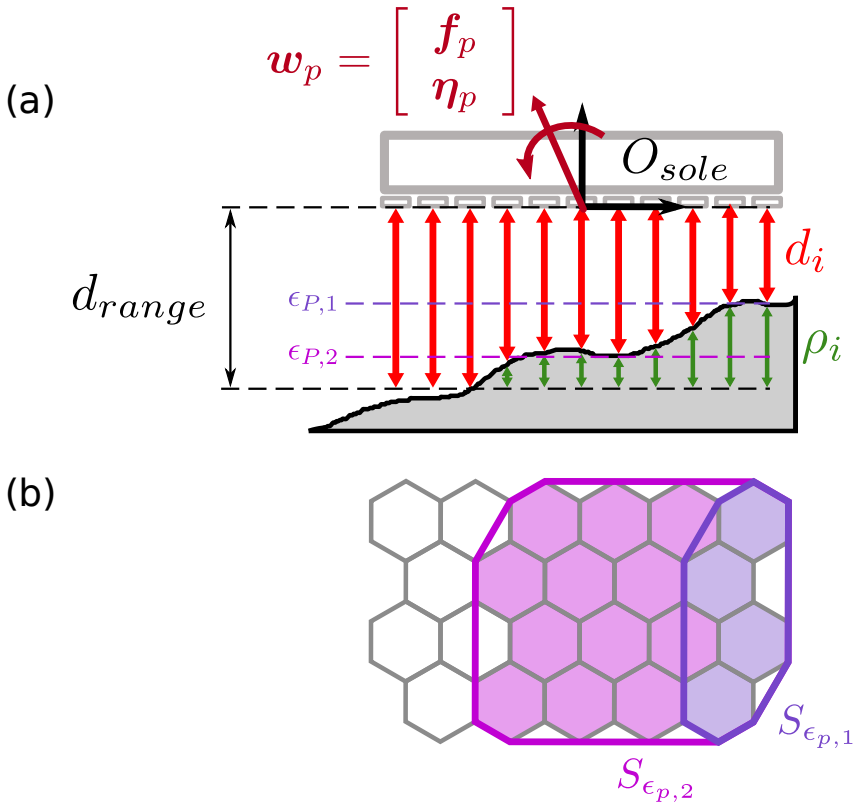

Figure 39 A sole covered with proximity sensing taxels. A proximity sensor provides the distance d_i from the taxel to the ground within the sensing range ρ_r. The proximity measurements can be used to generate height contours S_{ϵ_p} for the areas where $d_i > \epsilon_p$.

4.2.7. Preemptive supporting polygon from plantar proximity sensors

Analogous to the supporting polygon construction from contact information, a preemptive shape of such polygon can be constructed from the proximity information. In robot skins with proximity sensing on every taxel, a convex polygon S_p can be acquired from the convex hull enclosing the contours of all the taxels where the measured distance exceeds a certain threshold $d_i > \epsilon_p$. Furthermore, as the example depicted in Fig. 39-b, different height contours can be constructed defining different thresholds to approximate the ground geometry during the single support phases of walking.

4.3. Balance and Walking With Full Sole Contacts Using Plantar Tactile Feedback

In this section, the methods described above are experimentally evaluated. The results obtained using robot skin are compared to similar methods using ankle force-torque sensors. The controllers were implemented on the H1 robot with the skin sole covers shown in Fig. 34[1].

[1] The results in this section were presented in the 2018 IEEE-RAS 18th International Conference on Humanoid Robots (Humanoids 2018) [162] and a Journal article [56].

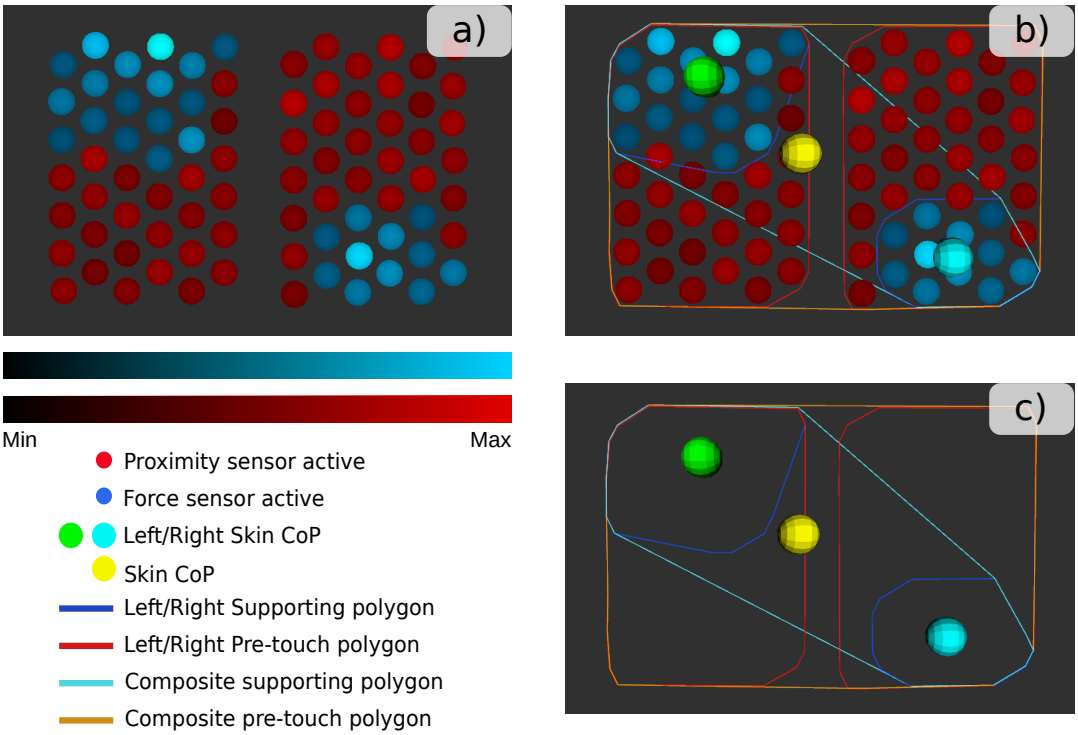

Figure 40 Snapshots of the sensor data from the robot skin in ROS-Rviz. a) Raw sensor data from Force sensors and pre-touch sensors. b) Computation of local and global CoP, supporting polygon and pre-touch polygon. c) Final representation of the Left and Right CoP, the general CoP, the supporting polygons and pre-touch polygons.

The measurement of the CoP and the reconstruction of the supporting polygon from raw skin data are shown in Fig. 40. First, we identify the active-taxels as shown in Fig 40-a. The taxels where the pre-touch sensor is active are marked in red and the taxels which detect contact force are marked in blue. With the active-taxels data, as shown in Fig. 40-b, we compute the CoP of each foot with the method described in Section 4.2.5. With this data information, as shown in Fig. 40-c, we can also construct the supporting polygon and the pre-touch polygon for each foot using the method described in Section 4.2.7. Finally, we combine the feet's polygons to construct the composite supporting polygon and the composite pre-touch polygon as described in Section 4.2.7.

In the following subsections, the skin measurements are used as tactile feedback in a balance controller and to re-plan steps when an obstacle is detected under the foot during walking.

4.3.1. Experiment: Tactile-based ZMP feedback in a balance controller

The online acquisition of the CoP can be used to compute the ZMP feedback for stable balance controllers and dynamically balanced walking controllers [97]. To assess the performance of the skin ZMP acquisition, a bench test was implemented comparing the ZMP position estimated by both the robot skin and ankle force-torque sensors in a balance con-

troller. The feedback law used for this test is the 2D DCM-ZMP regulator controller [179].

$$\boldsymbol{\xi} = \boldsymbol{x} + \frac{\dot{\boldsymbol{x}}}{\omega} \tag{4.27}$$

$$\mathbf{p}_d = \mathbf{p}_r - \left(1 + \frac{k_\xi}{\omega}\right)(\boldsymbol{\xi}_r - \boldsymbol{\xi}) \tag{4.28}$$

$$\dot{\boldsymbol{x}}_d = k_f\,(\mathbf{p} - \mathbf{p}_d) + k_{\boldsymbol{x}}(\boldsymbol{x}_d - \boldsymbol{x}) \tag{4.29}$$

where $\omega = \sqrt{\frac{g}{z_x}} \in \mathbb{R}$ is the inverted pendulum frequency at CoM height z_x, $\mathbf{p} \in \mathbb{R}^3$ and $\dot{\mathbf{p}} \in \mathbb{R}^3$ are the real and desired ZMP, $\boldsymbol{\xi} \in \mathbb{R}^2$ and $\boldsymbol{\xi}_r \in \mathbb{R}^2$ are the real and reference DCM, $\boldsymbol{x} \in \mathbb{R}^3$ and $\boldsymbol{x}_d \in \mathbb{R}^3$ are the real and desired CoM positions and k_ξ, k_f and $k_{\boldsymbol{x}}$ are positive gains. The controller was designed to be compliant to external pushing forces and return to a standing position afterwards. The parameters are listed in Table 2.

Table 2 Balance control parameters.

Parameter	Value
ξ_r	$0 \in \mathbb{R}^3$ [m]
$\boldsymbol{x}_d$	$0 \in \mathbb{R}^3$ [m]
z_x	0.8 [m]
$k_{\boldsymbol{\xi}}$	1.5
k_f	0.5
$k_{\boldsymbol{x}}$	1.0
ϵ_f	0.15 [kg]

The robot was standing on both legs keeping balance and was pushed and pulled by an operator to introduce unknown disturbances on the controller as shown in Fig. 41. The plots in Fig. 42-a,e and 42-c,f show the estimated ZMP *x* and *y* components used directly as feedback in the balance controller (assuming both soles are in full contact with the ground). In these plots, a comparison of the ZMP measured by the ankle force-torque sensors and the robot skin is presented. The difference in the estimation of the ZMP between the force-torque sensor and the robot skin $\mathbf{p}_{FT} - \mathbf{p}_{skin}$ is shown in Fig. 42-b,g and 42-d,h. The plots in Fig. 43 show the comparison of the estimated ZMP with the force-torque sensors and the skin in the xy plane. Fig. 43-a shows the local ZMP in each foot and the supporting polygon detected for each foot. Fig. 43-b shows the composite ZMP and supporting polygon.

As a comparison, the experiment was conducted under two conditions, first using the skin measured ZMP as feedback in the balance controller and then using the ZMP estimated with the ankle force-torque sensors. In both cases, the gains of the balance controller were the same. The operator pushed and pulled the robot from the neck to induce compliant motions in the robot body. When the external force was removed, the robot came back to the desired

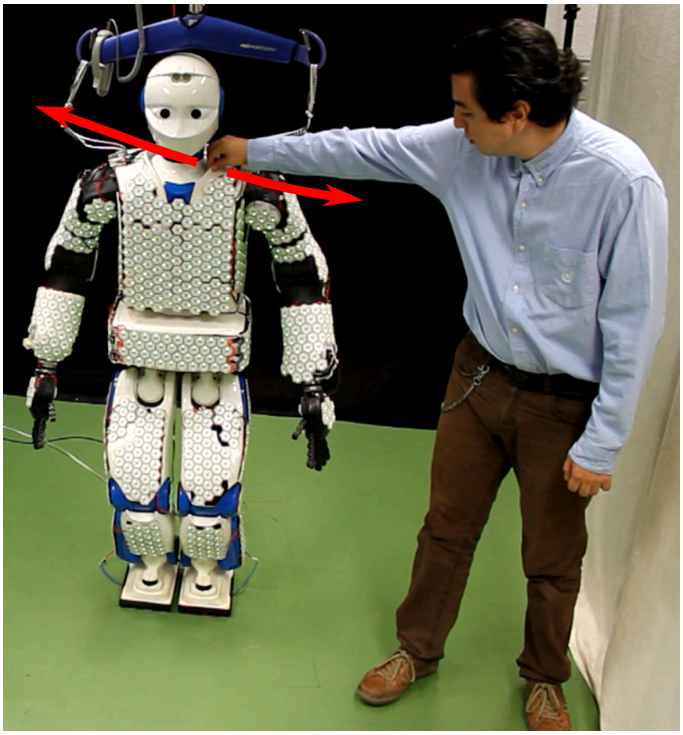

Figure 41 An experimental test of the ZMP estimation using robot skin. The robot is standing executing a CoM-ZMP compliant balance controller and an operator is pushing the upper body to disturb its balance. The ZMP used in the feedback loop was estimated using the robot skin.

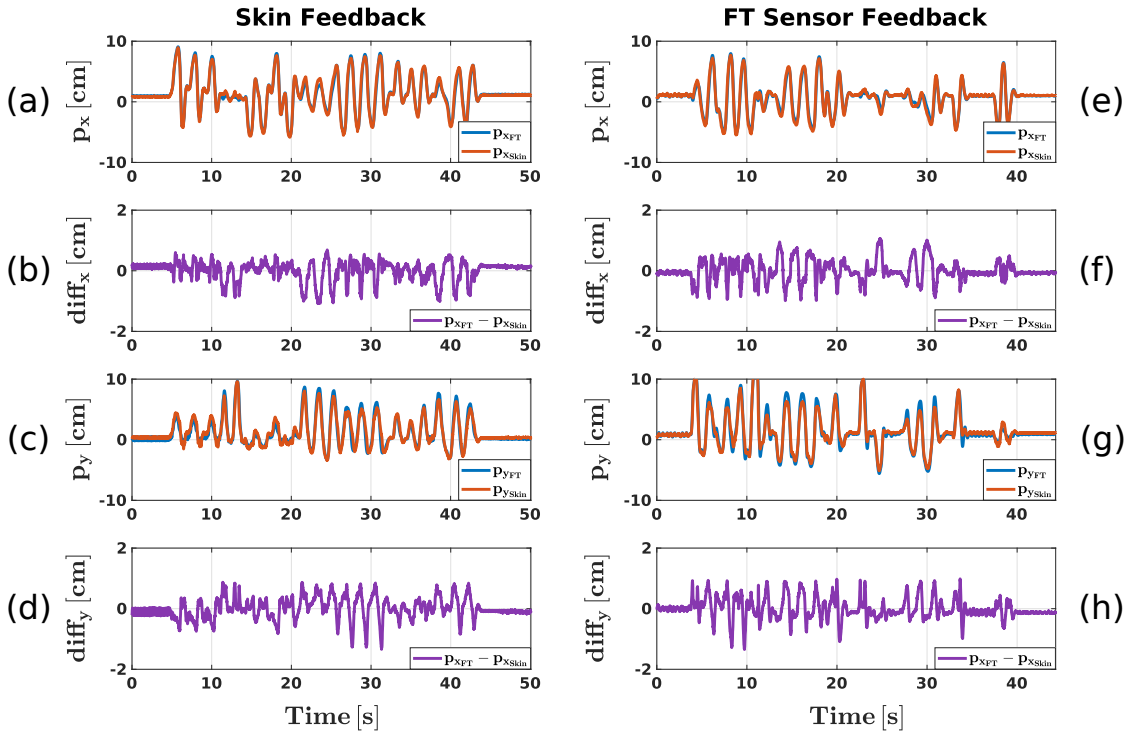

Figure 42 Data plot of the balance experimental test (Fig. 41). The ZMP was estimated using two different sensors: the robot's ankle force-torque sensors (blue), and the robot skin on the sole (red). The experiment was recorded twice, first using the skin ZMP as feedback in the balance controller and then, using the force-torque sensor ZMP. a,e) x component of the ZMP. b,f) difference between the force-torque sensor and robot skin ZMP x component. c,g) y component of the ZMP. d,h) difference between the force-torque sensor and the robot skin ZMP y component.

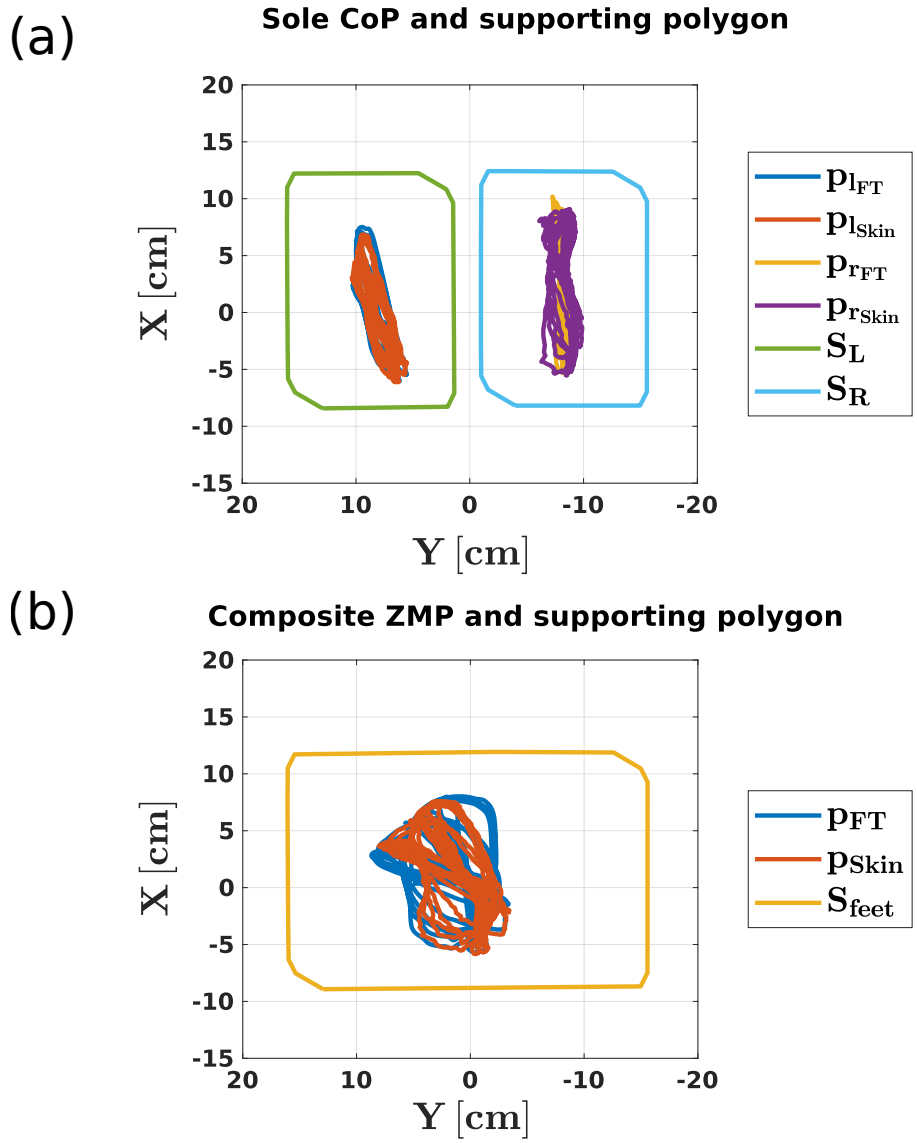

Figure 43 2D Data plot of the CoP experimental test shown in Fig. 41. a) Single sole force-torque sensor DCM (left $\mathbf{p}_{l_{FT}}$ and right $\mathbf{p}_{r_{FT}}$), skin DCM (left $\mathbf{p}_{l_{skin}}$ and right $\mathbf{p}_{r_{skin}}$), and supporting polygon (left S_L and right S_R). b) Composite force-torque sensor DCM $\mathbf{p}_{FT}$, skin DCM $\mathbf{p}_{Skin}$, and the composite supporting polygon S_{feet}.

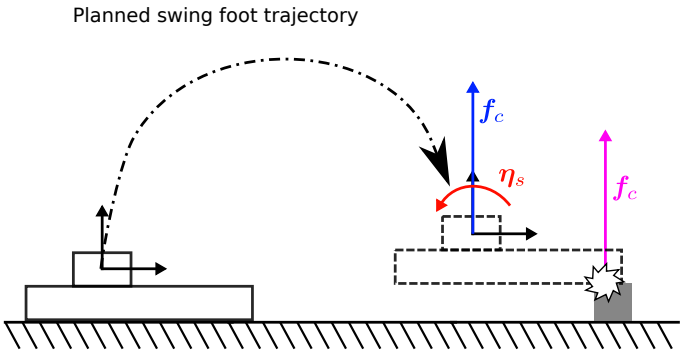

Figure 44 The trajectory of the swing foot during the experiment. When a premature contact is detected, the forces and moments in the ankle are measured by the force-torque sensor to evaluate if the obstacle is safe to step on it.

ZMP position located at the center of the supporting polygon. During the experiment, the ZMP was deviated up to 10 cm from the reference (located at 0 cm) by the external forces. However, it never reached the supporting polygon border to prevent breaking the full-sole contact assumption. The most considerable difference between the ZMP estimation from the force-torque sensor and the skin was approximately 1 cm and, although the magnitude of the disturbances was unknown, the balance controller showed a stable behavior in both cases.

4.3.2. Experiment: Steps re-planning from instantaneous contact information

This experiment is designed to examine the advantages the plantar robot skin has over the ankle force-torque sensors for footstep re-planning over unknown terrain. The robot is intended to walk on a straight line without knowing the geometry of the terrain. The walking controller is designed for flat terrain and does not consider ankle compliance. If an early contact occurs during the swing-leg phase (Fig. 44), the feasibility of stepping on the detected obstacle is evaluated with a simple rule which only uses the information acquired during the impact. If the obstacle is considered as stable, the robot continues walking over it following the planned footsteps. If the obstacle is considered as not safe, the footstep is re-planed to circumvent the obstacle and the robot continues walking as shown in Fig. 45. To check the step feasibility, the following rules are designed with the different sensors:

a) With the force-torque sensors, the moment produced at the ankle by the collision $\boldsymbol{\eta}_s$ (Fig. 44) is compared to a feasibility threshold of ϵ_t. This was defined under the assumption that the impact of a flat foot over flat terrain produces only vertical force. Therefore if $||\boldsymbol{\eta}_s|| \geq \epsilon_t$ the step must be re-planed.

b) With the robot skin, the relation $\dfrac{A_p}{A_s}$ is compared to a feasibility threshold of ϵ_A where A_p is the area of the supporting polygon detected at the moment of the impact, and A_s is the total foot sole area (measured directly from the robot's foot). This rule was designed under the assumption that a safe foothold must cover at least a certain percentage of the sole area to provide enough surface to generate enough friction for stepping on it. Therefore if $\dfrac{A_p}{A_s} \leq \epsilon_A$ the step must be re-planed.

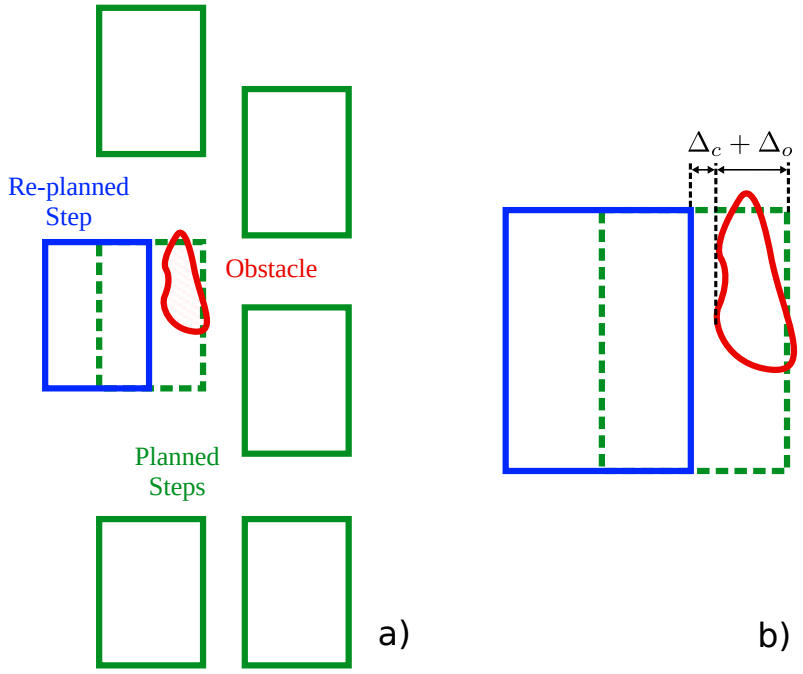

Figure 45 Walking on unknown terrain experiment. a) If a foothold is not safe to step onto it, the robot must re-plan to sidestep the detected obstacle. b) The re-planed step must consider the size of the obstacle Δ_o and a clearance distance Δ_c .

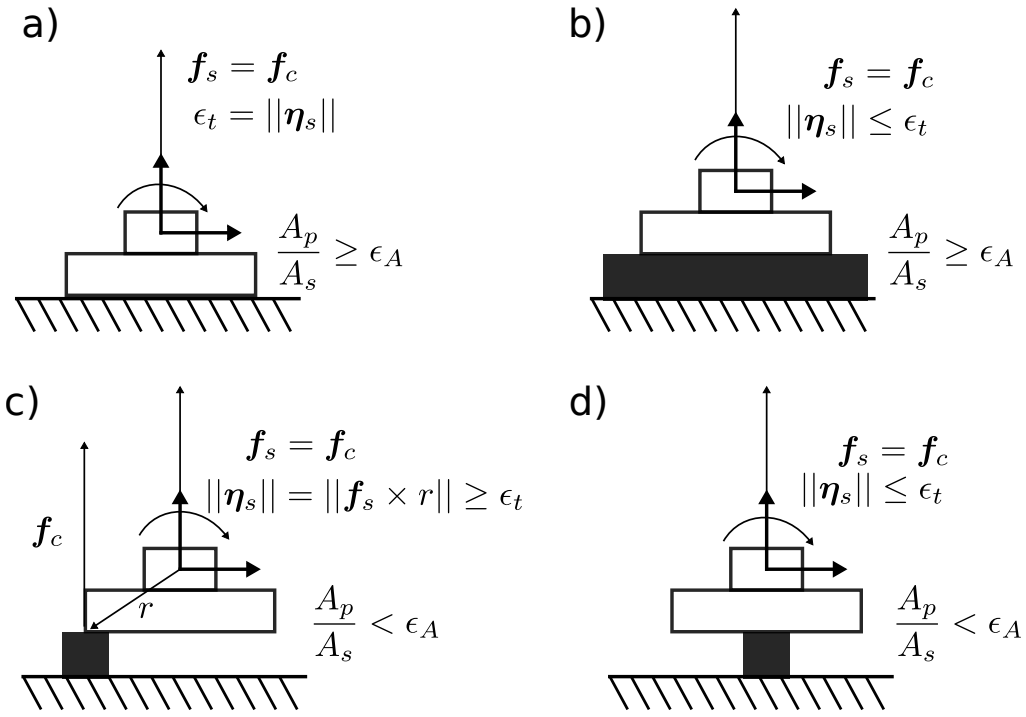

Figure 46 Different conditions for step feasibility evaluation. a) With no obstacle, both feasibility rules result in no re-plan. b) With a big flat obstacle, both feasibility rules result in no re-plan. c) With a small flat obstacle hit with the border of the sole, both feasibility rules trigger a step re-plan. d) With a small flat obstacle hit with the center of the sole, just below the force-torque sensor, the force-torque sensor rule does not trigger the re-plan, while the robot skin detects the unsafe condition and triggers the re-plan.

Both rules are analogous. However, the force-torque sensor cannot directly measure the contact area. Thus, it cannot be used for rule *b* while the plantar robot skin can be used for both. This is one major advantage of having more information about the ground contacts.

The conditions for step re-plan are represented in Fig. 46. For the cases where the contact provides a large flat surface, both rules *a* and *b* result in no re-plan Fig. 46-a and 46-b . If the contact is produced by a small flat obstacle Fig. 46-c, both rules trigger a step re-plan. All these conditions are correctly evaluated by both, the force-torque sensors and the robot skin. Nevertheless, when premature contact generates a moment, which is not large enough, the force-torque sensor fails to detect small surfaces and considers them as similar to a large area flat obstacle Fig. 46-b. For example, when a small flat obstacle is touched with the sole right below the force-torque sensor Fig. 46-d. On the other hand, the robot skin can measure the small obstacle area and trigger a step re-plan.

Right after the first contact, the robot skin can additionally provide the exact distance to sidestep an obstacle. We can obtain the obstacle's width Δ_o from the bounding box of the supporting polygon and the clearance distance Δ_c from the geometry of the foot sole. With this information, we can easily re-plan the step as shown in Fig. 45-b.

Fig. 47 shows the experimental comparison for an obstacle in the form shown in Fig. 46-d. The force-torque sensor fails to detect the unsafe foothold and the walking controller tries to step onto the obstacle causing the robot to fall. The robot skin detects correctly the unsafe obstacle and triggers the step re-plan with the exact distance to sidestep the obstacle and continues walking.

The walking test was performed under eight different conditions using four different obstacles as shown in Table 2. For each obstacle, the test was run once using only the force-torque sensor and once using only the robot skin. The thresholds for the feasibility check rules are ϵ_t for the force-torque sensor and ϵ_A for the contact area. The force-torque sensor failed with obstacles 3 and 4 which provide a small flat area that was assumed to be large enough to support the robot. Obstacle 4 is made with 3 small spheres which are providing round surfaces similar to stepping on pebbles. This three-point contact condition is not detectable by the force-torque sensor without exploratory motions.

4.4. Walking on Uneven Terrain and Partial Footholds

In Section 4.3, we probed how plantar skin complements balance and walking controllers to prevent stepping over insecure terrain conditions. In this section, the tactile information will be used to extend the formulations of balance and walking controllers to walk over uneven terrain and partial footholds.

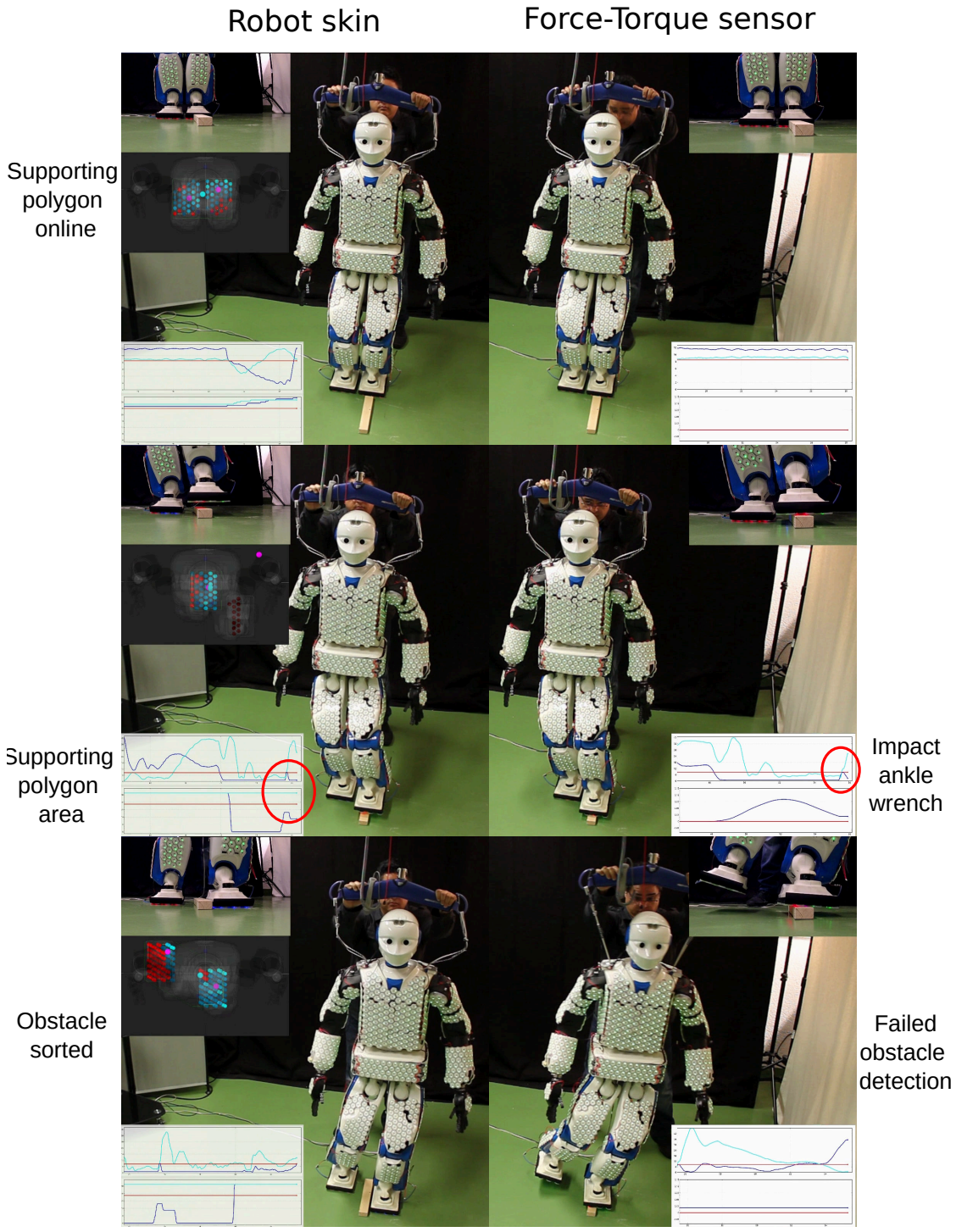

Figure 47 Experimental evaluation of the step feasibility rules using force-torque sensors and robot skin. On the left side, the robot skin successfully detects the small area of the obstacle and triggers a step re-plan with the exact distance required to sidestep the obstacle. On the right side, the force-torque sensor fails to detect the unsafe condition and the walking controller tries to step on the obstacle leading the robot to fall.

Table 3 Tested obstacles. Green: Robot completed the test. Red: Robot fell down.

No.	Obstacle	Footprint	$\boldsymbol{\eta}_s[Nm]$ $\epsilon_t = 8.0$	A_p/A_s $\epsilon_A = 0.8$	Handled by force-torque sensor	Handled by robot skin
1		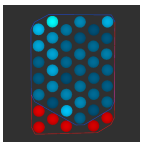	6.5	0.85	Stepping on obstacle	Stepping on obstacle
2		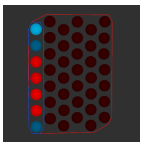	8.6	0.16	Footstep re-plan	Footstep re-plan
3		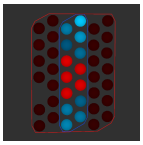	6.0	0.33	Stepping on obstacle	Footstep re-plan
4		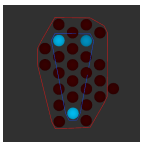	4.5	0.23	Stepping on obstacle	Footstep re-plan

4.4.1. Preemptive foot compliance (PFC) using plantar proximity sensors

A common strategy for bipedal robot walking on uneven terrain using ankle force-torque sensors is to generate compliant joint motions from the GRW to distribute the contact forces along the sole [86, 180, 85, 181, 93]. This approach is briefly depicted in Fig. 48. During the swing phase of walking, the foot can encounter an unexpected early contact caused by a terrain irregularity or an obstacle. During the swing phase of walking, the foot can encounter an unexpected early contact caused by a terrain irregularity or an obstacle. This event produces an impact which is measured by the ankle sensor as a spike in the force $\boldsymbol{f}_{ankle} \in \mathbb{R}^3$ and torque $\boldsymbol{\eta}_{ankle} \in \mathbb{R}^3$.

The swing foot motion is canceled when early contact is detected, for instance, when the ankle force exceeds a predefined threshold $||\boldsymbol{f}_{ankle}|| > \epsilon_{stop}$. However, this method causes heavy impacts on highly dynamic walking motions. In [182], the impacts are reduced by adding contact switches on the corners of the foot. However, for irregular terrain (as in the case of a small size obstacle), the switches at the corners of the sole can miss the early contact, leading to an impact in the foot.

When the terrain is irregular, $||\boldsymbol{\eta}_{ankle}||$ is larger than in the flat terrain case, and thus, the ZMP is pushed away from the sole center. Such disturbance can be compensated by distributing the contact forces along the sole. The force distribution can be realized by changing the foot orientation with a foot impedance controller as in [180], and [93] or as an optimization problem as in [183], and [8].

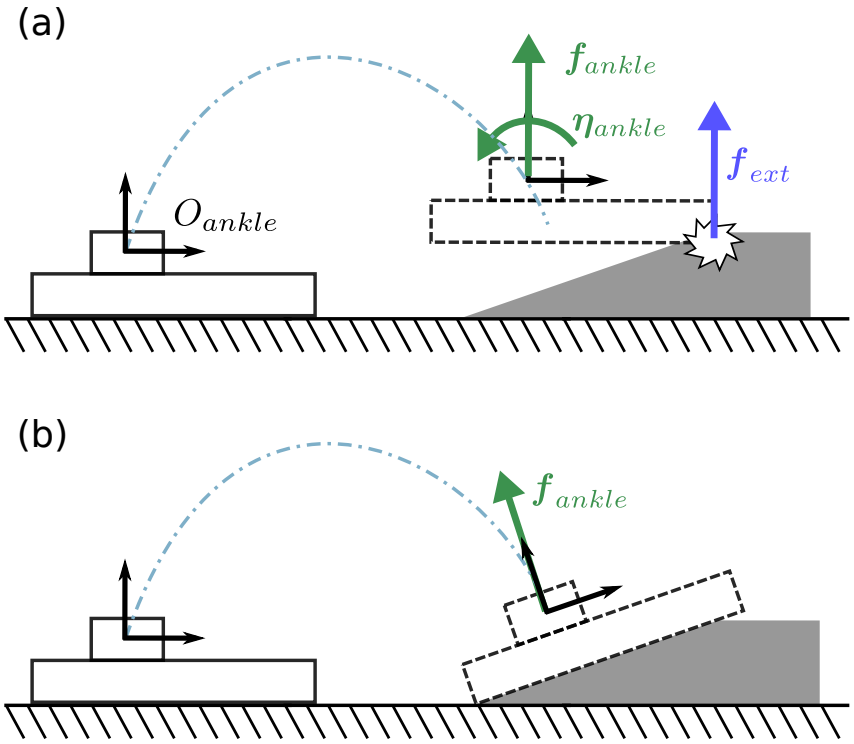

Figure 48 Foot compliance with ankle force-torque sensors: (a) foot compliance for uneven terrain is triggered when an external force spikes as a result of a collision with an unexpected obstacle. (b) foot motion is generated to minimize the ankle torque τ_{ankle} which causes the adaptation of the foot orientation to comply with the terrain conditions.

Proximity sensing plantar skin can provide the terrain information required approach the problem of walking on uneven terrain, enabling *PFC* for the foot orientation and a virtual repellent force for smoothly stopping the landing foot. The formulation for the PGRW (Preemptive Ground Reaction Wrench) in Section 4.2.6 provides the computation of the repulsive forces needed for the PFC.

The VGRW (Virtual Ground Reaction Wrench) can be added as a complementary input to any foot admittance or motion tracking controller for ankle force-torque sensors without significant changes in the formulation. However, its contribution must be set to zero once the foot touches the ground to avoid adding disturbances to the balance controller. Let us define a sole wrench for PFC as

$$\boldsymbol{w}_{sole} = \begin{cases} \boldsymbol{w}_f + \boldsymbol{w}_p & \text{for } ||\boldsymbol{w}_f|| = 0 \\ \boldsymbol{w}_f & \text{for } ||\boldsymbol{w}_f|| > 0 \end{cases} \tag{4.30}$$

Fig. 49 shows the preemptive foot compliance during one stride. It starts when the swing foot approaches an unexpected obstacle or an inclined terrain segment (Fig. 49-a). When the terrain enters the proximity sensors' range, the PFC starts damping the swing motion (Fig. 49-b). Simultaneously, the sole is pushed to adopt the terrain orientation (Fig. 49-c). This can be done by any controller that minimizes $\boldsymbol{\eta}_p$. The foot tracking motion is damped by $\boldsymbol{f}_p$ which increases as the foot gets closer to the terrain. The preemptive foot compliance can

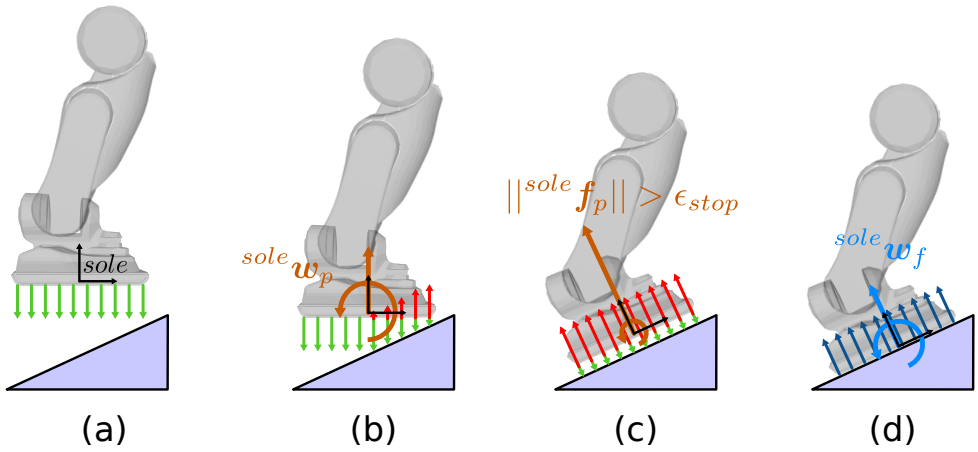

Figure 49 (a) the swing foot with plantar proximity sensing approaches an obstacle. (b) when the obstacle enters the sensing range, a virtual repellent force field produces a virtual GRW ${}^{sole}\boldsymbol{w}_p$. (c) foot motion damps due to ${}^{sole}\boldsymbol{w}_p$ and stops when $||{}^{sole}\boldsymbol{f}_p|| > \epsilon_{stop}$ while adapting the foot orientation to match the terrain slope. (d) once foot landed, the real GRW ${}^{sole}\boldsymbol{w}_f$ (measured by force sensing taxels) is used as feedback.

be used to define an early contact for stopping the swing motion when the virtual exceeds a certain threshold

$$\boldsymbol{f}_p > \epsilon_{stop} \tag{4.31}$$

However, there can be cases where the foot lands before the early contact condition Eq. (4.31) is fulfilled. This can happen, for example, when the foot lands over a partial foothold that generates a small $\boldsymbol{f}_p$. Once the foot lands, the real GRW measured from force-sensing taxels or an ankle force-torque sensor must be used for a final adjustment of the foot on the terrain (Fig. 49-d).

4.4.1.1 Experiment: HRP-2Kai robot steps over moving obstacle using PFC

The PFC effects can be seen in Fig. 50. The HRP-2 robot steps in place and an obstacle is slid below a foot while landing. The proximity sensing adjusts the orientation of the foot before the contact and stops the swing motion before the impact. With this preemptive adaptation, the impact against an unexpected obstacle produces a smaller disturbance to the balance controller, which can coup with it by distributing the ground reaction forces over the available contact geometry.

4.4.1.2 Experiment: HRP-2Kai robot on flat ground, foot landing impact reduction with PFC

Adding the PFC force component from Eq. (4.30) to the ankle force measurement, we can detect early contacts and stop the foot swing motion before hitting the ground. This impact reduction is visible when walking over flat ground as shown in Fig. 51. In this experiment, the HRP-2Kai robot is commanded to take 6 forward steps of 20 cm with $t_{ss} = 1.4$, and $t_{ds} = 0.5$ and 5 cm height. With the proximity sensors disabled, the walking motion produces impacts

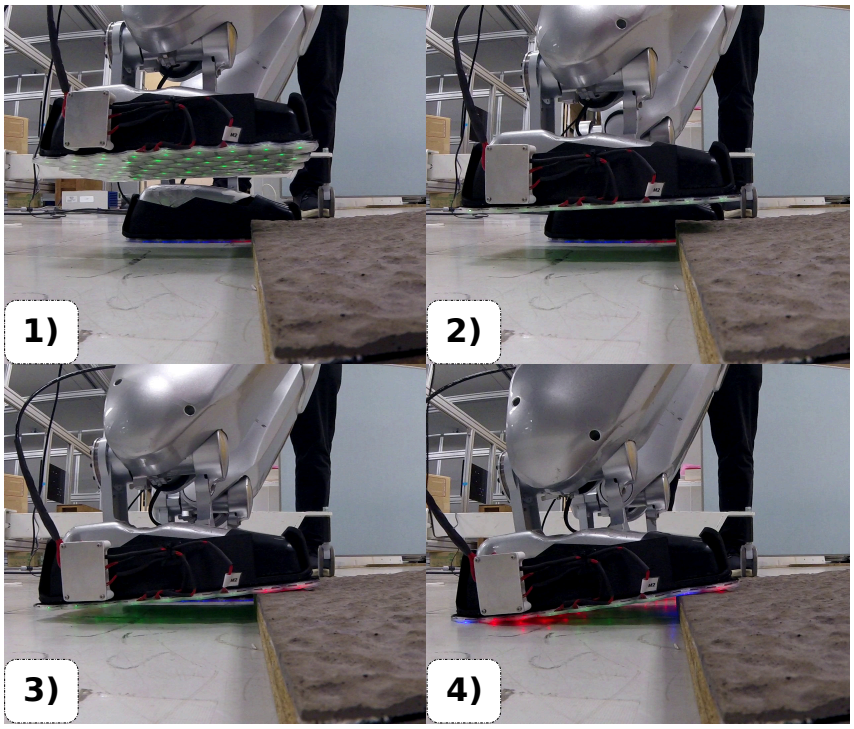

Figure 50 Preemptive foot compliance in the HRP-2 robot. The robot is stepping in place and an obstacle is introduced below the sole during a foot swing phase.

$\approx$ 350 N. With the proximity sensing enabled, the impact forces are reduced to below 200 N and suppressed to 0 N in some steps.

Fig. 52 shows the impact ranges of the two runs. The left bar shows the maximum and minimum impact recorded when PFC is off. The maximum impact is 430 N, the minimum impact is 156 N, and the average impact is 340 N. When the PFC is enabled, the maximum impact is 200 N, the minimum impact is 0 N which means a smooth foot landing, and the average impact is 58 N. The average impact with PFC is 17% of the average impact with no PFC. The maximum impact with no PFC is 46% of the maximum impact with no PFC.

4.4.1.3 Experiment: H1 robot on flat ground, foot landing impact reduction with PFC

Let us analyze the impact suppression effect of PFC in a larger stepping run in the H1 robot. In this experiment, the H1 robot takes 100 steps under two conditions, first with PFC *on* and then with PFC *off*. In both cases, the single support phase time is $t_{ss} = 0.9$, and the double support time is $t_{ds} = 0.3$. The step height is 5 cm Fig. 53 shows the impacts recorded by the left ankle force-torque sensor during the runs. Fig. 53-a shows the landing impact magnitudes measured by the left ankle force-torque sensor $\boldsymbol{f}_f$ when the PFC is disabled. Fig. 53-b shows the run with PFC enabled. The impact forces are smaller with the PFC and in several steps, the impact force is 0 N.

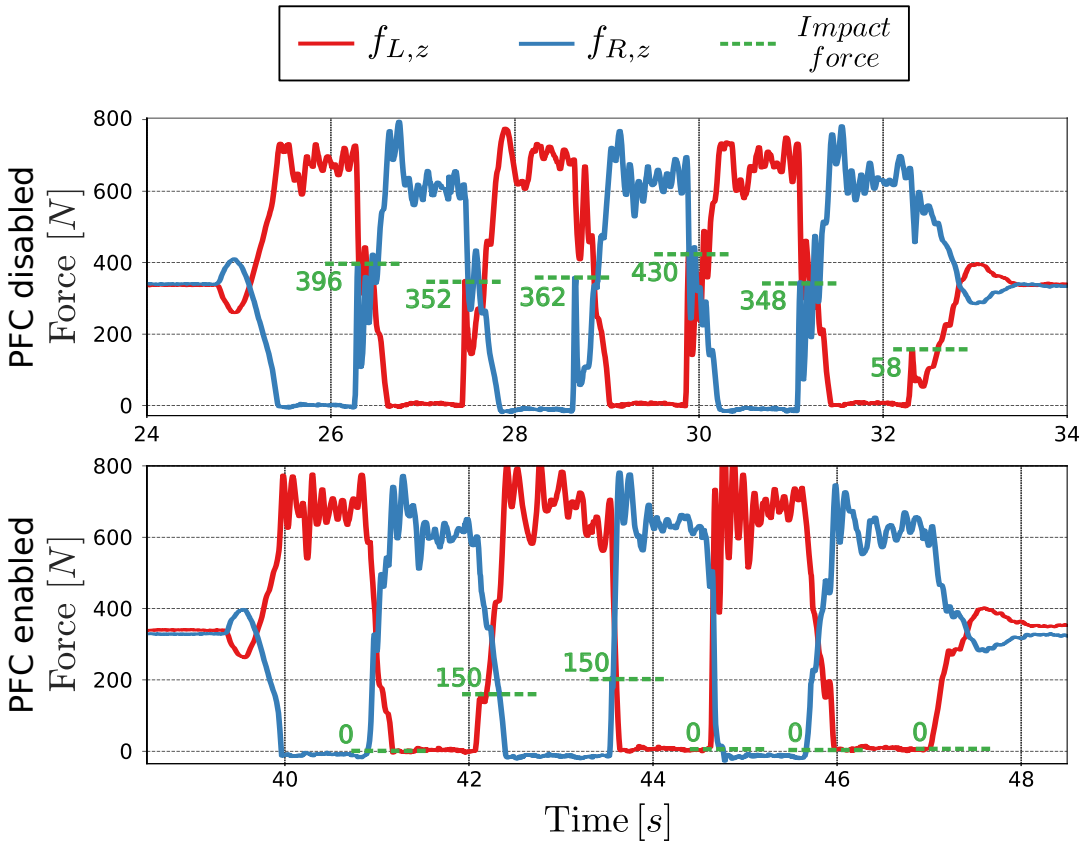

Figure 51 An effect of the PFC is the reduction of impact forces, even on walking over flat ground. The HRP-2Kai robot takes 6 forward steps with $t_{ss} = 1.4$, and $t_{ds} = 0.5$. In the upper plot, PFC is disabled and the HRP-2Kai robot hits the ground with a force $\approx$ 350 N in every step. In the lower plot, the PFC reduces the impacts below 200 N and suppresses them to 0 N in some of the steps.

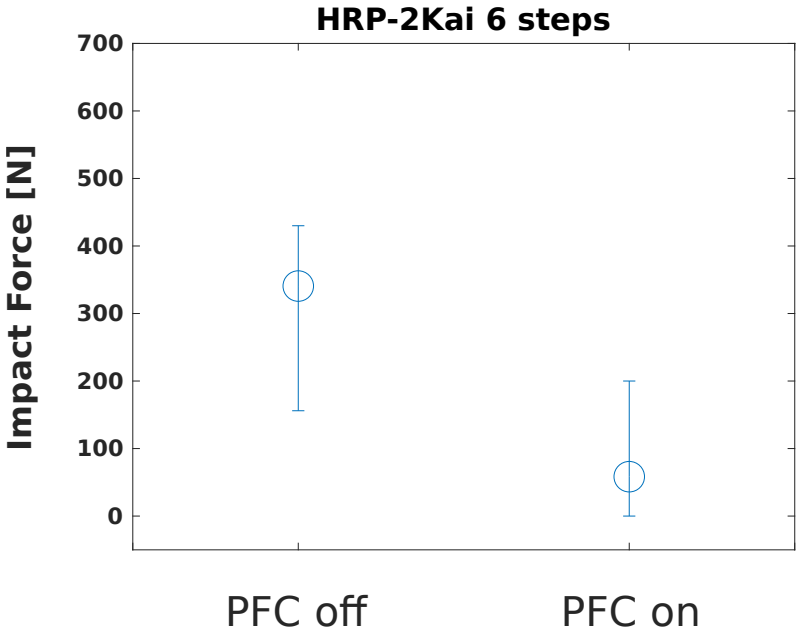

Figure 52 Impact reduction caused by PFC in the HRP-2Kai robot taking 6 steps. The average impact with PFC on is 17% of the average impact when PFC is off. The maximum impact recorded with PFC is 430 N. With PFC on the maximum impact recorded is 200 N which is a reduction of 54%.

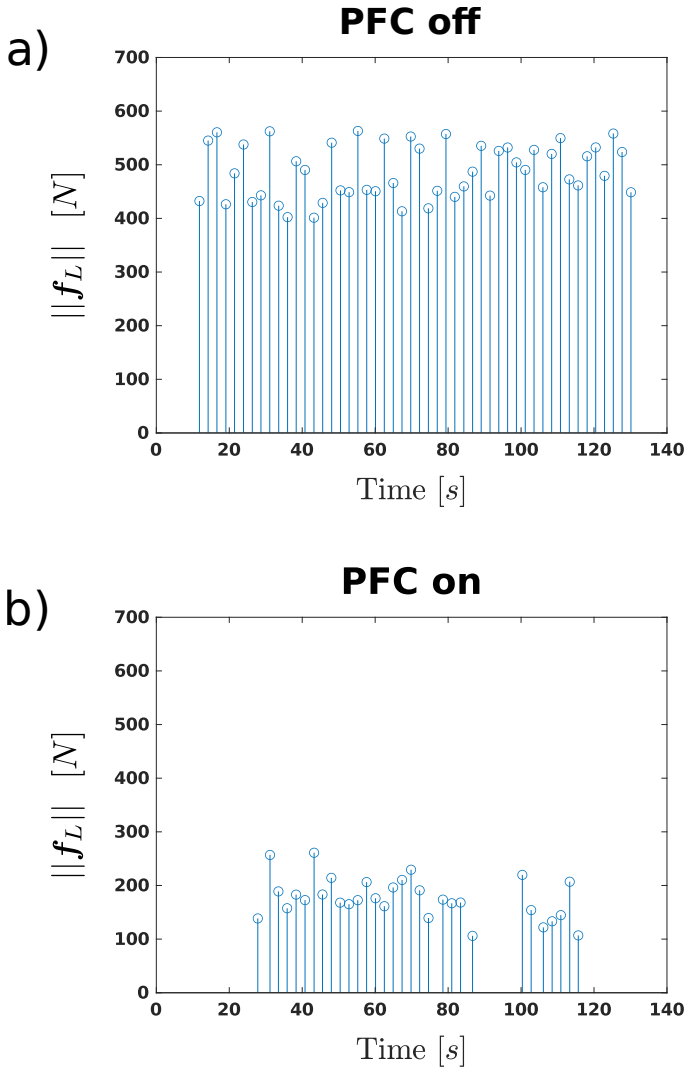

Figure 53 Left foot landing impacts. a) The H1 robots took 100 steps (50 with the left foot) with no PFC. b) The same experiment with PFC enabled. The missing impacts are recorded as 0 N by the ankle force-torque sensor, they are lower than the activation threshold of 50 N.

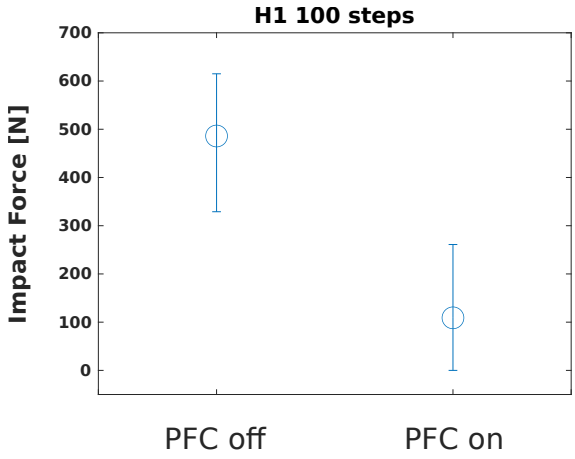

Figure 54 Impact reduction caused by PFC in the H1 robot taking 100 steps. The average impact with PFC on is 22% of the average impact when PFC is off. The maximum impact recorded with PFC is 615 N. With PFC on the maximum impact recorded is 261 N which is a reduction of 58%.

Fig. 54 shows the impact ranges of the two runs. The left bar shows the maximum and minimum impact recorded when PFC is off. The maximum impact is 615 N, the minimum impact is 329 N, and the average impact is 486 N. When the PFC is enabled, the maximum impact is 261 N, the minimum impact is 0 N which means a smooth foot landing, and the average impact is 109 N. The average impact with PFC is 22% of the average impact with no PFC. The maximum impact with no PFC is 42% of the maximum impact with no PFC.

At first glance, this improvement may not be necessary for flat ground and the impacts can be absorbed by passive elements such as soft rubber soles or ankle couples. However, the picture is different if an unexpected obstacle is hit at foot landing.

4.4.1.4 Experiment: H1 robot over a flat obstacle, foot landing impact reduction with PFC

The impact reduction effect of the PFC applies also when early contacts are caused by uneven terrain conditions. This experiment shows the effect when walking over obstacles. Walking controllers for flat ground cannot deal with discontinuities in the terrain height. The impact caused by an unexpected rise in the terrain height disturbs the balance of the walking controller and can cause it to fall. The risk increases if the step time is shorter, e.g. dynamic walking.

In Fig. 55, the H1 robot takes 6 forward steps of 20 cm with $t_{ss} = 0.9$, and $t_{ds} = 0.3$. However, in the third step, an obstacle with a height of 3 cm is hit with the left foot. When the PFC is disabled, the impact produced by the unexpected obstacle $\approx$ 1100 N. The disturbance causes the walking controller designed for flat ground to lose balance and fall. The impact is abrupt and the force-torque sensor cannot stop the swing motion in time to reduce it. When the PFC is enabled, the early contact is anticipated by the virtual force $\boldsymbol{f}_p$ and the foot swing motion stopped in time. The impact produced by the obstacle is $\approx$ 370 N, and the disturbance on the balance controller is suppressed successfully. The impact in this case is in the same

range as the impacts on flat ground recorded in the experiment in Section 4.4.1.3.

4.4.2. Walking motion adjustment from contact geometry

Although preemptive foot compliance helps find suitable footholds over uneven terrain, the terrain geometry must be considered to adapt the walking motions to keep the stability. For example, the three-dimensional control in [184] compensates for height variations in the terrain, [181, 86], and [180] adapt to terrain inclination, and [94] adapts the walking motions to step on partial footholds including line contacts.

Motion planning for walking commonly starts by planning the footsteps over the terrain. Then, a feasible reference ZMP trajectory within these footsteps is created. A common strategy is to define the ZMP way-points at the center of the planned steps where full sole contact is assumed. Finally, a smooth trajectory for the center of mass is interpolated using a simplified model such as the LIP. Nevertheless, during the execution of the motion, disturbances and uncertainties make the system deviate, and feedback control is required to track the reference trajectories. Therefore, the trajectories should be continuously adjusted from sensor feedback every time a foot takes a new step. Let us analyze the case of a foot landing over a partial foothold and how plantar tactile information helps re-plan the motion.

As described in Section 4.2.5, plantar robot skin provides an approximation of the real contact geometry and thus the supporting polygon. Additionally, the centroid of a convex polygon can be easily computed with fast algorithms as [185]. The centroid of the supporting polygon r_f can be used as an immediate new reference position for the ZMP right after contact is detected as shown in Fig. 56.

Depending on the capabilities of the robot, a security check with the relation of the sole area A_{sole} and the supporting polygon area A_f can be defined to decide to step over the obstacle or take other action, for example, a step re-plan as in Section 4.3.2, or an emergency stop as in [186].

4.4.3. Balance control using the contact geometry

A necessary condition for stable biped walking is the existence of the ZMP inside the supporting polygon [155]. Furthermore, if the ZMP gets too close to the edge, the robot can tilt at the slightest disturbance and fall. To prevent this, balance controllers push the ZMP away from the edges of the supporting polygon by distributing the contact forces along the sole. Different strategies can be applied for balance control, an efficient method is to used a feedback loop of the DCM to shift the target position of the ZMP. Let us complement it with the plantar tactile information.

In Section 4.1.1, we expressed the walking dynamics in terms of the LIP model with Eq. (4.1). Then, in Section 4.1.3 we revised the generation of stable walking motions using the LIP model and the DCM. Finally, in Section 4.1.4 we revised the feedback control required

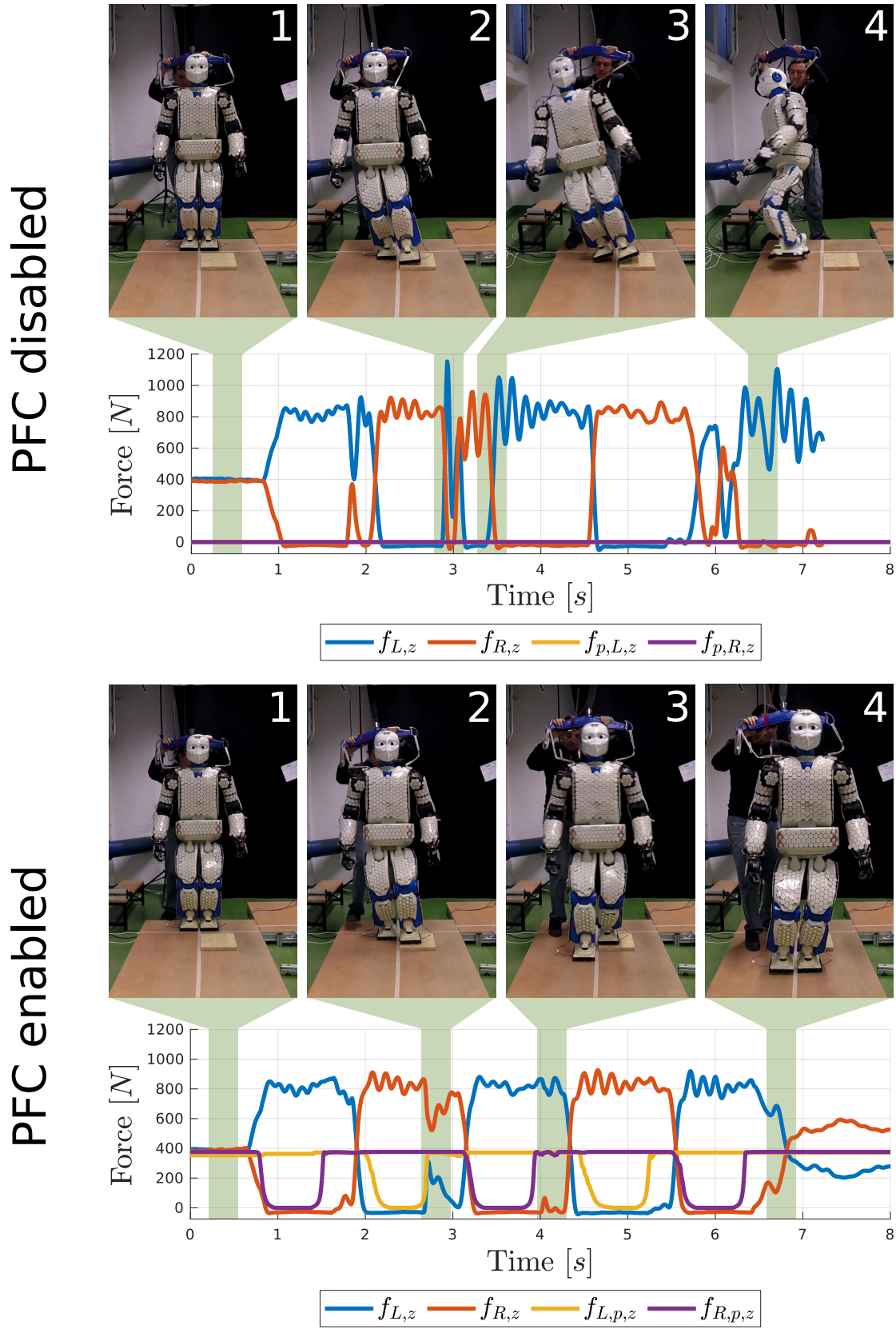

Figure 55 The H1 robot walks over flat ground and finds an unexpected 3cm obstacle ($t_{ss} = 0.9$, $t_{ds} = 0.3$). In the upper plot, PFC is disabled and the 1150 N impact produced by the obstacle causes a robot to fall. In the lower plot, the PFC anticipates the obstacle and damps the impact to 370 N. This allows the stabilizer to keep the balance and continue walking.

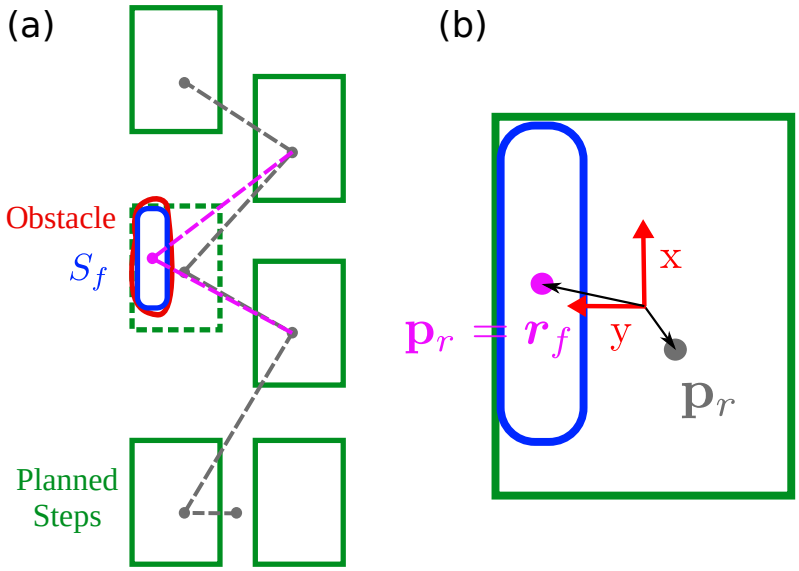

Figure 56 Reference ZMP adjustment from tactile information when a foot lands over a foothold smaller than the robot sole. (a) the centroid $\boldsymbol{r}_F$ of the supporting polygon S_F can be directly assigned as new ZMP reference. (b) Closer look at the ZMP reference change from the original plan $\boldsymbol{p}_{ref}$ to the centroid $\boldsymbol{r}_F$.

to track the walking motions closing the loop with information on the ground reactions. The chain structure of the DCM and the LIP model helped propagate the feedback to stabilize the walking motions. Eq. (4.18) minimizes the DCM deviations by shifting the desired position for the ZMP. Nevertheless, $\mathbf{p}$ must stay within the supporting polygon to keep the stability. Therefore, its reference trajectory $\mathbf{p}_d$ must be constrained inside the estimated supporting polygon S_f as a safety measurement. Englsberger et al. proposed adjusting $\mathbf{p}_d$ to the closes point in the known sole geometry. However, there was no knowledge on the real shape of the contact and thus full sole contact was assumed.

Plantar skin provides the missing information on the contact geometry that will help constraint $\mathbf{p}_d$. Hence, after computing a first approximation $\mathbf{p}_{d,ini}$ two cases are possible as shown in Fig. 57: a) $\mathbf{p}_{d,ini}$ lays inside S_f and $\mathbf{p}_d = \boldsymbol{p}_{d,ini}$, b) $\mathbf{p}_d$ lays outside S_f and must be shifted to the closest point in S_f. Algorithm 1 verifies the first case and implements the second when needed from the vertices of S_f and an initial adjusted ZMP reference $\mathbf{p}_{d,ini}$.

$\mathbf{p}_d$ is now constrained inside an accurate approximation of the supporting polygon. Additionally, the supporting polygon as a constraint for ZMP control is known. Therefore, $\mathbf{p}_d$ can be tracked with any ZMP tracking control to close the loop on for the walking control. For example Eq. (4.20) or the QP (Quadratic Programming) formulation in [8].

4.4.4. Constrained contact wrench distribution

A common strategy for ZMP tracking is through CoM admittance control [187]. However, plantar wrench control can improve the ZMP tracking by distributing the contact forces along the sole [188]. Furthermore, if the contact area is smaller than the sole, such distribution of forces must be kept within the contact geometry. Fortunately, the supporting polygon

Algorithm 1 Constraining $\mathbf{p}_d$ inside S_f

Input: S_k: the k vertices of S_f in clockwise order,
$\mathbf{p}_{d,ini} \in \mathbb{R}^3, \mathbf{p}_{d,ini,z} = 0 \in \mathbb{R}^3$
Output: $\mathbf{p}_d \in S_f$ such that
$||\mathbf{p}_d - \mathbf{p}_{d,ini}|| = \inf\{||a - \mathbf{p}_{d,ini}|| \mid a \in S_f\}$

Function $next(j)$
if $j = k$ **then**
return 1
else
return $j + 1$
end if

$\mathbf{p}_d = S_k(1)$
$inside = \text{true}$
for $i = 1$ to k **do**
$\boldsymbol{l} = S_k(next(i)) - S_k(i)$
$\boldsymbol{d} = \mathbf{p}_{d,ini} - S_k(i)$
$\boldsymbol{v} = d \times l$
if $v_z > 0$ **then**
$r = (\boldsymbol{d} \cdot \boldsymbol{l}) \,/\, (\boldsymbol{l} \cdot \boldsymbol{l})$
if $r \leq 0$ **then**
$\tilde{\mathbf{p}}_d = S_k(i)$
else if $0 < r < 1$ **then**
$\tilde{\mathbf{p}}_d = S_k(i) + r\boldsymbol{l}$
else if $1 \leq r$ **then**
$\tilde{\mathbf{p}}_d = S_k(next(i))$
end if
if $||\mathbf{p}_{d,ini} - \tilde{\mathbf{p}}_d|| < ||\mathbf{p}_{d,ini} - \mathbf{p}_d||$ **then**
$\mathbf{p}_d = \tilde{\mathbf{p}}_d$
end if
$inside = \text{false}$
end if
end for
if $inside$ **then**
$\mathbf{p}_d = \mathbf{p}_{d,ini}$
end if

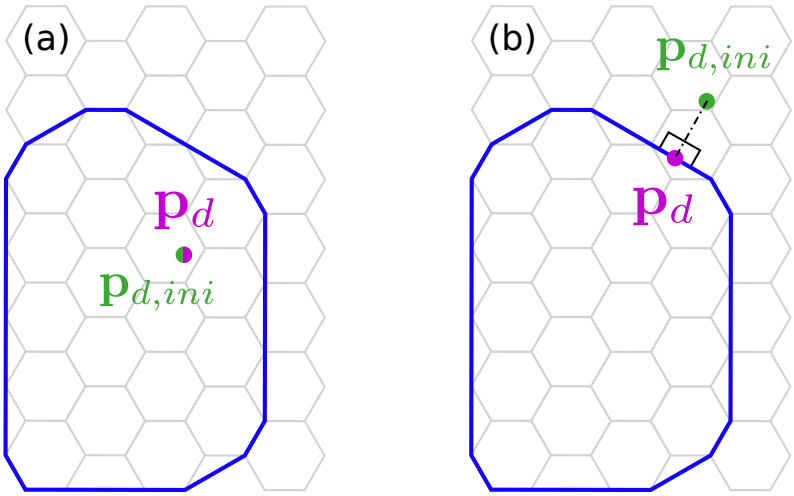

Figure 57 Adjustment of reference ZMP $\mathbf{p}_d$ to stay inside S_f from an initial approximation $\mathbf{p}_{d,ini}$. a) $\mathbf{p}_{d,ini}$ lays inside S_f and $\mathbf{p}_d = \mathbf{p}_{d,ini}$, b) $\mathbf{p}_d$ lays outside S_f and must be shifted to the closest point in S_f.

estimated with plantar skin can help define constraints for different controllers. As an example, let us adapt the contact stability formulation proposed by Caron et al. [8], which defines linear constraints for an ankle-wrench distribution QP from the supporting polygon assuming full-sole contacts. The formulation of these constraints is the sole wrench cone

$$|f_x| \leq \mu f_z \tag{4.32}$$
$$|f_y| \leq \mu f_z \tag{4.33}$$
$$f_z > 0 \tag{4.34}$$
$$|\tau_x| \leq Y f_z \tag{4.35}$$
$$|\tau_y| \leq X f_z \tag{4.36}$$
$$\tau_{z,min} \leq \tau_z \leq \tau_{z,max} \tag{4.37}$$

where

$$\tau_{z,min} \coloneqq -\mu (X+Y) f_z + |Y f_x - \mu \tau_x| + |X f_y - \mu \tau_y| \tag{4.38}$$
$$\tau_{z,max} \coloneqq +\mu (X+Y) f_z - |Y f_x + \mu \tau_x| - |X f_y + \mu \tau_y| \tag{4.39}$$

μ is the friction coefficient, and X, Y are the dimensions of the sole as shown in Fig. 58. Let us now consider the case of a partial foothold to rewrite the wrench cone. For simplicity as a proof of concept, we will keep the constraint that the contact is still an axis-aligned rectangle. This rectangle can be constructed by optimization algorithms as [189] to find the maximum area rectangle, or merely as a bounding box of the contact with a safety inner offset. Note that the second is less accurate but faster to compute, and therefore would require a conservative margin to be applicable in realistic scenarios.

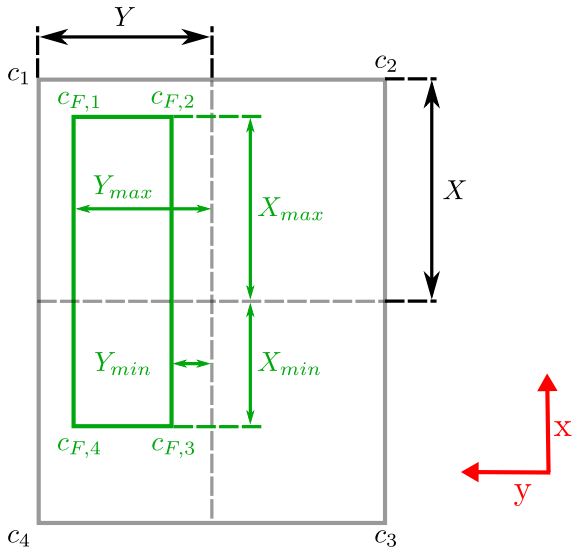

Figure 58 Contact constraints geometry in [8] adapted to smaller contact rectangular areas approximated by plantar skin.

As shown in Fig. 58, the limits of the contact are now divided by maximum X_{max}, Y_{max} and minimum X_{min}, Y_{min} for each axis. With this geometry, the torsional part of the wrench cone (Eq. (4.38) and (4.39)) is redefined as

$$Y_{max} f_z \leq \quad \tau_x \quad \leq Y_{min} f_z \tag{4.40}$$

$$X_{min} f_z \leq \quad \tau_y \quad \leq X_{max} f_z, \tag{4.41}$$

however, the constraints for τ_z can no longer be expressed in the concise notation of Eq. (4.39) and (4.39), and must consider the different cases

$$\begin{aligned}
-Y_{max} f_x - X_{max} f_y - \mu(X_{max} + Y_{max}) f_z + \mu\tau_x + \mu\tau_y &\leq \tau_z \\
-Y_{max} f_x + X_{min} f_y - \mu(X_{min} + Y_{max}) f_z + \mu\tau_x - \mu\tau_y &\leq \tau_z \\
+Y_{min} f_x - X_{max} f_y - \mu(X_{max} + Y_{min}) f_z - \mu\tau_x + \mu\tau_y &\leq \tau_z \\
+Y_{min} f_x + X_{min} f_y - \mu(X_{min} + Y_{min}) f_z - \mu\tau_x - \mu\tau_y &\leq \tau_z \\
-Y_{max} f_x - X_{max} f_y + \mu(X_{max} - Y_{max}) f_z - \mu\tau_x - \mu\tau_y &\geq \tau_z \\
-Y_{max} f_x + X_{min} f_y + \mu(X_{min} - Y_{max}) f_z - \mu\tau_x + \mu\tau_y &\geq \tau_z \\
+Y_{min} f_x - X_{max} f_y + \mu(X_{max} - Y_{min}) f_z + \mu\tau_x - \mu\tau_y &\geq \tau_z \\
+Y_{min} f_x + X_{min} f_y + \mu(X_{min} - Y_{min}) f_z + \mu\tau_x + \mu\tau_y &\geq \tau_z
\end{aligned}$$

With these new constraints, the solution of the QP will generate an ankle wrench, which distributes the contact forces on the corners of the rectangle $c_{F,i}$ shown in Fig. 58.

4.4.5. Experiment: Stepping over partial footholds

Two robots running different controllers were used to validate the plantar sensing with the formulations from this Section: a) the HRP-2Kai robot [3] described in Section 2.3.3. The tactile information was added in the foot admittance task of the open source[2] controller implemented by Caron et al. [127]. The ZMP adjustment from the center of the supporting polygon was adapted without deep modifications into the code. b) the H1 robot described in Section 2.3.2. The H1 robot runs the $\mathrm{ros\_control}$ framework [126] and a custom walking controller based on the DCM dynamics similar to [6] as described in Section 4.1.

Plantar robot skin is mounted on both robots with the shoes described in Section 4.2.2. The skin system delivers four sensing modalities (force, proximity, temperature, and acceleration) at a maximum update rate of 250 Hz.

The principles described in this section were primarily validated on the HRP-2 robot. The single support time was assigned as $t_{ss} = 1.4$, and the double support time as $t_{ss} = 0.5$. Additionally, the weights of the cost function were adjusted as follows: $\boldsymbol{W}_{\dddot{\boldsymbol{x}}} = 5$ for the CoM jerk, $\boldsymbol{W}_{\dot{\boldsymbol{x}}} = 100$ for the CoM velocity, and $\boldsymbol{W}_{\boldsymbol{p}} = 50$ for the ZMP. This adjustment was required to reduce the ZMP distribution reactions due to the small surface of the foothold. The tuning of the weights was done by trial and error in simulation.

Subsequently, the second round of experiments was validated for the H1 robot with faster-walking motions and smaller footholds. For the H1 robot, the single support time was assigned as $t_{ss} = 0.9$, and the double support time as $t_{ss} = 0.3$. In all the experiments, early contacts are assumed when the contact force in the landing foot is larger than 70 N. Two sets of experiments were prepared for each robot walking over obstacles with an area smaller than the foot sole. The robots are commanded to take 6 forward steps. The step size is 20 cm and the height of the swing foot motion to 8 cm.

4.4.5.1 Experiment: HRP-2Kai stepping over partial footholds

The first experiment shows the HRP-2 robot walking over two different obstacles. In Fig. 59, the obstacle is only supporting the rear half of the robot sole. When the foot lands over the obstacle, the plantar skin approximates the shape of the contact and the constraints for the ZMP X_{max}, and X_{min} are defined. Additionally, the reference point for the ZMP $\mathbf{p}_r$ is shifted to the center of the contact area. Then, while shifting the robot's weight to the new supporting foot, the balance controller shifts the desired ZMP $\mathbf{p}_d$ to track the reference. Nevertheless, the adjustment is constrained within X_{max}, X_{min}, Y_{max}, and Y_{min}. These limits are also used to define the constraints for the wrench distribution QP, which controls the real ZMP $\mathbf{p}$. A closer look at the constraint adjustment is detailed in Fig. 59-c. The dashed green line is the original constraint X, which considers full sole contact.

[2] $\mathrm{https://github.com/stephane-caron/lipm\_walking\_controller}$

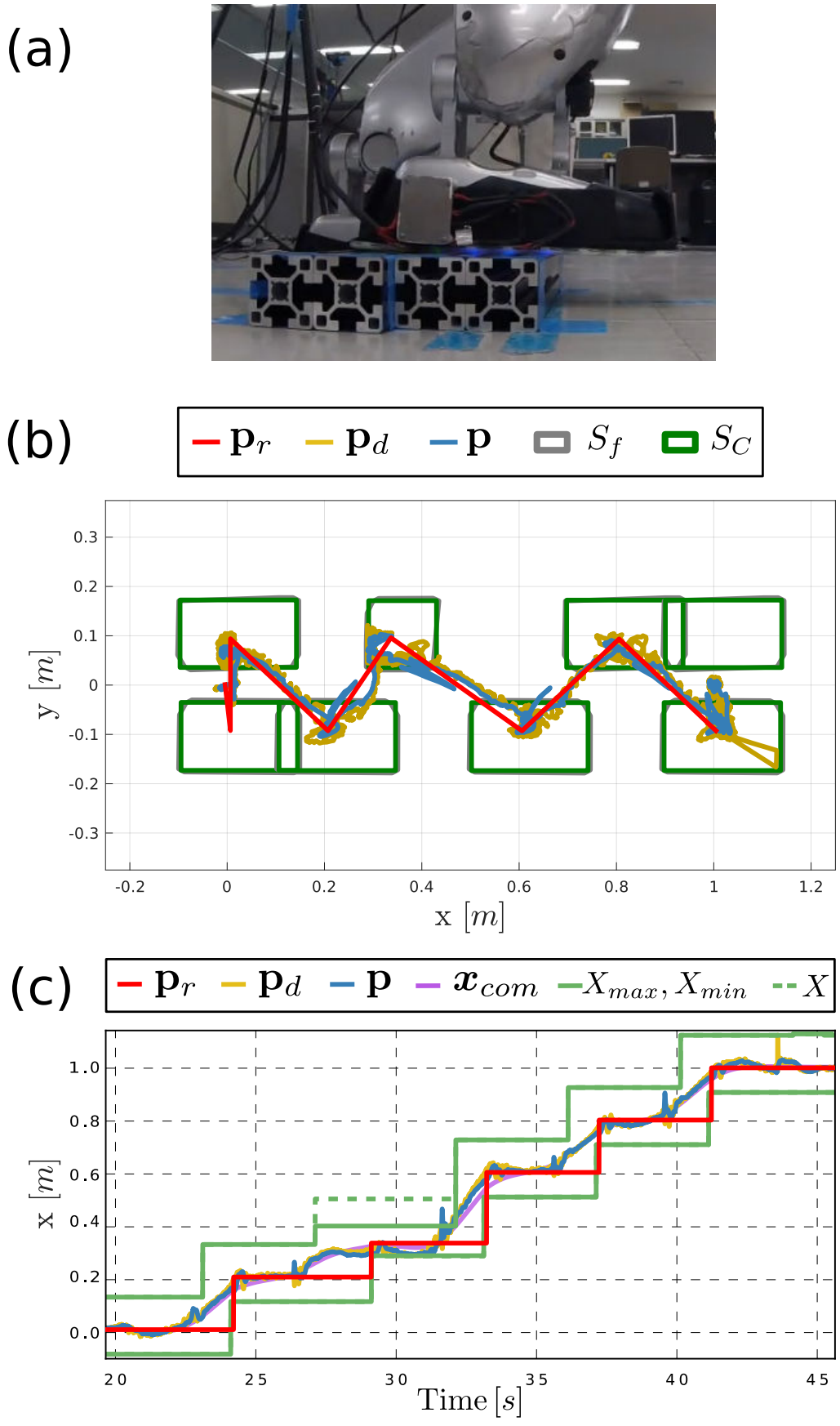

Figure 59 The HRP-2Kai robot walks over an onstacle that is half the size of the sole. The plantar skin approximates the supporting polygon S_F, and the contact constraints for the ZMP wrench distribution control are defined as the bounding box S_F with a safety inner offset of 1 cm. The obstacle requires an adjustment in the sagital direction. The reference ZMP $\mathbf{p}_{ref}$ is shifted to the center of the contact area. The desired ZMP $\mathbf{p}_d$ is adjusted and constrained within the supporting area and the real ZMP $\mathbf{p}$ is controlled to track $\mathbf{p}_d$ considering the hard constraints X_{max},X_{min}.

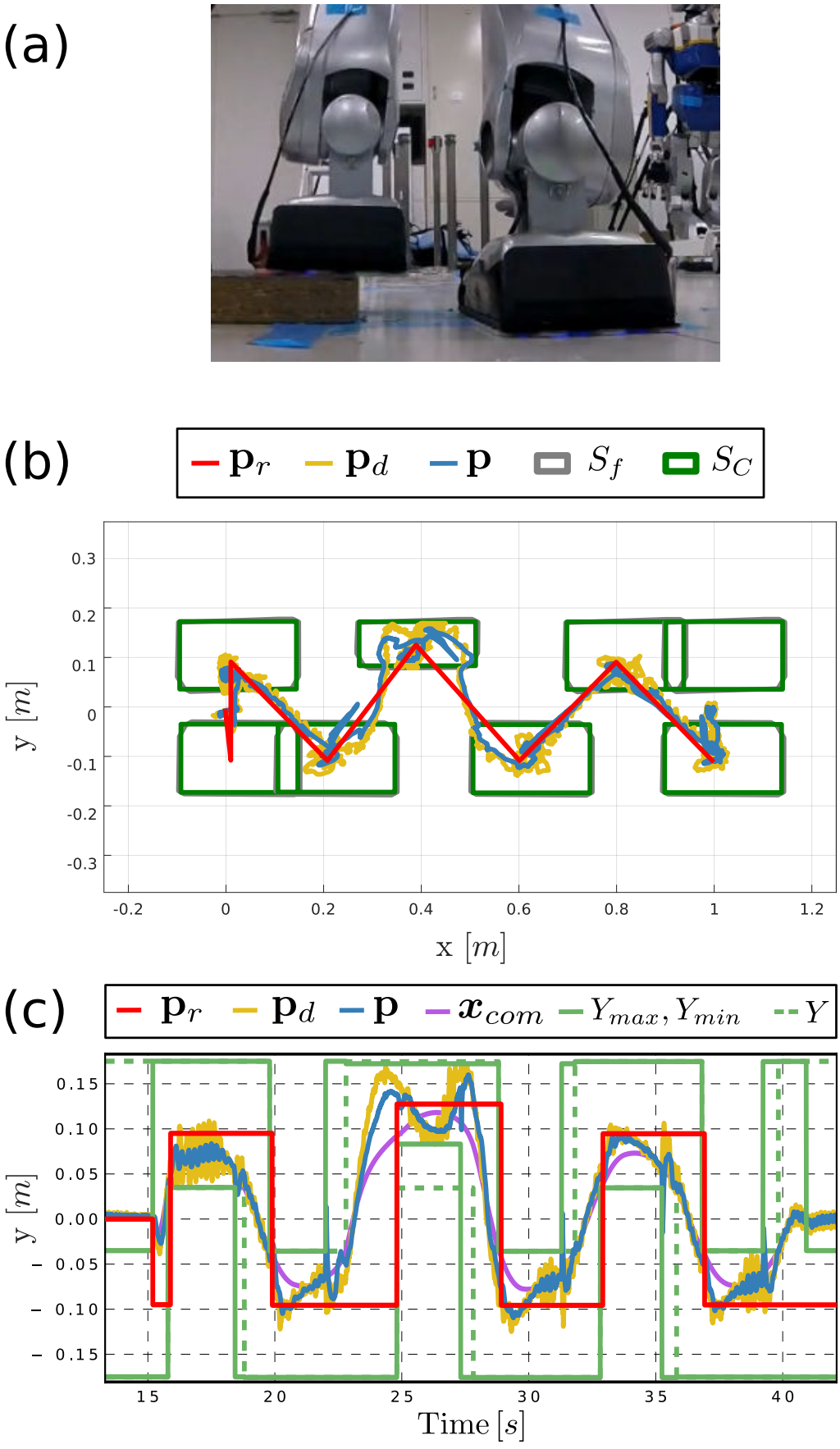

Figure 60 The HRP-2Kai robot walks over an obstacle that is half the size of the sole. The plantar skin approximates the supporting polygon S_F, and the contact constraints for the ZMP wrench distribution control are defined as the bounding box S_F with a safety inner offset of 1 cm. The obstacle triggers an adjustment on the lateral direction. The reference ZMP $\mathbf{p}_{ref}$ is shifted to the center of the contact area. The desired ZMP $\mathbf{p}_d$ is adjusted and constrained within the supporting area and the real ZMP $\mathbf{p}$ is controlled to track $\mathbf{p}_d$ considering the hard constraints Y_{max}, and Y_{min}.

Fig. 60 shows the experiment with another obstacle, which only supports the lateral half of the sole. In this case, the adjustment is performed on the y axis. In Fig. 60-c, the supporting polygon constraints Y_{min} and Y_{max} are plotted and the dashed line shows the full sole geometry.

4.4.5.2 Experiment: H1 robot stepping over partial footholds

A similar experiment with the H1 robot is shown in Fig.61 and Fig. 62. First, the H1 robot walks over a foothold that covers only the rear half of the sole. However, the robot does not have information on the terrain and is commanded to take five forward steps. The step length is 20 cm, and the height is 8 cm. The single support time is 0.9 s and the double support time is 0.3 s. When the foot hits the obstacle, the reference ZMP $\mathbf{p}_r$ is shifted to the centroid of the supporting polygon, and the DCM waypoints are replanned automatically. Then the robot continues walking and constraints the adjustment of the ZMP within the supporting polygon using Algorithm 1.

We ran the same experiment with the H1 robot with a smaller obstacle as shown in Fig. 62. The contact area of the obstacle is $\approx 30\%$ of the H1's sole (Fig. 62-a). Nevertheless, the walking controller can step over it without falling and the ZMP is always kept inside the supporting polygon. Fig. 62-b shows the adjustment of the virtual repellent points $\boldsymbol{r}$ over the contact area. This adjustment is also reflected in the reference DCM trajectory $\boldsymbol{\xi}_{ref}$, and the reference CoM trajectory $\boldsymbol{x}_r$. In these plots, the gray polygons are the different supporting polygons for both the single support and double support phases.

4.4.5.3 Experiment: H1 robot walking over a beam

Walking over partial footholds is possible with plantar tactile feedback as shown in the previous experiments in this section. However, these experiments involved only one obstacle smaller than the sole. To assess the performance of our approach in a continuous walking case, we designed an experiment inspired by the labor of heights workers. Construction workers in high buildings are often required to step on or traverse structures that are built with thin beams. Furthermore, in many cases, they must also carry tools and materials. Heights workers move over scaffolds that are made with thin beams to reduce the drag caused by the wind.

Walking continuously over partial footholds is not possible without plantar sensing. A remarkable example of walking on partial footholds is the work from Wiedebach et al. [94]. However, they map the geometry of the terrain using fast exploratory motions between each step. Their solution is very robust to the terrain conditions but relies on aggressive motions and slow stepping to keep the balance.

(a)

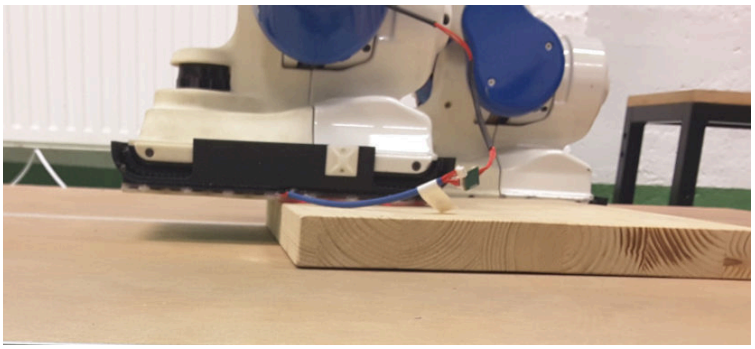

(b)

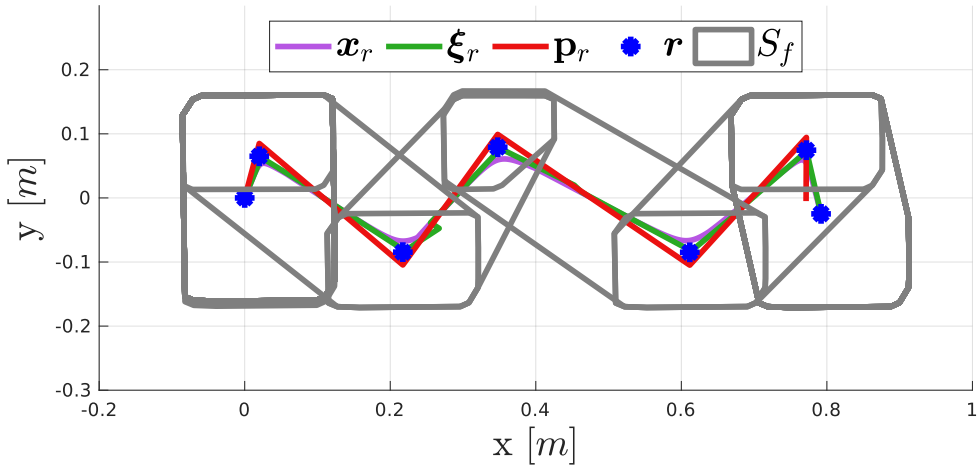

(c)

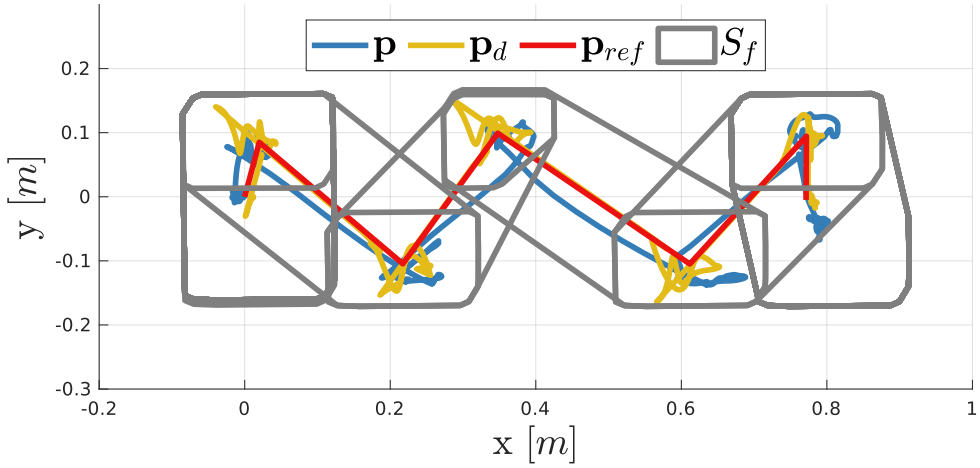

Figure 61 The H1 robot walking over a partial foothold. The upper plot shows the adjustment of the walking reference trajectories. The lower plot shows the tracking of the ZMP constrained in the supporting region S_f. $\boldsymbol{r}$ are the VRPs, $\boldsymbol{\xi}_r$ is the reference trajectory for the DCM, $\boldsymbol{x}_r$ is the reference trajectory for the CoM, $\mathbf{p}_r$ is the reference trajectory for the ZMP, $\mathbf{p}_d$ is the adjusted desired position of for the ZMP, and $\mathbf{p}$ is the real ZMP during the experiment.

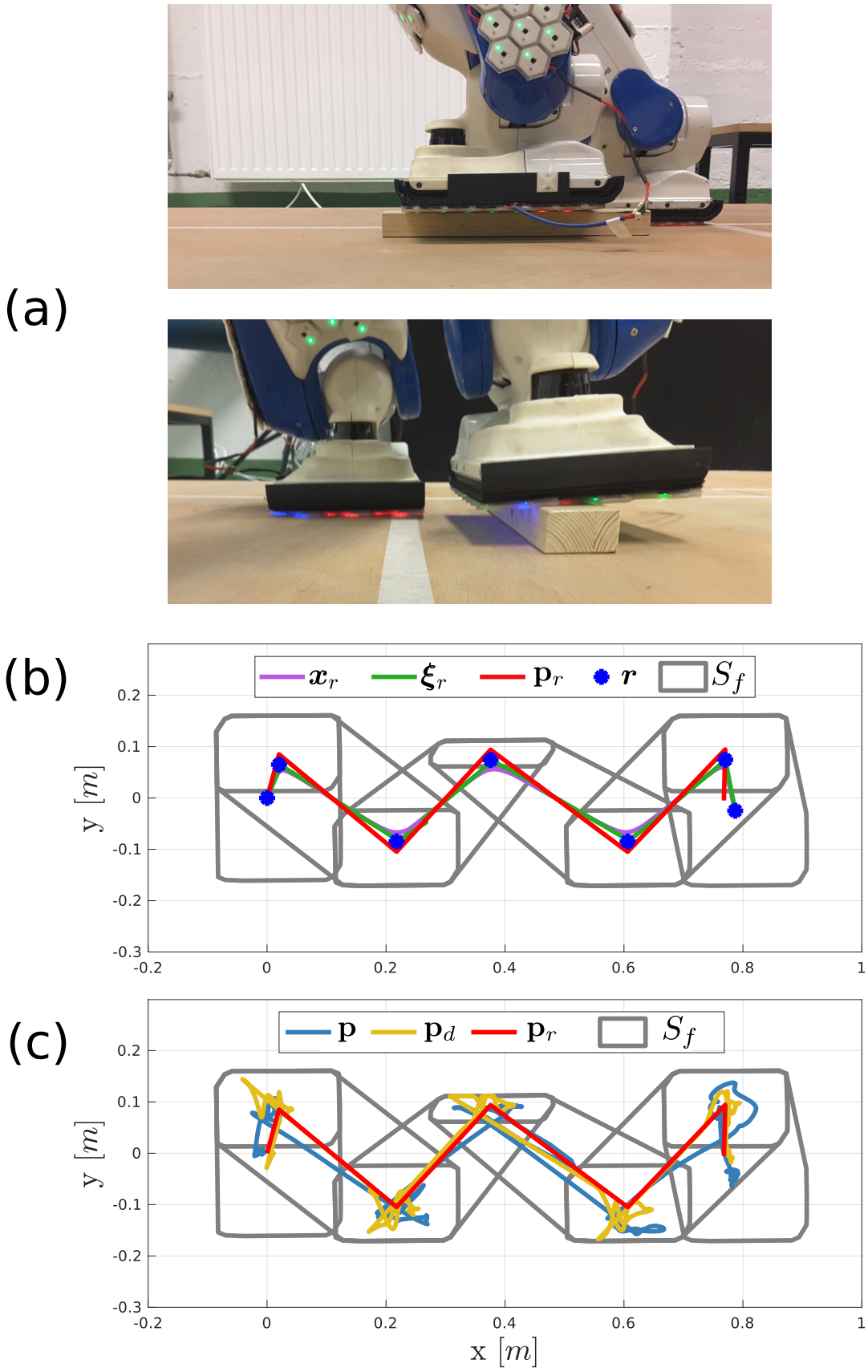

Figure 62 The H1 robot walking over an obstacle smaller than the foot sole (approx. 30% of the sole area). The upper plot shows the adjustment of the walking reference trajectories. The lower plot shows the tracking of the ZMP constrained in the supporting region S_f. $\boldsymbol{r}$ are the VRPs, $\boldsymbol{\xi}_r$ is the reference trajectory for the DCM, $\boldsymbol{x}_r$ is the reference trajectory for the CoM, $\mathbf{p}_r$ is the reference trajectory for the ZMP, $\mathbf{p}_d$ is the adjusted desired position of for the ZMP, and $\mathbf{p}$ is the real ZMP during the experiment.

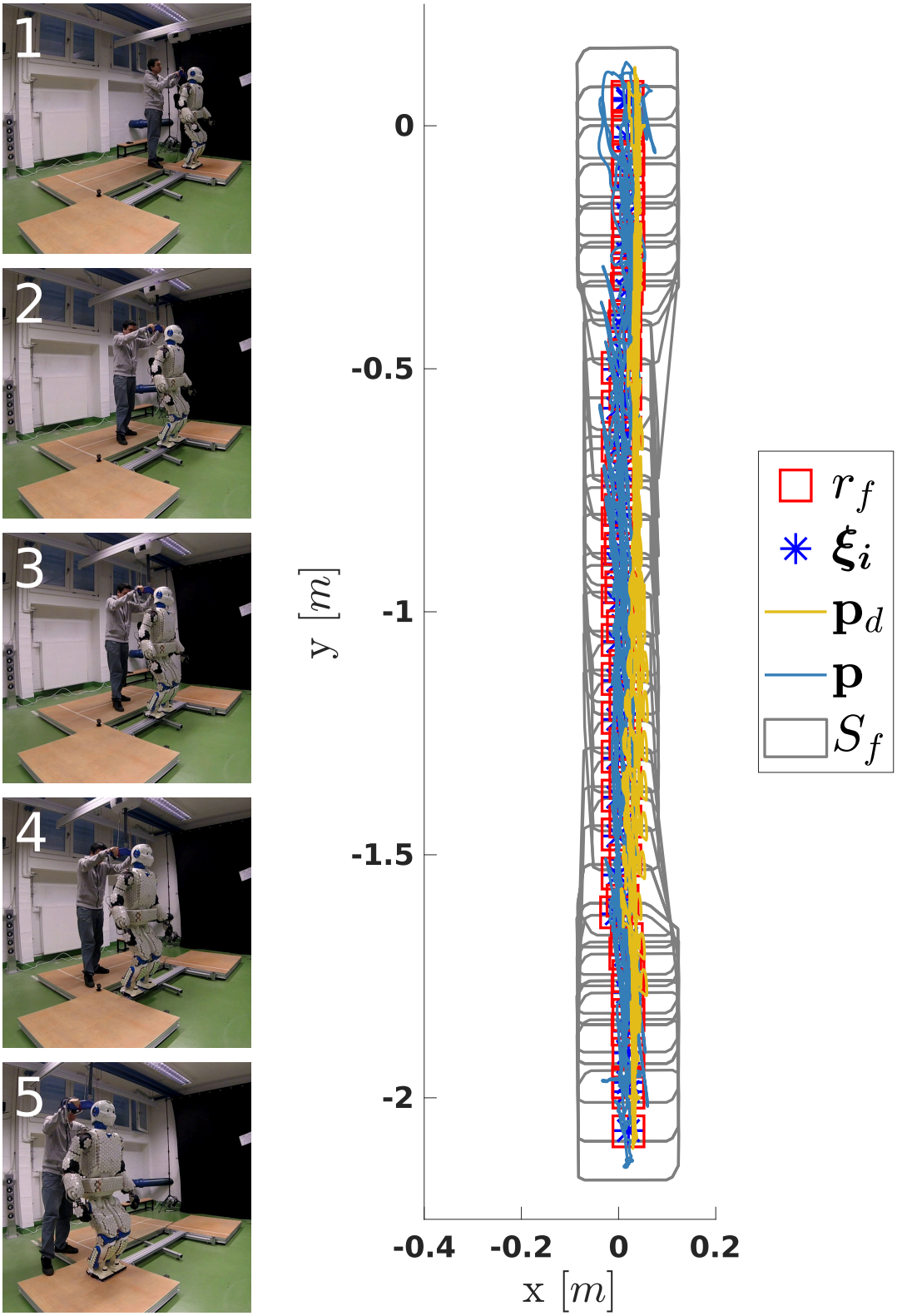

Figure 63 The H1 robot walking over a 12 cm beam. The length of its sole is 25 cm. The supporting polygon constructed from plantar tactile information is used to adjust online the walking motions. The VRPs and thus the DCM waypoints are shifted to the centroid of the polygon acquired right after foot landing. Then the supporting polygon is used to constraint the adjusted reference ZMP $\mathbf{p}_d$ for the balance controller.

In this experiment, we set up a beam between two platforms. The beam is 1.3 m long and 12 cm in width. The H1 robot walked over the beam with 50 side steps of 8 cm going from one platform to the other under two different conditions. In both cases, the single support time is 0.9 s and the double support time is 0.3 s.

Fig. 63 shows the first case of the experiment. The picture sequence shows the robot walking over the beam. In the 2D plot, the gray contours are the supporting polygons S_f acquired with plantar tactile feedback. The walking motions are adapted to the supporting polygon geometry as described in Section 4.4.2. When a foot lands on the beam, the VRP of the next step is shifted to the centroid supporting polygon of the foot, then the DCM waypoints are adjusted to match the new VRP. The supporting polygon is also used to constraint the reference ZMP using algorithm 1. The yellow line is the adjusted ZMP $\mathbf{p}_d$ which is constrained inside S_f with a safety offset of 1.5 cm. The real ZMP $\mathbf{p}$ is represented in the blue line. The red squares show the centroids of the S_f polygons used to adapt the walking motions.

Fig. 64 shows the second case for the experiment, the terrain geometry is the same but the H1 robot was placed in the initial position with a small angular deviation around the z axis. The robot once again takes 50 side steps of 8 cm but when it reaches the beam, the plantar tactile information detects the angular deviation and the walking motions are adapted as described in Section 4.4.5. The supporting polygon with inner offset is also used as constraint for the ZMP reference adjustment in the balance controller.

In this experiment, the H1 robot walked over a 12 cm beam. The foot length of the H1 robot with the tactile shoes is 25 cm, therefore the supporting polygon in every step is about 50% of the sole. Plantar tactile feedback allows the robot to walk over the beam without the need of exploratory motions to map the terrain. Every step provides the geometric information of the foothold immediately after touching the ground. Then the trajectories for the DCM are adjusted online and despite producing an abrupt change in the DCM reference point, the CoM follows the new reference point smoothly as described in the LIP model in Eq. (4.10).

4.5. Summary

This chapter provided the formulations for physical and virtual interaction to bipedal robot balance and locomotion. With the distributed force sensing provided by robot skin, a robot can measure the interaction forces exerted by the terrain and the geometry of the interaction area. These measurements provide information on the walking metrics that the classic approach (ankle force-torque sensors) can not. State-the-art walking controllers cope with the missing information by making assumptions as full sole contact (for example [8, 188]) or by slowing down the walking pace applying fast exploratory motions over the footholds before transferring the weight to the landing foot.

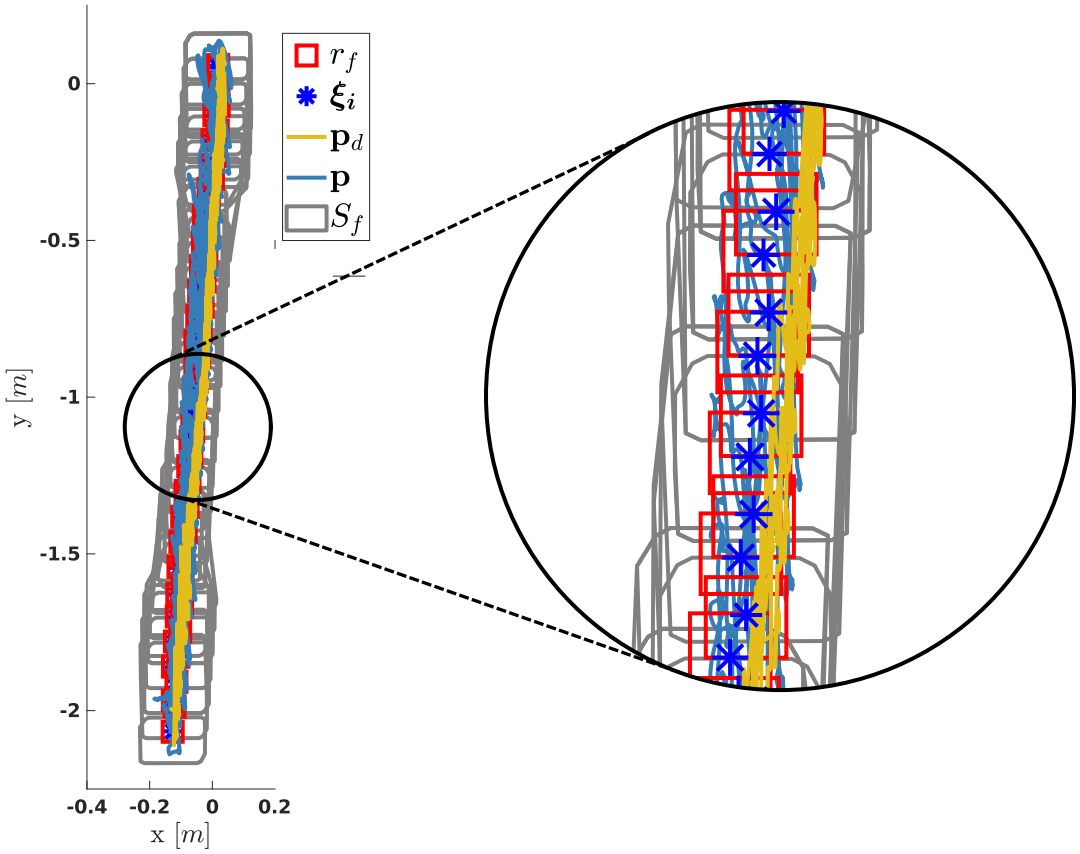

Figure 64 The H1 robot walking over a 12 cm beam with a deviated initial orientation. When the robot walks from the first platform to the beam, the supporting polygon constructed from tactile plantar feedback helps adjust the walking motions as described in Section 4.4.5, and at to constraint the reference ZMP in for the balance controller.

The formulations presented in this chapter merge the capabilities that plantar skin provides into bipedal robot balance and walking control. We revised how to find the ZMP from the plantar tactile information, which is the fundamental metric for equilibrium in most walking controllers. We investigated the capability of plantar skin to replace ankle force-torque sensors to measure the ZMP and the GRF with a side-by-side comparison of both feedbacks in a balance controller. Nevertheless, the plantar skin system must know the location of every taxel in the sole to estimate the ZMP.

In the experimental runs, we found that to find the ZMP, there is no need for precise calibration of the force cell in the taxels, as long as the sensitivities and sensing ranges of the taxels are uniform. The formulation of the ZMP (Eq. (4.21)) divides the product of the force and the location of the taxels by the vertical component of the resultant force, which is the largest component of the GRF. Therefore, in practice, the variations in the magnitude of the GRF are compensated when computing the ZMP. However, if we need to compute the GRF, proper calibration of the force cells will be required.

In Section 4.2.5, we introduce a new method to approximate the shape of the supporting polygon from plantar tactile information. In that method, we exploited the spatial distribution of the taxels over the sole, combined with the knowledge of the taxel geometry. In practice, the taxel geometry is given during the hardware design of the robot skin systems. Therefore, we can assume that the shape and size of the taxels are known. Our method applies to any taxel shape and size. Combining taxels of different shapes and sizes is not a problem, as long as the geometry of all the taxels is known. The accuracy of the supporting polygon approximation depends on the spatial resolution of the skin system. However, in practice, the plantar skin can have a coarse spatial resolution and still be functional when applied to bipedal robot balance and walking control as shown in the experiments of walking over partial footholds.

We used the proximity sensing modality of the plantar skin to preemptively estimate the ground reaction wrench and generate an ankle reaction during the swing motion of the single support phase of the walking cycle. The preemptive foot compliance modality introduced in Section 4.4.1 uses the proximity sensors of the taxels to generate a virtual reaction force that damps the landing motion and adapts the foot orientation to the terrain geometry. The damping of the landing motion reduces the magnitude of the impacts during walking. The experiments in Sections 4.4.1.2 and 4.4.1.3 show how the landing impact forces with PFC are reduced to 20%, compared to the landing impacts with no PFC. This also applies to unexpected obstacles encountered during walking. PFC anticipates the stopping of the swing motion to land softly when an increment in the terrain height is detected. In such cases, plantar skin provides information to either cancel and re-plan a stepping motion as shown in Section 4.3.2 or to step over the obstacle using its geometry to define constraints for the walking motions and balance control.

The direct supporting polygon acquisition right after foot landing enabled the adaptation of the walking motion during the double support phase of the walking cycle. The centroid of the polygon detected in the landing foot defines a new target position for the ZMP to continue walking. Then, we recalculate the walking motions to step over the new foothold, which can be smaller than the sole. We no longer require the assumption of full sole contact to compute the walking motions nor the reactions for balance. The adapted walking motions can be tracked using the supporting polygon as a constraint in the balance control. We improved the balancer modules of two different controllers using the supporting polygon in the ZMP tracking formulation. We validated the proposed method on two different full-sized humanoid robots running different software frameworks and walking controllers. The generality of the formulations in this thesis allowed the implementation of the plantar tactile feedback in both robots without requiring deep modifications in the walking controller. The formulations in this chapter enabled the walking controllers of both robots to walk over uneven terrain and step over partial footholds. Both controllers were designed for walking over flat ground, considering full sole contacts. In the last experiment in Section 4.4.5.3 the H1 robot continuously walked over a narrow beam without stopping to assess the terrain conditions. The robot adapted its walking motions to keep the balance and stay over the beam, constraining its compensatory motions within the geometry of the contacts measured by the plantar skin.

From the inspiration on human plantar skin and the practical evaluation done during the development of the formulations of this chapter, the minimum required features for plantar skin for bipedal robots can be listed as follows:

- The soles of the robot must be fully covered by skin.
- The position and shape of all the taxels in the skin must be known.
- The taxels of one foot must not saturate when holding the whole robot's weight.
- The taxels must provide force sensing modality.

While the items above are the minimum requirements for plantar sensing, it is also useful to include the proximity sensing modality in the taxels to enable PFC in the walking controllers.

In this thesis, the skin was mounted on the robots using 3D printed shoes which are a practical apparatus for plantar skin. The tactile shoes developed for the experiments of this chapter allow mounting plantar skin on a robot with a short preparation time. They also are easy to remove and require no permanent changes in the foot design of the robot. Furthermore, preparing tactile shoes requires only the knowledge of the external foot geometry to design the model to print. The contributions of this chapter explored the advantages that plantar sensing brings for bipedal robot balance and walking control as an alternative to ankle force-torque sensors or a complement to them providing the missing information about the foot-terrain interactions that ankle force-torque sensors cannot deliver.

5. Conclusion and Outlook

The goal of this thesis is to extend the capabilities of robots for physical interactions with the environment. For this purpose, we explored the use of robot skin that provides direct measurements of the interactions and additional insights into the environmental conditions. Robot skin systems are increasing their capabilities every year by including new sensing modalities, increasing the sensor resolution and operation range, reducing the size of the taxels, and improving the durability of the hardware designs. However, the fast development of these systems causes a bottleneck in the classic robot control techniques that cannot exploit all the new modalities of tactile feedback. Therefore, the control techniques must be continuously updated to handle the tactile information and develop closed-loop controllers that use these new modalities of feedback. To overcome this gap, this thesis presents the fundamentals to exploit multi-modal tactile feedback to enhance the versatility of physical interactions for robots.

Through the chapters of this thesis, we proposed a series of formulations to extract useful information from large amounts of tactile information to model physical interactions for control. The contributions of this thesis set a precedence to enable different modalities of body compliance control from alternative sensing modalities. The direct and virtual interaction task formulations presented in this thesis can be combined to fit the requirements of new applications for robots equipped with multi-modal sensory skin. We presented case studies where the tactile information was used to make higher-level decisions such as task priority rearrangements or step replanning in the context of biped walking.

Within all the forms of physical interaction, locomotion is one of the most important. Walking is paramount in the everyday life of human beings and animals. In this thesis, we expanded the formulations to use multi-modal tactile feedback in the complex process of biped locomotion. We presented methods to measure the interactions of the supporting contacts from plantar skin to acquire the metrics used in bipedal robot balance and walking controllers. The methods presented in this thesis substantially extend and complemented the formulations for balance and walking control to remove the assumption of full sole contact that is commonly taken due to the lack of geometric information on the supporting contacts.

5.1. Summary of Results and Contributions

Whole-body physical interaction control methods

We designed a series of tasks using the operational space formulation from Khatib and Sentis [131] that exploit the spatial distribution of force sensors in robot skins. The direct interaction task collects the measurements of all the taxels in a link of the kinematic chain and generates

joint torque reaction motions to minimize the contact forces. This thesis expanded the whole body interaction control framework of Dean et al. [4] by formulating other modalities of interaction and proposing a method to automatically activate/deactivate the interaction tasks from the tactile information. This improves the performance when running several simultaneous instances of interaction tasks together. The performance of the method was evaluated in the experiment in Section 3.2.4.1 which combines 13 instances of direct physical contact interaction tasks with 13 instances of proximity-based collision-avoidance virtual interaction tasks while standing on one leg with a supporting/balance task, and below all these tasks, with a lower priority, a full-rank CoM controller task. All these computations were made possible to be implemented in real-time the embedded computer inside the H1 robot.

Whole-body virtual interaction control methods from alternative sensing modalities

This thesis provides the formulations for generating interaction tasks from the additional information that robot skins deliver. This information includes the geometric localization of the contacts provided by the spatial distribution of the taxels in the skin and the additional sensing modalities aside from the force sensing included in the taxels (in this work, proximity, and temperature).

The geometric information on the contacts was used to formulate the pressure-driven body compliance behavior. This modality of physical interaction amplifies the forces when concentrated in a small area and damps the forces when distributed over large areas. This new tactile-based modality of physical interaction generates a behavior that cannot be implemented using the classic force-torque sensor approaches and provides a valuable component to generate combined whole-body behaviors for future applications.

This thesis also presented the formulations to generate interaction tasks from sensing modalities that do not imply a physical contact of the robot with the environment. As examples of this type of interaction, we presented virtual repellent tasks from distributed proximity sensors. This modality of virtual interactions allows manipulating the posture of a robot without touching it. This behavior can be applied when a robot must avoid contact with the environment. The repellent potential fields generated from the proximity sensor signals push away the robot links from any object in the environment providing a versatile whole-body collision-avoidance control. This includes operators, surrounding objects, and the other links of the robot.

Following the virtual interaction formulation, this thesis presented a temperature-driven body compliance modality that generates a virtual repulsive potential fields that drive away the robot's links from hot surfaces. This modality of body compliance can be applied in applications where a robot must operate close to hazard hot surfaces as the cooking scenario experiment in Section 3.3.2.1.

Whole-body behaviors combining physical and virtual interactions

This thesis presented two cases of body behaviors that use tactile information to make changes in the priorities of tasks. The mechanical nociception in Section 3.4.1 deactivates a task if the pressure-driven compliance task in a lower priority detects a potentially harmful concentration of forces. The intentional contact behavior presented in Section 3.4.2 rearranges the task priorities to escape from local minima when the collision-avoidance prevents an end-effector task from executing. The possibility of a direct measurement of physical interactions allows a robot to apply intentional contacts to the environment to modify it to clear the way for the end-effector. Aside from these two specific behaviors, the formulations in this thesis for direct and virtual interactions provide a practical framework to generate other modalities of body behaviors for future applications in robotics.

The examples presented in this thesis show how the environmental awareness that multimodal tactile feedback brings can be used to make higher-level decisions in robotic applications aside from enabling closed-loop physical interaction.

Plantar sensing modalities for biped balance and locomotion

This thesis presented a practical method to mount plantar skin on biped robots with mountable tactile shoes. With the information provided by plantar skin, we can locate the ZMP of a biped robot and construct the supporting polygon. We presented a method to find the convex hull of the sole contacts using the tactile information and the geometric parameters of the taxels. We compared the ZMP acquired from robot skin to the classic method using ankle force-torque sensors. Plantar skin is capable of serving as the main feedback in balance controllers with similar results as ankle force-torque sensors, and at the same time provide geometric information of the terrain.

Preemptive foot compliance

With the additional sensing modality of proximity to the terrain in plantar skin, this thesis developed the Preemptive Foot Compliance (PFC) modality for the swing leg in the single support phase of the walking cycle. PFC adapts the foot orientation using the virtual repulsive force formulation developed for the virtual interactions to match the terrain inclination before hitting the ground. This preemptive motion helps reduce the impact at foot landing and thus reduces the disturbance forces produced by anticipated contacts. This modality is a good complement to any ankle impedance controller, reducing the required reaction motion to adopt the foothold geometry with the sole. Additionally, the virtual repulsive force suppresses 80% of the landing impact force on average when walking over flat ground.

Constrained balance control using plantar skin

This thesis presented two new methods that constraint the ZMP reference position within the geometry of the supporting polygon constructed by robot skin.

This thesis removed the assumption of full-sole contact commonly made in walking controllers [127, 148, 6] providing a method to construct the actual supporting polygon from plantar tactile information. As the first example of this principle, the bounding box of the supporting polygon was used to redefine the constraints of the ZMP distribution QP problem in [8]. With the generalization of the friction cone constraints presented Section 4.4.4 in this work, the open-source controller [127] was capable of keeping the balance while stepping over partial footholds as presented in Section 4.4.5.1.

This thesis also presented an algorithm to constraint the adjusted reference ZMP from the DCM tracking controllers inside the supporting polygon constructed from plantar skin. This change was applied in a DCM-ZMP walking controller that was also capable of stepping over partial footholds with the contact information acquired right at the foot landing. This removes completely all the assumptions of the contact geometry (even the bounding box requirement for the experiment in Section 4.4.5.1) by directly using the supporting polygon to constraint the adjustments of the reference ZMP done by balance controllers.

Walking motion adaptation from plantar tactile feedback

This thesis proposed a new method to modify online the walking motions to adapt to the actual contact geometry with the tactile information acquired right at the foot landing. Our method re-plans the VRPs and DCM waypoints to the center of the supporting polygon measured immediately after foot touchdown. With this method, a robot is capable of continuously walking over partial footholds while keeping the reaction motions for balance within the supporting polygon.

The new method was evaluated in an experiment where a robot walked over a narrow beam in a scenario inspired by construction sites. In state-of-the-art walking controllers without plantar tactile feedback, a robot must apply exploratory motions to map the terrain geometry at every step, slowing down the walking motion. This thesis advanced the state-of-the-art by setting the formulations for plantar tactile feedback that provide the geometric information of the terrain immediately after foot contact, which allows adapting the walking reference motions within one update cycle of the walking control. Therefore, with the proposed method, no stops or exploratory motions are required to continuously walk over partial footholds.

5.2. Outlook

Based on the experiences gained and the evaluations presented in this work, some ideas emerged that are worth exploring in future works.

Distributed sensing for virtual interactions is a promising idea to give awareness to robots. The next logical step in this direction is to include even more sensing modalities into the robot skins to enhance the reactive control of robots, especially in critical situations. For example, humidity, radiation, or chemical detectors can help a robot detect released substances in cooperative scenarios with human workers. Multi-modal body behaviors as the ones presented in this work can improve the performance in hazardous scenarios where robots can help improve the working conditions or prevent damages to the health of human workers. The pressure-driven body compliance in this work can be applied, for example, for manipulating human bodies in health care robots. In such a sensitive application, the interaction forces can be as high as the weight of a human body. However, they should not be concentrated in small areas because applying high pressures on a human body can cause injuries in the skin or in the soft tissues of the body.

The set of interaction modalities and the priority of the tasks used to realize the two whole-body behaviors presented in this work were selected and assigned by a person from observations of human behavior in real scenarios. However, the realization of new behavior could be generalized by semantic relations from human actions. It would be worth exploring the possibility of developing a general method to select interaction modalities and task priorities from application description semantics to automatize the generation of whole-body behaviors.

Plantar tactile feedback is also a promising idea that allows the design of new control techniques for robot balance and walking. In this work, the tactile information was used to modify the kinematics of the walking motion. However, a drastic change in the walking pattern should also represent a change in the timing of the walking cycle. Plantar feedback can help coordinate the timing of the walking cycle similarly as plantar skin helps regulate the timing of the muscular reflexes in human walking.

As the plantar skin provides additional information for balance and control, the same principle can be extended to the whole body. A robot with a whole-body skin system as the H1 robot used in this work can exploit the sensing modalities of the skin on the hands, the arms, or the torso for balance and locomotion. The community of humanoid robotics has proposed control techniques for multi-limb locomotion that can profit from the tactile information from robot skins. For example, the intentional contact behavior presented in this work can be applied to generate motions to look for supporting surfaces with the hands. Then, once defined upper body supporting contacts and their geometry, the tactile feedback can be used for generalized stability criteria as the 3D polyhedron in [190] or the projected ZMP support area in [191].

Bibliography

[1] Philipp Mittendorfer and Gordon Cheng. Integrating discrete force cells into multi-modal artificial skin. In *2012 12th IEEE-RAS International Conference on Humanoid Robots (Humanoids 2012)*, pages 847–852. IEEE, 2012.

[2] Emmanuel Dean-Leon, J. Rogelio Guadarrama-Olvera, Florian Bergner, and Gordon Cheng. Whole-body active compliance control for humanoid robots with robot skin. In *IEEE International Conference on Robotics and Automation (ICRA)*, pages 5404–1510, 2019.

[3] Kenji Kaneko, Mitsuharu Morisawa, Shuuji Kajita, Shin'ichiro Nakaoka, Takeshi Sakaguchi, Rafael Cisneros, and Fumio Kanehiro. Humanoid robot hrp-2kai—improvement of hrp-2 towards disaster response tasks. In *2015 IEEE-RAS 15th International Conference on Humanoid Robots (Humanoids)*, pages 132–139. IEEE, 2015.

[4] Emmanuel Dean-Leon, J Rogelio Guadarrama-Olvera, Florian Bergner, and Gordon Cheng. Whole-body active compliance control for humanoid robots with robot skin. In *2019 International Conference on Robotics and Automation (ICRA)*, pages 5404–5410. IEEE, 2019.

[5] Gordon Cheng, Emmanuel Dean-Leon, Florian Bergner, Julio Rogelio Guadarrama Olvera, Quentin Leboutet, and Philipp Mittendorfer. A comprehensive realization of robot skin: Sensors, sensing, control, and applications. *Proceedings of the IEEE*, 107(10):2034–2051, 2019.

[6] Johannes Englsberger, Christian Ott, Máximo A Roa, Alin Albu-Schäffer, and Gerhard Hirzinger. Bipedal walking control based on capture point dynamics. In *2011 IEEE/RSJ International Conference on Intelligent Robots and Systems*, pages 4420–4427. IEEE, 2011.

[7] Philipp Mittendorfer and Gordon Cheng. Humanoid multi-modal tactile sensing modules. *IEEE Transactions on Robotics*, 27(3):401–410, 2011.

[8] Stéphane Caron, Quang-Cuong Pham, and Yoshihiko Nakamura. Stability of surface contacts for humanoid robots: Closed-form formulae of the contact wrench cone for rectangular support areas. In *2015 IEEE International Conference on Robotics and Automation (ICRA)*, pages 5107–5112. IEEE, 2015.

[9] Tamim Asfour, Kristian Regenstein, Pedram Azad, J Schroder, Alexander Bierbaum, Nikolaus Vahrenkamp, and Rüdiger Dillmann. Armar-iii: An integrated humanoid plat-

form for sensory-motor control. In *2006 6th IEEE-RAS international conference on humanoid robots*, pages 169–175. IEEE, 2006.

[10] Koichi Nishiwaki, James Kuffner, Satoshi Kagami, Masayuki Inaba, and Hirochika Inoue. The experimental humanoid robot h7: a research platform for autonomous behaviour. *Philosophical Transactions of the Royal Society A: Mathematical, Physical and Engineering Sciences*, 365(1850):79–107, 2006.

[11] Gordon Cheng, Sang-Ho Hyon, Jun Morimoto, Aleš Ude, Joshua G Hale, Glenn Colvin, Wayco Scroggin, and Stephen C Jacobsen. Cb: A humanoid research platform for exploring neuroscience. *Advanced Robotics*, 21(10):1097–1114, 2007.

[12] Shuuji Kajita, Hirohisa Hirukawa, Kensuke Harada, and Kazuhito Yokoi. *Introduction to humanoid robotics*, volume 101. Springer, 2014.

[13] Tamim Asfour, Mirko Waechter, Lukas Kaul, Samuel Rader, Pascal Weiner, Simon Ottenhaus, Raphael Grimm, You Zhou, Markus Grotz, and Fabian Paus. Armar-6: a high-performance humanoid for human-robot collaboration in real-world scenarios. *IEEE Robotics & Automation Magazine*, 26(4):108–121, 2019.

[14] Grzegorz Ficht and Sven Behnke. Bipedal humanoid hardware design: a technology review. *Current Robotics Reports*, 2(2):201–210, 2021.

[15] Hiroyasu Iwata and Shigeki Sugano. Whole-body covering tactile interface for human robot coordination. In *Proceedings 2002 IEEE International Conference on Robotics and Automation (Cat. No. 02CH37292)*, volume 4, pages 3818–3824. IEEE, 2002.

[16] Francesco Nori, Silvio Traversaro, Jorhabib Eljaik, Francesco Romano, Andrea Del Prete, and Daniele Pucci. icub whole-body control through force regulation on rigid non-coplanar contacts. *Frontiers in Robotics and AI*, 2:6, 2015.

[17] Sami Haddadin, Alin Albu-Schäffer, and Gerd Hirzinger. Safety evaluation of physical human-robot interaction via crash-testing. In *Robotics: Science and systems*, volume 3, pages 217–224. Citeseer, 2007.

[18] Orhan Agcaoglu, Shamil Aliyev, Halit Eren Taskin, Sricharan Chalikonda, Matthew Walsh, Meagan M Costedio, Matthew Kroh, Tomasz Rogula, Bipan Chand, Emre Gorgun, et al. Malfunction and failure of robotic systems during general surgical procedures. *Surgical endoscopy*, 26(12):3580–3583, 2012.

[19] Agostino De Santis, Bruno Siciliano, Alessandro De Luca, and Antonio Bicchi. An atlas

of physical human–robot interaction. *Mechanism and Machine Theory*, 43(3):253–270, 2008.

[20] Paolo Dario, Eugenio Guglielmelli, Benedetto Allotta, and Maria Chiara Carrozza. Robotics for medical applications. *IEEE Robotics & Automation Magazine*, 3(3):44–56, 1996.

[21] G Dogangil, BL Davies, and F Rodriguez y Baena. A review of medical robotics for minimally invasive soft tissue surgery. *Proceedings of the Institution of Mechanical Engineers, Part H: Journal of Engineering in Medicine*, 224(5):653–679, 2010.

[22] Toshiharu Mukai, Shinya Hirano, Hiromichi Nakashima, Yo Kato, Yuki Sakaida, Shijie Guo, and Shigeyuki Hosoe. Development of a nursing-care assistant robot riba that can lift a human in its arms. In *2010 IEEE/RSJ International Conference on Intelligent Robots and Systems*, pages 5996–6001. IEEE, 2010.

[23] Emmanuel Dean-Leon, Karinne Ramirez-Amaro, Florian Bergner, Ilya Dianov, Pablo Lanillos, and Gordon Cheng. Robotic technologies for fast deployment of industrial robot systems. In *IECON 2016-42nd Annual Conference of the IEEE Industrial Electronics Society*, pages 6900–6907. IEEE, 2016.

[24] Birgit Graf, Matthias Hans, and Rolf D Schraft. Care-o-bot ii—development of a next generation robotic home assistant. *Autonomous robots*, 16(2):193–205, 2004.

[25] Kimitoshi Yamazaki, Ryohei Ueda, Shunichi Nozawa, Mitsuharu Kojima, Kei Okada, Kiyoshi Matsumoto, Masaru Ishikawa, Isao Shimoyama, and Masayuki Inaba. Home-assistant robot for an aging society. *Proceedings of the IEEE*, 100(8):2429–2441, 2012.

[26] Satoru Satake, Takayuki Kanda, Dylan F Glas, Michita Imai, Hiroshi Ishiguro, and Norihiro Hagita. How to approach humans? strategies for social robots to initiate interaction. In *Proceedings of the 4th ACM/IEEE international conference on Human robot interaction*, pages 109–116, 2009.

[27] Masahiro Shiomi, Aya Nakata, Masayuki Kanbara, and Norihiro Hagita. A hug from a robot encourages prosocial behavior. In *2017 26th IEEE international symposium on robot and human interactive communication (RO-MAN)*, pages 418–423. IEEE, 2017.

[28] Aaron Steinfeld, Terrence Fong, David Kaber, Michael Lewis, Jean Scholtz, Alan Schultz, and Michael Goodrich. Common metrics for human-robot interaction. In *Proceedings of the 1st ACM SIGCHI/SIGART conference on Human-robot interaction*, pages 33–40. ACM, 2006.

[29] Sang-Ho Hyon, Joshua G Hale, and Gordon Cheng. Full-body compliant human–humanoid interaction: balancing in the presence of unknown external forces. *IEEE Transactions on Robotics*, 23(5):884–898, 2007.

[30] Matthew T Mason. Compliance and force control for computer controlled manipulators. *IEEE Transactions on Systems, Man, and Cybernetics*, 11(6):418–432, 1981.

[31] Daniel E Whitney. Historical perspective and state of the art in robot force control. *The International Journal of Robotics Research*, 6(1):3–14, 1987.

[32] Rainer Bischoff, Johannes Kurth, Günter Schreiber, Ralf Koeppe, Alin Albu-Schäffer, Alexander Beyer, Oliver Eiberger, Sami Haddadin, Andreas Stemmer, Gerhard Grunwald, et al. The kuka-dlr lightweight robot arm-a new reference platform for robotics research and manufacturing. In *ISR 2010 (41st international symposium on robotics) and ROBOTIK 2010 (6th German conference on robotics)*, pages 1–8. VDE, 2010.

[33] Sami Haddadin, Alin Albu-Schaffer, Alessandro De Luca, and Gerd Hirzinger. Collision detection and reaction: A contribution to safe physical human-robot interaction. In *Intelligent Robots and Systems, 2008. IROS 2008. IEEE/RSJ International Conference on*, pages 3356–3363. IEEE, 2008.

[34] Gill A Pratt and Matthew M Williamson. Series elastic actuators. In *Proceedings 1995 IEEE/RSJ International Conference on Intelligent Robots and Systems. Human Robot Interaction and Cooperative Robots*, volume 1, pages 399–406. IEEE, 1995.

[35] Haoyong Yu, Sunan Huang, Nitish V Thakor, Gong Chen, Siew-Lok Toh, Manolo Sta Cruz, Yassine Ghorbel, and Chi Zhu. A novel compact compliant actuator design for rehabilitation robots. In *Rehabilitation Robotics (ICORR), 2013 IEEE International Conference on*, pages 1–6. IEEE, 2013.

[36] Bram Vanderborght, Nikos G Tsagarakis, Ronald Van Ham, Ivar Thorson, and Darwin G Caldwell. Maccepa 2.0: compliant actuator used for energy efficient hopping robot chobino1d. *Autonomous Robots*, 31(1):55–65, 2011.

[37] Vladimir J Lumelsky and Edward Cheung. Real-time collision avoidance in teleoperated whole-sensitive robot arm manipulators. *IEEE Transactions on Systems, Man, and Cybernetics*, 23(1):194–203, 1993.

[38] Thomas Wosch and Wendelin Feiten. Reactive motion control for human-robot tactile interaction. In *Robotics and Automation, 2002. Proceedings. ICRA'02. IEEE International Conference on*, volume 4, pages 3807–3812. IEEE, 2002.

[39] Oliver Kerpa, Karsten Weiss, and Heinz Worn. Development of a flexible tactile sensor system for a humanoid robot. In *Intelligent Robots and Systems, 2003.(IROS 2003). Proceedings. 2003 IEEE/RSJ International Conference on*, volume 1, pages 1–6. IEEE, 2003.

[40] Takayuki Hoshi and Hiroyuki Shinoda. Robot skin based on touch-area-sensitive tactile element. In *Proceedings 2006 IEEE International Conference on Robotics and Automation, 2006. ICRA 2006.*, pages 3463–3468. IEEE, 2006.

[41] Emmanuel Dean-Leon, Florian Bergner, Karinne Ramirez-Amaro, and Gordon Cheng. From multi-modal tactile signals to a compliant control. In *2016 IEEE-RAS 16th International Conference on Humanoid Robots (Humanoids)*, pages 892–898. IEEE, 2016.

[42] Ravinder S Dahiya, Giorgio Metta, Maurizio Valle, and Giulio Sandini. Tactile sensing-from humans to humanoids. *IEEE Trans. Robotics*, 26(1):1–20, 2010.

[43] Ravinder Dahiya. E-skin: From humanoids to humans. *Proceedings of the IEEE*, 107(2):247–252, 2019.

[44] Andrea Del Prete, Simone Denei, Lorenzo Natale, Fulvio Mastrogiovanni, Francesco Nori, Giorgio Cannata, and Giorgio Metta. Skin spatial calibration using force/torque measurements. In *2011 IEEE/RSJ International Conference on Intelligent Robots and Systems*, pages 3694–3700. IEEE, 2011.

[45] Philipp Mittendorfer, Emmanuel Dean, and Gordon Cheng. 3d spatial self-organization of a modular artificial skin. In *2014 IEEE/RSJ International Conference on Intelligent Robots and Systems*, pages 3969–3974. IEEE, 2014.

[46] Florian Bergner, Emmanuel Dean-Leon, and Gordon Cheng. Design and realization of an efficient large-area event-driven e-skin. *Sensors*, 20(7):1965, 2020.

[47] Pedro Silva Girão, Pedro Miguel Pinto Ramos, Octavian Postolache, and José Miguel Dias Pereira. Tactile sensors for robotic applications. *Measurement*, 46(3):1257–1271, 2013.

[48] Guanyu Liu, Qiulin Tan, Hairong Kou, Lei Zhang, Jinqi Wang, Wen Lv, Helei Dong, and Jijun Xiong. A flexible temperature sensor based on reduced graphene oxide for robot skin used in internet of things. *Sensors*, 18(5):1400, 2018.

[49] Jim L Novak and John T Feddema. A capacitance-based proximity sensor for whole arm obstacle avoidance. Technical report, Sandia National Labs., Albuquerque, NM (United States), 1991.

[50] Satoshi Tsuji and Teruhiko Kohama. Proximity skin sensor using time-of-flight sensor for human collaborative robot. *IEEE Sensors Journal*, 19(14):5859–5864, 2019.

[51] Liming Miao, Ji Wan, Yu Song, Hang Guo, Haotian Chen, Xiaoliang Cheng, and Haixia Zhang. Skin-inspired humidity and pressure sensor with a wrinkle-on-sponge structure. *ACS applied materials & interfaces*, 11(42):39219–39227, 2019.

[52] Ebrahim Mattar. A survey of bio-inspired robotics hands implementation: New directions in dexterous manipulation. *Robotics and Autonomous Systems*, 61(5):517–544, 2013.

[53] Mohsen Kaboli, Kunpeng Yao, and Gordon Cheng. Tactile-based manipulation of deformable objects with dynamic center of mass. In *2016 IEEE-RAS 16th International Conference on Humanoid Robots (Humanoids)*, pages 752–757. IEEE, 2016.

[54] Quentin Leboutet, J Rogelio Guadarrama-Olvera, Florian Bergner, and Gordon Cheng. Second-order kinematics for floating-base robots using the redundant acceleration feedback of an artificial sensory skin. In *2020 IEEE International Conference on Robotics and Automation (ICRA)*, pages 4687–4694. IEEE, 2020.

[55] Taisuke Kobayashi, Emmanuel Dean-Leon, Julio Rogelio Guadarrama-Olvera, Florian Bergner, and Gordon Cheng. Multi-contacts force-reactive walking control during physical human-humanoid interaction. In *2019 IEEE-RAS 19th International Conference on Humanoid Robots (Humanoids)*, pages 33–39. IEEE, 2019.

[56] J Rogelio Guadarrama Olvera, Emmanuel Dean Leon, Florian Bergner, and Gordon Cheng. Plantar tactile feedback for biped balance and locomotion on unknown terrain. *International Journal of Humanoid Robotics*, 17(01):1950036, 2020.

[57] Julio Rogelio Guadarrama-Olvera, Emmanuel Dean-Leon, Florian Bergner, and Gordon Cheng. Pressure-driven body compliance using robot skin. *IEEE Robotics and Automation Letters*, 4(4):4418–4423, 2019.

[58] Oussama Khatib. Real-time obstacle avoidance for manipulators and mobile robots. *The international journal of robotics research*, 5(1):90–98, 1986.

[59] Pradeep Khosla and Richard Volpe. Superquadric artificial potentials for obstacle avoidance and approach. In *Robotics and Automation, 1988. Proceedings., 1988 IEEE International Conference on*, pages 1778–1784. IEEE, 1988.

[60] Agostino De Santis, Alin Albu-Schaffer, Christian Ott, Bruno Siciliano, and Gerd Hirzinger. The skeleton algorithm for self-collision avoidance of a humanoid manip-

ulator. In *2007 IEEE/ASME international conference on advanced intelligent mechatronics*, pages 1–6. IEEE, 2007.

[61] Fumi Seto, Kazuhiro Kosuge, and Yasuhisa Hirata. Self-collision avoidance motion control for human robot cooperation system using robe. In *2005 IEEE/RSJ International Conference on Intelligent Robots and Systems*, pages 3143–3148. IEEE, 2005.

[62] Masahiko Mikawa, Koichi Yoshida, Mizuki Tanno, and Michito Matsumoto. Vision-based redundancy control of robot manipulators for obstacle avoidance. In *Proceedings of the IECON'97 23rd International Conference on Industrial Electronics, Control, and Instrumentation (Cat. No. 97CH36066)*, volume 3, pages 1373–1378. IEEE, 1997.

[63] S Higashi, S Komada, M Ishida, and T Hori. Obstacle avoidance of redundant manipulators on visual servo system using estimated image features. In *AMC'98-Coimbra. 1998 5th International Workshop on Advanced Motion Control. Proceedings (Cat. No. 98TH8354)*, pages 165–170. IEEE, 1998.

[64] Haobin Shi, Jialin Chen, Wei Pan, Kao-Shing Hwang, and Yi-Yun Cho. Collision avoidance for redundant robots in position-based visual servoing. *IEEE Systems Journal*, 13(3):3479–3489, 2018.

[65] Edward Cheung and VLADIMIR Lumelsky. Motion planning for robot arm manipulators with proximity sensing. In *Proceedings. 1988 IEEE International Conference on Robotics and Automation*, pages 740–745. IEEE, 1988.

[66] JR Llata, EG Sarabia, J Arce, and JP Oria. Fuzzy controller for obstacle avoidance in robotic manipulators using ultrasonic sensors. In *AMC'98-Coimbra. 1998 5th International Workshop on Advanced Motion Control. Proceedings (Cat. No. 98TH8354)*, pages 647–652. IEEE, 1998.

[67] Nicolas Mansard, Olivier Stasse, Paul Evrard, and Abderrahmane Kheddar. A versatile generalized inverted kinematics implementation for collaborative working humanoid robots: The stack of tasks. In *Advanced Robotics, 2009. ICAR 2009. International Conference on*, pages 1–6. IEEE, 2009.

[68] Alexander Dietrich, Christian Ott, and Alin Albu-Schäffer. An overview of null space projections for redundant, torque-controlled robots. *The International Journal of Robotics Research*, 34(11):1385–1400, 2015.

[69] Oussama Kanoun, Florent Lamiraux, and Pierre-Brice Wieber. Kinematic control of redundant manipulators: Generalizing the task-priority framework to inequality task. *IEEE Transactions on Robotics*, 27(4):785–792, 2011.

[70] Adrien Escande, Nicolas Mansard, and Pierre-Brice Wieber. Hierarchical quadratic programming: Fast online humanoid-robot motion generation. *The International Journal of Robotics Research*, page 0278364914521306, 2014.

[71] Alessandro De Luca, Alin Albu-Schaffer, Sami Haddadin, and Gerd Hirzinger. Collision detection and safe reaction with the dlr-iii lightweight manipulator arm. In *Intelligent Robots and Systems, 2006 IEEE/RSJ International Conference on*, pages 1623–1630. IEEE, 2006.

[72] Akihiko Nagakubo, Yasuo Kuniyoshi, and Gordon Cheng. The etl-humanoid system—a high-performance full-body humanoid system for versatile real-world interaction. *Advanced robotics*, 17(2):149–164, 2003.

[73] Alexandros Kouris, Fotios Dimeas, and Nikos Aspragathos. A frequency domain approach for contact type distinction in human-robot collaboration. *IEEE robotics and automation letters*, 3(2):720–727, 2018.

[74] J Rogelio Guadarrama-Olvera, Emmanuel Dean, and Gordon Cheng. Using intentional contact to achieve tasks in tight environments. In *Robotics and Automation (ICRA), 2017 IEEE International Conference on*, pages 1000–1005. IEEE, 2017.

[75] Tapomayukh Bhattacharjee, Joshua Wade, Yash Chitalia, and Charles C Kemp. Data-driven thermal recognition of contact with people and objects. In *Haptics Symposium (HAPTICS), 2016 IEEE*, pages 297–304. IEEE, 2016.

[76] Roberto Calandra, Serena Ivaldi, Marc Peter Deisenroth, et al. Learning torque control in presence of contacts using tactile sensing from robot skin. In *2015 IEEE-RAS 15th International Conference on Humanoid Robots (Humanoids)*, pages 690–695. IEEE, 2015.

[77] Agostino De Santis, Vincenzo Lippiello, Bruno Siciliano, and Luigi Villani. Human-robot interaction control using force and vision. In *Advances in Control Theory and Applications*, pages 51–70. Springer, 2007.

[78] Emanuele Magrini, Fabrizio Flacco, and Alessandro De Luca. Estimation of contact forces using a virtual force sensor. In *Intelligent Robots and Systems (IROS 2014), 2014 IEEE/RSJ International Conference on*, pages 2126–2133. IEEE, 2014.

[79] Carlo Bagnato, Atsushi Takagi, and Etienne Burdet. Artificial nociception and motor responses to pain, for humans and robots. In *Engineering in Medicine and Biology Society (EMBC), 2015 37th Annual International Conference of the IEEE*, pages 7402–7405. IEEE, 2015.

[80] Agnese Augello, Ignazio Infantino, Umberto Maniscalco, Giovanni Pilato, and Filippo Vella. The effects of soft somatosensory system on the execution of robotic tasks. In *2017 First IEEE International Conference on Robotic Computing (IRC)*, pages 14–21. IEEE, 2017.

[81] Fumiya Iida and Simon Bovet. *Learning Legged Locomotion*, pages 21–33. Springer London, London, 2009.

[82] Dimitrios Kanoulas, Chengxu Zhou, Anh Nguyen, Georgios Kanoulas, Darwin G Caldwell, and Nikos G Tsagarakis. Vision-based foothold contact reasoning using curved surface patches. In *Humanoid Robotics (Humanoids), 2017 IEEE-RAS 17th International Conference on*, pages 121–128. IEEE, 2017.

[83] Scott Kuindersma, Robin Deits, Maurice Fallon, Andrés Valenzuela, Hongkai Dai, Frank Permenter, Twan Koolen, Pat Marion, and Russ Tedrake. Optimization-based locomotion planning, estimation, and control design for the atlas humanoid robot. *Autonomous Robots*, 40(3):429–455, 2016.

[84] Yisoo Lee, Hosang Lee, Soonwook Hwang, and Jaeheung Park. Terrain edge detection for biped walking robots using active sensing with vcop-position hybrid control. *Robotics and Autonomous Systems*, 96:41–57, 2017.

[85] Mitsuharu Morisawa, Shuuji Kajita, Fumio Kanehiro, Kenji Kaneko, Kanako Miura, and Kazuhiro Yokoi. Balance control based on capture point error compensation for biped walking on uneven terrain. In *Humanoid Robots (Humanoids), 2012 12th IEEE-RAS International Conference on*, pages 734–740. IEEE, 2012.

[86] Jung-Yup Kim, Ill-Woo Park, and Jun-Ho Oh. Walking control algorithm of biped humanoid robot on uneven and inclined floor. *Journal of Intelligent and Robotic Systems*, 48(4):457–484, 2007.

[87] Zhibin Li, Chengxu Zhou, Nikos Tsagarakis, and Darwin Caldwell. Compliance control for stabilizing the humanoid on the changing slope based on terrain inclination estimation. *Autonomous Robots*, 40(6):955–971, 2016.

[88] Majid Khadiv, S Ali A Moosavian, Aghil Yousefi-Koma, Hessam Maleki, and Majid Sadedel. Online adaptation for humanoids walking on uncertain surfaces. *Proceedings of the Institution of Mechanical Engineers, Part I: Journal of Systems and Control Engineering*, 231(4):245–258, 2017.

[89] Shinya Aoi and Kazuo Tsuchiya. Stability analysis of a simple walking model driven

by an oscillator with a phase reset using sensory feedback. *IEEE Transactions on robotics*, 22(2):391–397, 2006.

[90] Robert J Griffin, Georg Wiedebach, Stephen McCrory, Sylvain Bertrand, Inho Lee, and Jerry Pratt. Footstep planning for autonomous walking over rough terrain. In *2019 IEEE-RAS 19th International Conference on Humanoid Robots (Humanoids)*, pages 9–16. IEEE, 2019.

[91] Christian Hubicki, Jesse Grimes, Mikhail Jones, Daniel Renjewski, Alexander Spröwitz, Andy Abate, and Jonathan Hurst. Atrias: Design and validation of a tether-free 3d-capable spring-mass bipedal robot. *The International Journal of Robotics Research*, 35(12):1497–1521, 2016.

[92] Kirill Van Heerden and Atsuo Kawamura. Biped robot position control with stability-based ground reaction force and velocity constraints. *IEEJ Journal of Industry Applications*, 2(1):30–39, 2013.

[93] Felix Sygulla and Daniel Rixen. A force-control scheme for biped robots to walk over uneven terrain including partial footholds. *International Journal of Advanced Robotic Systems*, 17(1):1729881419897472, 2020.

[94] Georg Wiedebach, Sylvain Bertrand, Tingfan Wu, Luca Fiorio, Stephen McCrory, Robert Griffin, Francesco Nori, and Jerry Pratt. Walking on partial footholds including line contacts with the humanoid robot atlas. In *Humanoid Robots (Humanoids), 2016 IEEE-RAS 16th International Conference on*, pages 1312–1319. IEEE, 2016.

[95] George Mesesan, Johannes Englsberger, Gianluca Garofalo, Christian Ott, and Alin Albu-Schäffer. Dynamic walking on compliant and uneven terrain using dcm and passivity-based whole-body control. In *2019 IEEE-RAS 19th International Conference on Humanoid Robots (Humanoids)*, pages 25–32. IEEE, 2019.

[96] Miomir Vukobratovic and Davor Juricic. Contribution to the synthesis of biped gait. *IEEE Transactions on Biomedical Engineering*, (1):1–6, 1969.

[97] Miomir Vukobratović and Branislav Borovac. Zero-moment point— thirty five years of its life. *International journal of humanoid robotics*, 1(01):157–173, 2004.

[98] Lewis Michael Nashner. *Sensory feedback in human posture control.* PhD thesis, Massachusetts Institute of Technology, 1970.

[99] Frances A Hellebrandt. Standing as a geotropic reflex: the mechanism of the asyn-

chronous rotation of motor units. *American Journal of Physiology-Legacy Content*, 121(2):471–474, 1938.

[100] Arash Mahboobin, Patrick J Loughlin, Mark S Redfern, Stuart O Anderson, Christopher G Atkeson, and Jessica K Hodgins. Sensory adaptation in human balance control: lessons for biomimetic robotic bipeds. *Neural Networks*, 21(4):621–627, 2008.

[101] J Timothy Inglis, Paul M Kennedy, Cari Wells, and Romeo Chua. The role of cutaneous receptors in the foot. In *Sensorimotor control of movement and posture*, pages 111–117. Springer, 2002.

[102] WHSC Heyd. *Der Tastsinn der Fusssohle als Aequilibrirungsmittel des Körpers beim Stehen*. H. Laupp, 1862.

[103] EJ Orma. The effects of cooling the feet and closing the eyes on standing equilibrium. different patterns of standing equilibrium in young adult men and women. *Acta Physiologica Scandinavica*, 38(3-4):288–297, 1957.

[104] JH Rogers. Romberg and his test. *The Journal of Laryngology & Otology*, 94(12):1401–1404, 1980.

[105] MÅNs Magnusson, Håkan Enbom, Rolf Johansson, and Joakim Wiklund. Significance of pressor input from the human feet in lateral postural control: The effect of hypothermia on galvanically induced body-sway. *Acta oto-laryngologica*, 110(3-4):321–327, 1990.

[106] Stephen D Perry, William E McIlroy, and Brian E Maki. The role of plantar cutaneous mechanoreceptors in the control of compensatory stepping reactions evoked by unpredictable, multi-directional perturbation. *Brain research*, 877(2):401–406, 2000.

[107] Henry Gray. *Anatomy of the human body*, volume 8. Lea & Febiger, 1878.

[108] Mats Trulsson. Mechanoreceptive afferents in the human sural nerve. *Experimental Brain Research*, 137(1):111–116, 2001.

[109] J Duysens, AAM Tax, S Nawijn, W Berger, T Prokop, and E Altenmüller. Gating of sensation and evoked potentials following foot stimulation during human gait. *Experimental brain research*, 105(3):423–431, 1990.

[110] Jaynie F Yang and Richard B Stein. Phase-dependent reflex reversal in human leg muscles during walking. *Journal of Neurophysiology*, 63(5):1109–1117, 1990.

[111] Bart MH Van Wezel, Frans AM Ottenhoff, and Jacques Duysens. Dynamic control of location-specific information in tactile cutaneous reflexes from the foot during human walking. *Journal of Neuroscience*, 17(10):3804–3814, 1997.

[112] Makoto Shimojo, Takuma Araki, Aigou Ming, and Masatoshi Ishikawa. A zmp sensor for a biped robot. In *Proceedings 2006 IEEE International Conference on Robotics and Automation, 2006. ICRA 2006.*, pages 1200–1205. IEEE, 2006.

[113] Kitti Suwanratchatamanee, Mitsuharu Matsumoto, and Shuji Hashimoto. A simple tactile sensing foot for humanoid robot and active ground slope recognition. In *2009 IEEE International Conference on Mechatronics*, pages 1–6. IEEE, 2009.

[114] Young-Dae Hong and Jong-Hwan Kim. 3-d command state-based modifiable bipedal walking on uneven terrain. *IEEE/ASME Transactions on Mechatronics*, 18(2):657–663, 2013.

[115] Mark A Hoepflinger, C David Remy, Marco Hutter, Luciano Spinello, and Roland Siegwart. Haptic terrain classification for legged robots. In *Robotics and Automation (ICRA), 2010 IEEE International Conference on*, pages 2828–2833. IEEE, 2010.

[116] Gen-ichiro Kinoshita, Tomonori Kimura, and Makoto Shimojo. Dynamic sensing experiments of reaction force distributions on the sole of a walking humanoid robot. In *Proceedings 2003 IEEE/RSJ International Conference on Intelligent Robots and Systems (IROS 2003)(Cat. No. 03CH37453)*, volume 2, pages 1413–1418. IEEE, 2003.

[117] Kristin Fondahl, Daniel Kuehn, Frank Beinersdorf, Felix Bernhard, Felix Grimminger, Moritz Schilling, Tobias Stark, and Frank Kirchner. An adaptive sensor foot for a bipedal and quadrupedal robot. In *2012 4th IEEE RAS & EMBS International Conference on Biomedical Robotics and Biomechatronics (BioRob)*, pages 270–275. IEEE, 2012.

[118] Youhei Takahashi, Koichi Nishiwaki, Satoshi Kagami, Hiroshi Mizoguchi, and Hirochika Inoue. High-speed pressure sensor grid for humanoid robot foot. In *2005 IEEE/RSJ International Conference on Intelligent Robots and Systems*, pages 3909–3914. IEEE, 2005.

[119] Satoshi Kagami, Koichi Nishiwaki, James Kuffner, Simon Thompson, J Chestnutt, Mike Stilman, and Philipp Michel. Humanoid hrp2-dhrc for autonomous and interactive behavior. In *Robotics Research*, pages 103–117. Springer, 2007.

[120] Baoyuan Wu, Zengfu Wang, Jianfei Luo, and Zhongcheng Wu. Perception of effective contact area distribution for humanoid robot foot. *Measurement*, 46(7):2093–2098, 2013.

[121] Vadim Chernyak, Ennio Claretti, Stephen S Nestinger, and Eduardo Torres-Jara. Caminante: A platform for sensitive walking. In *Nature-Inspired Mobile Robotics*, pages 351–358. World Scientific, 2013.

[122] Baoyuan Wu, Fei Shen, Yang Ren, Jianfei Luo, and Zhongcheng Wu. Development of an integrated perceptual foot system for humanoid robots. *International Journal of Robotics and Automation*, 27(2):217, 2012.

[123] Taiyu Okatani, Hidetoshi Takahashi, Tomoyuki Takahata, and Isao Shimoyama. Evaluation of ground slippery condition during walk of bipedal robot using mems slip sensor. In *2017 IEEE 30th International Conference on Micro Electro Mechanical Systems (MEMS)*, pages 1033–1035. IEEE, 2017.

[124] Christian Bader, Florian Bergner, and Gordon Cheng. A robust and efficient dynamic network protocol for a large-scale artificial robotic skin. In *2018 IEEE/RSJ International Conference on Intelligent Robots and Systems (IROS)*, pages 1600–1605. IEEE, 2018.

[125] E. Dean-Leon, B. Pierce, P. Mittendorfer, F. Bergner, K. Ramirez-Amaro, W. Burger, and Gordon Cheng. Tomm: Tactile omnidirectional mobile manipulator. In *2017 IEEE International Conference on Robotics and Automation (ICRA), Accepted*, May 2017.

[126] Sachin Chitta, Eitan Marder-Eppstein, Wim Meeussen, Vijay Pradeep, Adolfo Rodríguez Tsouroukdissian, Jonathan Bohren, David Coleman, Bence Magyar, Gennaro Raiola, Mathias Lüdtke, et al. ros_control: A generic and simple control framework for ros. *The Journal of Open Source Software*, 2(20):456–456, 2017.

[127] Stéphane Caron, Abderrahmane Kheddar, and Olivier Tempier. Stair climbing stabilization of the hrp-4 humanoid robot using whole-body admittance control. In *2019 International Conference on Robotics and Automation (ICRA)*, pages 277–283. IEEE, 2019.

[128] Oussama Khatib. A unified approach for motion and force control of robot manipulators: The operational space formulation. *IEEE Journal on Robotics and Automation*, 3(1):43–53, 1987.

[129] Luis Sentis, Jaeheung Park, and Oussama Khatib. Compliant control of multicontact and center-of-mass behaviors in humanoid robots. *IEEE Transactions on robotics*, 26(3):483–501, 2010.

[130] B Siciliano and J-JE Slotine. A general framework for managing multiple tasks in highly redundant robotic systems. In *Fifth International Conference on Advanced Robotics' Robots in Unstructured Environments*, pages 1211–1216. IEEE, 1991.

[131] Luis Sentis and Oussama Khatib. Synthesis of whole-body behaviors through hierarchical control of behavioral primitives. *International Journal of Humanoid Robotics*, 2(04):505–518, 2005.

[132] Tomoyuki Noda, Takahiro Miyashita, Hiroshi Ishiguro, and Norihiro Hagita. Super-flexible skin sensors embedded on the whole body, self-organizing based on haptic interactions. *Human-Robot Interaction in Social Robotics*, page 183, 2012.

[133] Quentin Leboutet, Emmanuel Dean-Leon, Florian Bergner, and Gordon Cheng. Tactile-based whole-body compliance with force propagation for mobile manipulators. *IEEE Transactions on Robotics*, 35(2):330–342, 2019.

[134] Giorgio Cannata, Marco Maggiali, Giorgio Metta, and Giulio Sandini. An embedded artificial skin for humanoid robots. In *Multisensor Fusion and Integration for Intelligent Systems, 2008. MFI 2008. IEEE International Conference on*, pages 434–438. IEEE, 2008.

[135] Takao Someya, Yusaku Kato, Tsuyoshi Sekitani, Shingo Iba, Yoshiaki Noguchi, Yousuke Murase, Hiroshi Kawaguchi, and Takayasu Sakurai. Conformable, flexible, large-area networks of pressure and thermal sensors with organic transistor active matrixes. *Proceedings of the National Academy of Sciences*, 102(35):12321–12325, 2005.

[136] Tomomichi Sugihara and Yoshihiko Nakamura. Whole-body cooperative balancing of humanoid robot using cog jacobian. In *IEEE/RSJ international conference on intelligent robots and systems*, volume 3, pages 2575–2580. IEEE, 2002.

[137] Alexander Dietrich, Thomas Wimbock, Alin Albu-Schaffer, and Gerd Hirzinger. Integration of reactive, torque-based self-collision avoidance into a task hierarchy. *IEEE Transactions on Robotics*, 28(6):1278–1293, 2012.

[138] Oussama Khatib. The potential field approach and operational space formulation in robot control. In *Adaptive and Learning Systems*, pages 367–377. Springer, 1986.

[139] CL Boddy and JD Taylor. Whole-arm reactive collision avoidance control of kinematically redundant manipulators. In *Robotics and Automation, 1993. Proceedings., 1993 IEEE International Conference on*, pages 382–387. IEEE, 1993.

[140] Edward R Perl. Ideas about pain, a historical view. *Nature Reviews Neuroscience*, 8(1):71–80, 2007.

[141] AD Craig. Pain mechanisms: labeled lines versus convergence in central processing. *Annual review of neuroscience*, 26(1):1–30, 2003.

[142] Romildo Don, Francesco Pierelli, Alberto Ranavolo, Mariano Serrao, Massimiliano Mangone, Marco Paoloni, Angelo Cacchio, Giorgio Sandrini, and Valter Santilli. Modulation of spinal inhibitory reflex responses to cutaneous nociceptive stimuli during upper limb movement. *European Journal of Neuroscience*, 28(3):559–568, 2008.

[143] JS Yuan. Closed-loop manipulator control using quaternion feedback. *IEEE Journal on Robotics and Automation*, 4(4):434–440, 1988.

[144] Prahlad Vadakkepat, Kay Chen Tan, and Wang Ming-Liang. Evolutionary artificial potential fields and their application in real time robot path planning. In *Evolutionary Computation, 2000. Proceedings of the 2000 Congress on*, volume 1, pages 256–263. IEEE, 2000.

[145] Yoram Koren, Johann Borenstein, et al. Potential field methods and their inherent limitations for mobile robot navigation. In *ICRA*, volume 2, pages 1398–1404, 1991.

[146] Min Gyu Park and Min Cheol Lee. A new technique to escape local minimum in artificial potential field based path planning. *KSME international journal*, 17(12):1876–1885, 2003.

[147] Marko B Popovic, Ambarish Goswami, and Hugh Herr. Ground reference points in legged locomotion: Definitions, biological trajectories and control implications. *The International Journal of Robotics Research*, 24(12):1013–1032, 2005.

[148] Shuuji Kajita, Fumio Kanehiro, Kenji Kaneko, Kiyoshi Fujiwara, Kensuke Harada, Kazuhito Yokoi, and Hirohisa Hirukawa. Biped walking pattern generation by using preview control of zero-moment point. In *2003 IEEE International Conference on Robotics and Automation (Cat. No. 03CH37422)*, volume 2, pages 1620–1626. IEEE, 2003.

[149] PAL Robotics. REEM-C, 2015.

[150] Jaynie F Yang and Richard B Stein. Phase-dependent reflex reversal in human leg muscles during walking. *Journal of Neurophysiology*, 63(5):1109–1117, 1990.

[151] David A Winter. Human balance and posture control during standing and walking. *Gait & posture*, 3(4):193–214, 1995.

[152] J. Duysens, M. Trippel, G. A. Horstmann, and V. Dietz. Gating and reversal of reflexes in ankle muscles during human walking. *Experimental Brain Research*, 82(2):351–358, Oct 1990.

[153] David A Winter. *Biomechanics and motor control of human gait: normal, elderly and pathological*. 1991.

[154] Jessy W Grizzle, Christine Chevallereau, Ryan W Sinnet, and Aaron D Ames. Models, feedback control, and open problems of 3d bipedal robotic walking. *Automatica*, 50(8):1955–1988, 2014.

[155] Miomir Vukobratović and J Stepanenko. On the stability of anthropomorphic systems. *Mathematical biosciences*, 15(1-2):1–37, 1972.

[156] Jerry Pratt, John Carff, Sergey Drakunov, and Ambarish Goswami. Capture point: A step toward humanoid push recovery. In *2006 6th IEEE-RAS international conference on humanoid robots*, pages 200–207. IEEE, 2006.

[157] AL Hof, MGJ Gazendam, and WE Sinke. The condition for dynamic stability. *Journal of biomechanics*, 38(1):1–8, 2005.

[158] Joel Chestnutt, Manfred Lau, German Cheung, James Kuffner, Jessica Hodgins, and Takeo Kanade. Footstep planning for the honda asimo humanoid. In *Proceedings of the 2005 IEEE international conference on robotics and automation*, pages 629–634. IEEE, 2005.

[159] James J Kuffner, Koichi Nishiwaki, Satoshi Kagami, Masayuki Inaba, and Hirochika Inoue. Footstep planning among obstacles for biped robots. In *Proceedings 2001 IEEE/RSJ International Conference on Intelligent Robots and Systems. Expanding the Societal Role of Robotics in the the Next Millennium (Cat. No. 01CH37180)*, volume 1, pages 500–505. IEEE, 2001.

[160] Bjorn Verrelst, Olivier Stasse, Kazuhito Yokoi, and Bram Vanderborght. Dynamically stepping over obstacles by the humanoid robot hrp-2. In *2006 6th IEEE-RAS International Conference on Humanoid Robots*, pages 117–123. IEEE, 2006.

[161] Minh Nhat Vu, Jongwoo Lee, and Yonghwan Oh. A finite state machine and walking control algorithm of the biped robot with flat foot. In *2017 IEEE International Conference on Mechatronics and Automation (ICMA)*, pages 1180–1186. IEEE, 2017.

[162] J Rogelio Guadarrama-Olvera, Florian Bergner, Emmanuel Dean, and Gordon Cheng. Enhancing biped locomotion on unknown terrain using tactile feedback. In *2018 IEEE-RAS 18th International Conference on Humanoid Robots (Humanoids)*, pages 1–9. IEEE, 2018.

[163] Perla Maiolino, Marco Maggiali, Giorgio Cannata, Giorgio Metta, and Lorenzo Natale.

A flexible and robust large scale capacitive tactile system for robots. *IEEE Sensors Journal*, 13(10):3910–3917, 2013.

[164] Kent N Bachus, Alyssa L DeMarco, Kyle T Judd, Daniel S Horwitz, and Darrel S Brodke. Measuring contact area, force, and pressure for bioengineering applications: using fuji film and tekscan systems. *Medical engineering & physics*, 28(5):483–488, 2006.

[165] Qingdan Yuan and Jianxiao Wang. Design and experiment of the nao humanoid robot's plantar tactile sensor for surface classification. In *2017 4th International Conference on Information Science and Control Engineering (ICISCE)*, pages 931–935. IEEE, 2017.

[166] Philipp Mittendorfer and Gordon Cheng. Uniform cellular design of artificial robotic skin. In *ROBOTIK 2012; 7th German Conference on Robotics*, pages 1–5. VDE, 2012.

[167] Florian Bergner, Emmanuel Dean-Leon, and Gordon Cheng. Event-based signaling for large-scale artificial robotic skin - realization and performance evaluation. In *IEEE/RSJ International Conference on Intelligent Robots and Systems (IROS)*, pages 4918–4924, 2016.

[168] Philipp Mittendorfer and Gordon Cheng. 3d surface reconstruction for robotic body parts with artificial skins. In *Intelligent Robots and Systems (IROS), 2012 IEEE/RSJ International Conference on*, pages 4505–4510. IEEE, 2012.

[169] Luís Almeida, Vítor Santos, and Filipe Silva. A novel wireless instrumented shoe for ground reaction forces analysis in humanoids. In *2018 IEEE International Conference on Autonomous Robot Systems and Competitions (ICARSC)*, pages 36–41. IEEE, 2018.

[170] Hideaki Minakata, Hirokazu Seki, and Susumu Tadakuma. A study of energy-saving shoes for robot considering lateral plane motion. *IEEE Transactions on Industrial Electronics*, 55(3):1271–1276, 2008.

[171] Franco P. Preparata and Se June Hong. Convex hulls of finite sets of points in two and three dimensions. *Communications of the ACM*, 20(2):87–93, 1977.

[172] Jin-Seo Park and Se-Jong Oh. A new concave hull algorithm and concaveness measure for n-dimensional datasets. *Journal of Information science and engineering*, 28(3):587–600, 2012.

[173] Ivor van der Hoog, Vahideh Keikha, Maarten Löffler, Ali Mohades, and Jérôme Urhausen. Maximum-area triangle in a convex polygon, revisited. *Information Processing Letters*, page 105943, 2020.

[174] Kai Jin and Kevin Matulef. Finding the maximum area parallelogram in a convex polygon. In *CCCG*, 2011.

[175] Christian Schwarz, Jürgen Teich, Emo Welzl, and Brian Evans. On finding a minimal enclosing parallelogram. *International Computer Science Institute, Berkeley, CA, Tech. Rep. tr-94-036*, 1994.

[176] Bram Vanderborght, Alin Albu-Schäffer, Antonio Bicchi, Etienne Burdet, Darwin G Caldwell, Raffaella Carloni, MG Catalano, Oliver Eiberger, Werner Friedl, Ganesh Ganesh, et al. Variable impedance actuators: A review. *Robotics and autonomous systems*, 61(12):1601–1614, 2013.

[177] Diego Torricelli, Jose Gonzalez, Maarten Weckx, René Jiménez-Fabián, Bram Vanderborght, Massimo Sartori, Strahinja Dosen, Dario Farina, Dirk Lefeber, and Jose L Pons. Human-like compliant locomotion: state of the art of robotic implementations. *Bioinspiration & biomimetics*, 11(5):051002, 2016.

[178] Hikaru Arita and Aiguo Ming. Real-time motion planning using proximity information for bipedal walking on sloped terrain. *Journal of the Robotics Society of Japan*, 38(4):401–408, 2020.

[179] Manuel Krause, Johannes Englsberger, Pierre-Brice Wieber, and Christian Ott. Stabilization of the capture point dynamics for bipedal walking based on model predictive control. *IFAC Proceedings Volumes*, 45(22):165–171, 2012.

[180] Jiang Yi, Qiuguo Zhu, Rong Xiong, and Jun Wu. Walking algorithm of humanoid robot on uneven terrain with terrain estimation. *International Journal of Advanced Robotic Systems*, 13(1):35, 2016.

[181] Hyun-Min Joe and Jun-Ho Oh. A robust balance-control framework for the terrain-blind bipedal walking of a humanoid robot on unknown and uneven terrain. *Sensors*, 19(19):4194, 2019.

[182] Chen Koon Toh, Ming Xie, Hejin Yang, Guoqing Zhang, Quoc Phuong Bui, and Bo Tian. Flexible foot design for biped walking on uneven terrain. In *International Conference on Intelligent Robotics and Applications*, pages 442–452. Springer, 2010.

[183] Patrick M Wensing, Ghassan Bin Hammam, Behzad Dariush, and David E Orin. Optimizing foot centers of pressure through force distribution in a humanoid robot. *International Journal of Humanoid Robotics*, 10(03):1350027, 2013.

[184] Johannes Englsberger, Christian Ott, and Alin Albu-Schäffer. Three-dimensional

bipedal walking control based on divergent component of motion. *IEEE Transactions on Robotics*, 31(2):355–368, 2015.

[185] Behzad Khorshidi. A new method for finding the center of gravity of polygons. *Journal of Geometry*, 96(1-2):81–91, 2009.

[186] Mitsuharu Morisawa, Shuuji Kajita, Kensuke Harada, Kiyoshi Fujiwara, Fumio Kanehiro, Kenji Kaneko, and Hirohisa Hirukawa. Emergency stop algorithm for walking humanoid robots. In *2005 IEEE/RSJ International Conference on Intelligent Robots and Systems*, pages 2109–2115. IEEE, 2005.

[187] Johannes Englsberger and Christian Ott. Integration of vertical com motion and angular momentum in an extended capture point tracking controller for bipedal walking. In *2012 12th IEEE-RAS International Conference on Humanoid Robots (Humanoids 2012)*, pages 183–189. IEEE, 2012.

[188] Shuuji Kajita, Mitsuharu Morisawa, Kanako Miura, Shin'ichiro Nakaoka, Kensuke Harada, Kenji Kaneko, Fumio Kanehiro, and Kazuhito Yokoi. Biped walking stabilization based on linear inverted pendulum tracking. In *2010 IEEE/RSJ International Conference on Intelligent Robots and Systems*, pages 4489–4496. IEEE, 2010.

[189] Karen Daniels, Victor Milenkovic, and Dan Roth. Finding the largest area axis-parallel rectangle in a polygon. *Computational Geometry*, 7(1-2):125–148, 1997.

[190] Hervé Audren and Abderrahmane Kheddar. 3-d robust stability polyhedron in multicontact. *IEEE Transactions on Robotics*, 34(2):388–403, 2018.

[191] Stéphane Caron, Quang-Cuong Pham, and Yoshihiko Nakamura. Zmp support areas for multicontact mobility under frictional constraints. *IEEE Transactions on Robotics*, 33(1):67–80, 2016.